

007 111 0077

①

CECOM Center for Night Vision and Electro-Optics

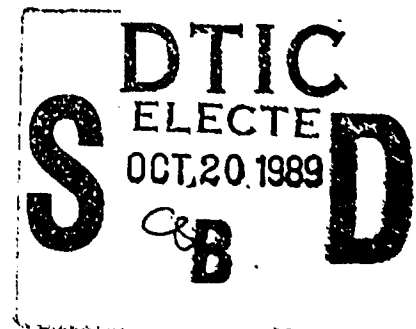
AD-A213 482

OPTOELECTRONIC WORKSHOPS

IX

DYNAMICAL INSTABILITIES IN HOMOGENEOUSLY BROADENED LASERS

August 23, 1988



sponsored jointly by

ARO-URI Center for Opto-Electronic Systems Research
The Institute of Optics, University of Rochester

①

REPORT DOCUMENTATION PAGE				
1a. REPORT SECURITY CLASSIFICATION Unclassified		1b. RESTRICTIVE MARKINGS		
2a. SECURITY CLASSIFICATION AUTHORITY OCT 20 1989		2b. DECLASSIFICATION/DOWNGRADING SCHEDULE Approved for public release; distribution unlimited.		
4. PERFORMING ORGANIZATION REPORT NUMBER(S)		5. MONITORING ORGANIZATION REPORT NUMBER(S)		
6a. NAME OF PERFORMING ORGANIZATION University of Rochester	6b. OFFICE SYMBOL (If applicable)	7a. NAME OF MONITORING ORGANIZATION U. S. Army Research Office		
6c. ADDRESS (City, State, and ZIP Code) The Insitute of Optics Rochester, NY 14627		7b. ADDRESS (City, State, and ZIP Code) P. O. Box 12211 Research Triangle Park, NC 27709-2211		
8a. NAME OF FUNDING/SPONSORING ORGANIZATION U. S. Army Research Office	8b. OFFICE SYMBOL (If applicable)	9. PROCUREMENT INSTRUMENT IDENTIFICATION NUMBER DAAL03-86-K-0173		
8c. ADDRESS (City, State, and ZIP Code) P. O. Box 12211 Research Triangle Park, NC 27709-2211		10. SOURCE OF FUNDING NUMBERS		
		PROGRAM ELEMENT NO.	PROJECT NO.	TASK NO.
		WORK UNIT ACCESSION NO.		
11. TITLE (Include Security Classification) Optoelectronic Workshop IX: Dynamical Instabilities in Homogeneously Broadened Lasers				
12. PERSONAL AUTHOR(S) Carlos R. Stroud, Jr.				
13a. TYPE OF REPORT Technical	13b. TIME COVERED FROM TO	14. DATE OF REPORT (Year, Month, Day) August 23, 1988	15. PAGE COUNT	
16. SUPPLEMENTARY NOTATION The view, opinions and/or findings contained in this report are those of the author(s) and should not be construed as an official Department of the Army position, policy, or decision, unless so designated by other documentation.				
17. COSATI CODES		18. SUBJECT TERMS (Continue on reverse if necessary and identify by block number)		
FIELD	GROUP	SUB-GROUP		
		Workshop; dynamical instabilities in homogeneously broadened lasers		
19. ABSTRACT (Continue on reverse if necessary and identify by block number)				
This workshop on "Dynamical Instabilities in Homogeneously Broadened Lasers" represents the ninth of a series of intensive academic/ government interactions in the field of advanced electro-optics, as part of the Army sponsored University Research Initiative. By documenting the associated technology status and dialogue it is hoped that this baseline will serve all interested parties towards providing a solution to high priority Army requirements. Responsible for program and program execution are Dr. Nicholas George, University of Rochester (ARO-URI) and Dr. Rudy Buser, NVEOC.				
20. DISTRIBUTION/AVAILABILITY OF ABSTRACT <input type="checkbox"/> UNCLASSIFIED/UNLIMITED <input type="checkbox"/> SAME AS RPT. <input type="checkbox"/> DTIC USERS		21. ABSTRACT SECURITY CLASSIFICATION Unclassified		
22a. NAME OF RESPONSIBLE INDIVIDUAL Nicholas George		22b. TELEPHONE (Include Area Code) 716-275-2417	22c. OFFICE SYMBOL	

CECOM Center for Night Vision and Electro-Optics

OPTOELECTRONIC WORKSHOPS

IX

**DYNAMICAL INSTABILITIES IN
HOMOGENEOUSLY BROADENED LASERS**

August 23, 1988

sponsored jointly by

**ARO-URI Center for Opto-Electronic Systems Research
The Institute of Optics, University of Rochester**

OPTOELECTRONIC WORKSHOP
ON
DYNAMICAL INSTABILITIES IN HOMOGENEOUSLY BROADENED LASERS

**Organizer: ARO-URI-University of Rochester
and CECOM Center for Night Vision and Electro-Optics**

- 1. INTRODUCTION**
- 2. SUMMARY -- INCLUDING FOLLOW-UP**
- 3. VIEWGRAPH PRESENTATIONS**

- A. Center for Opto-Electronic Systems Research
Organizer -- Carlos R. Stroud**

**Introduction and Overview
Carlos R. Stroud**

**Broadband Homogeneously Broadened Lasers: Dye Lasers
Karl Koch**

**Modulation Techniques: Alexandrite Lasers
Stephen Chakmakjian**

**Summary
Carlos R. Stroud**

- B. CECOM Center for Night Vision and Electro-Optics
Organizer -- Albert Pinto**

**Needs for Broadband Materials and Systems
Albert Pinto**

V⁴⁺ in Corundum: Crystal Growth and Spectroscopy

**Characterization of the Optical Spectra of EuA10₃:Ti
and GdA10₃:Ti**

- 4. LIST OF ATTENDEES**

Accession For	
NTIS SPA&I	<input checked="checked" type="checkbox"/>
DTIC TAB	<input type="checkbox"/>
Unannounced	<input type="checkbox"/>
Justification	
By	
Distribution/	
Availability Codes	
Dist	Avail and/or Special
A-1	

1. INTRODUCTION

This workshop on "Dynamical Instabilities in Homogeneously Broadened Lasers" represents the ninth of a series of intensive academic/ government interactions in the field of advanced electro-optics, as part of the Army sponsored University Research Initiative. By documenting the associated technology status and dialogue it is hoped that this baseline will serve all interested parties towards providing a solution to high priority Army requirements. Responsible for program and program execution are Dr. Nicholas George, University of Rochester (ARO-URI) and Dr. Rudy Buser, NVEOC.

2. SUMMARY AND FOLLOW-UP ACTIONS

Dr. Pinto opened the meeting giving an overview of current projects and problems of interest in the Laser Division. He discussed their work to find efficient diode laser pumped solid state lasers in the 1 micro band. He went into some detail concerning their interest in activating laser crystals for broadband absorption of laser diode array emission, such as those discussed in the article by A. A. Kaminskii. (Phys. Stat. Sol. **87**, 11 (1985).

Dr. Stroud then gave a general introduction to the work going on in this group at the University of Rochester involving laser dynamics in homogeneously broadened laser systems. He briefly surveyed the recent progress in understanding spiking and chaotic instabilities in homogeneously broadened lasers.

Karl Koch then gave a presentation in the instabilities that he has been studying in dye lasers, both intrinsic instabilities and the instabilities that are induced by external modulation. He pointed out that in dye lasers and other tunable lasers of the phonon assisted variety are not well described by simple ideal 4 level models. He described the work going on in Rochester and in Professor Haken's group in Stutgard on improved models for these systems.

Stephen Chakmakjian then discussed his work on alexandrite, another phonon assisted homogeneously broadened laser. He described in some detail modulation spectroscopic techniques developed in Rochester that allow one to easily measure the various lifetimes involved in the internal population dynamics in these lasers.

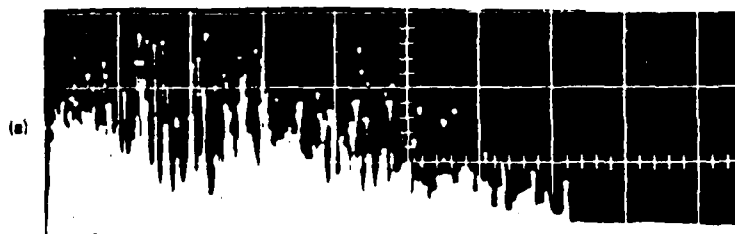
Dr. Stroud then summarized the work and described some of the projects that were planned or underway in this area in Rochester. This was followed by a general discussion on the ways that the modulation techniques might be usefully implemented to help characterize the activated crystals. Dr. Stroud said that he was not really set up in his laboratory at present to systematically go through a long list of materials and characterize them, but that he could easily look at one or two. Another possibility is that one or two of the students from Rochester might spend a few days at NVEOC to help in setting up an experiment there to make such measurements.

Another problem in the Laser Division was developing a simple way of determining whether a potential laser material is homogeneously or inhomogeneously broadened. Dr. Stroud discussed some of the usual techniques, and promised to send Dr. Pinto a writeup summarizing the problem.

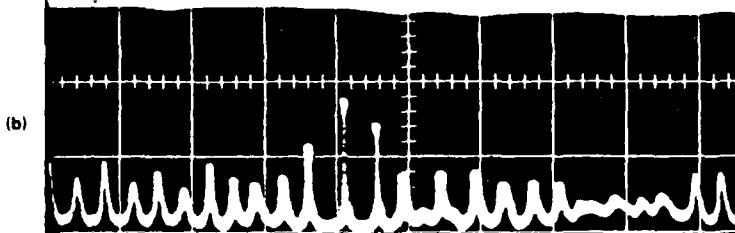
CENTER FOR OPTO-ELECTRONIC SYSTEMS RESEARCH
INTRODUCTION AND OVERVIEW

LASERS ARE NOISIER THAN THEY SHOULD BE

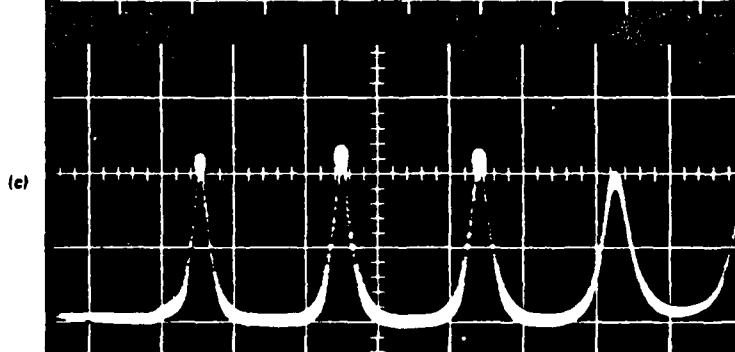
200 $\mu\text{s}/\text{cm}$



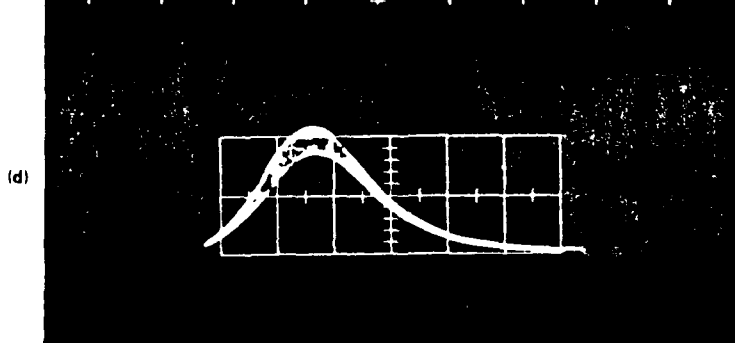
5 $\mu\text{s}/\text{cm}$



1 $\mu\text{s}/\text{cm}$



100 ns/cm



Spiking in Ruby Laser output

ARE LASERS NATURALLY UNSTABLE?

- Described by **NONLINEAR** equations.
- General solutions do not exist.
- Behavior may be qualitatively different for varying parameters and initial conditions.
- Progress has been made in study of driven nonlinear systems.
- System may be stable in some regions of parameters by display

BISTABILITY

HYSTERESIS

CHAOS

for other values of parameters.

Homogeneously Broadened Lasers

Textbook:

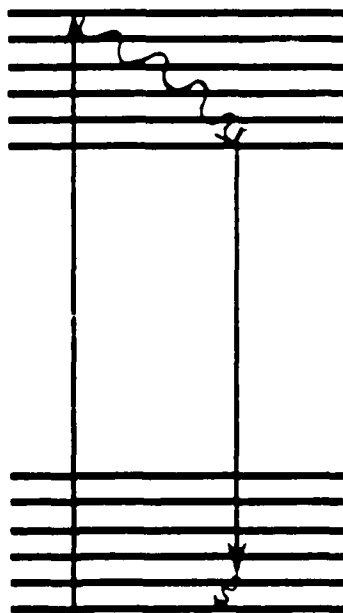
"An ideal homogeneously broadened laser will operate in one mode."

Engineer:

"Nonsense!"

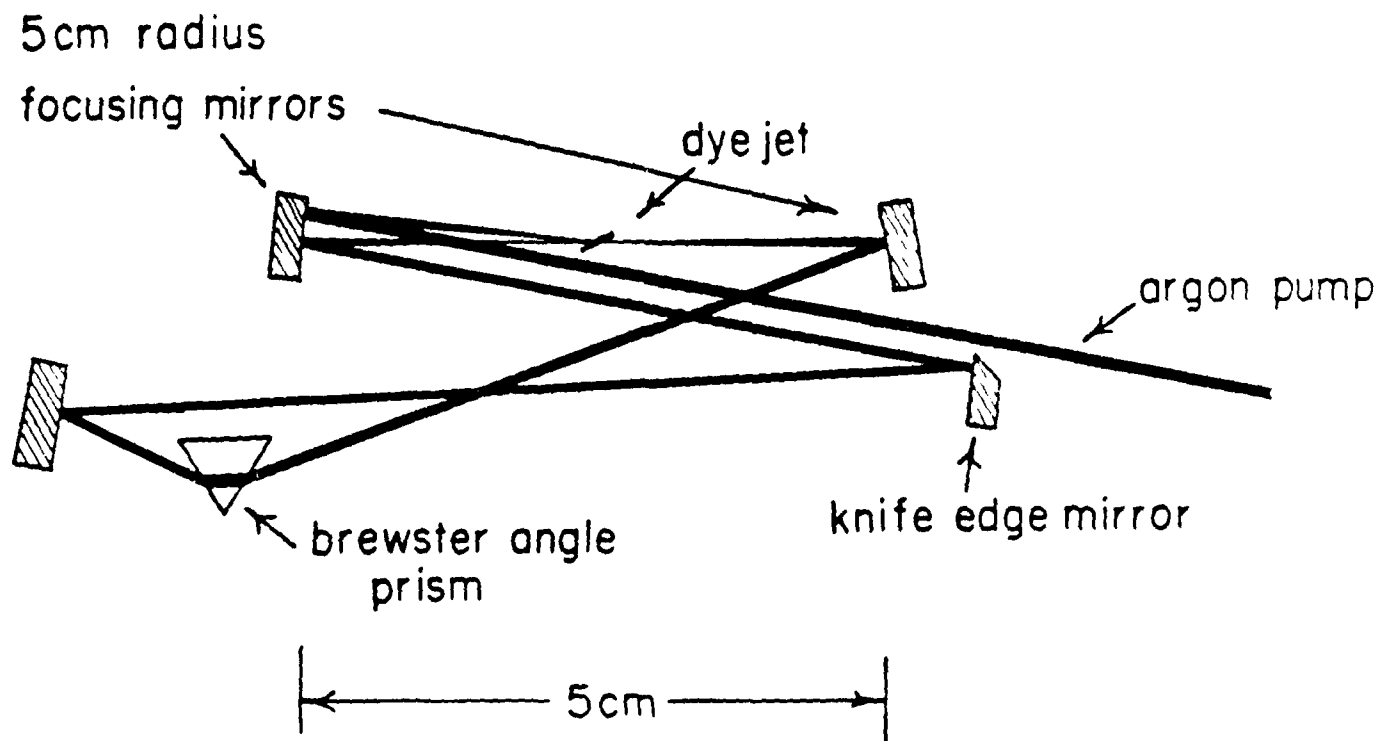
Question:

Are broadband tunable lasers ideal homogeneously broadened systems?



CENTER FOR OPTO-ELECTRONIC SYSTEMS RESEARCH
BROADBAND HOMOGENEOUSLY BROADENED LASERS: DYE LASERS

HIGH-Q RING DYE LASER



Low loss

1 Watt pump produces 50 Watts circulating dye laser power

10 μm focal spot generates 50 MWatts / cm^2 in the gain region

Pinhole ensures single transverse mode

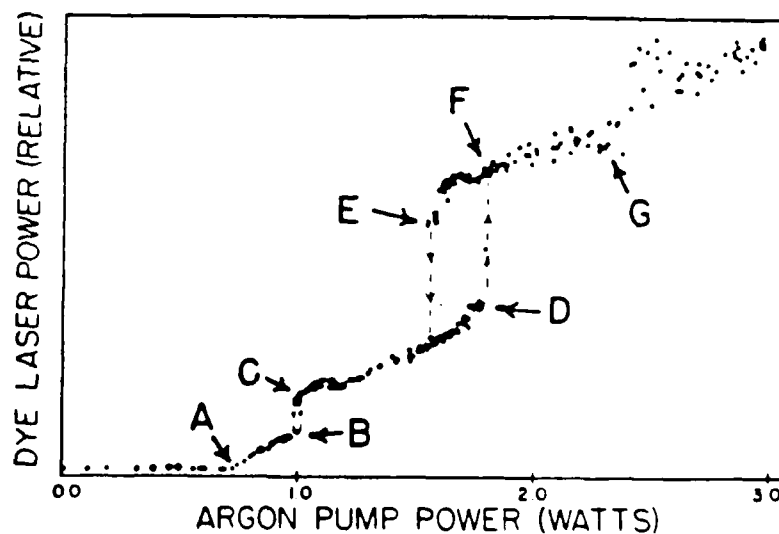
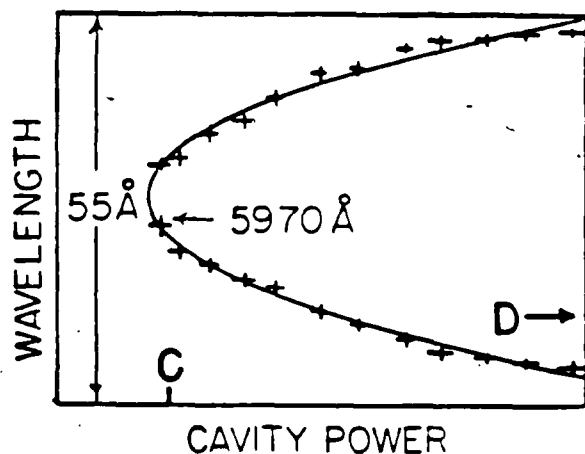
TWO-FREQUENCY INSTABILITY

CHARACTERISTICS

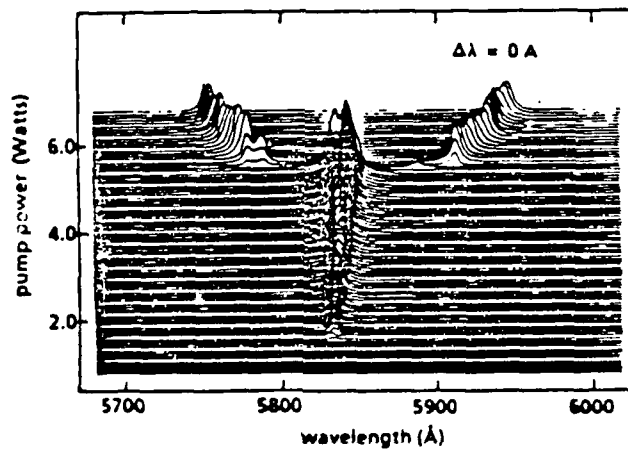
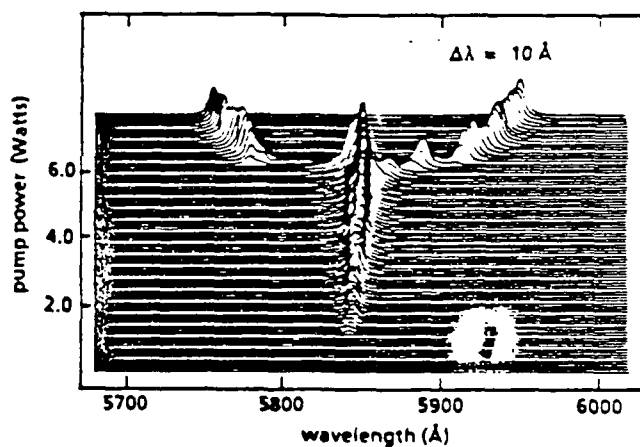
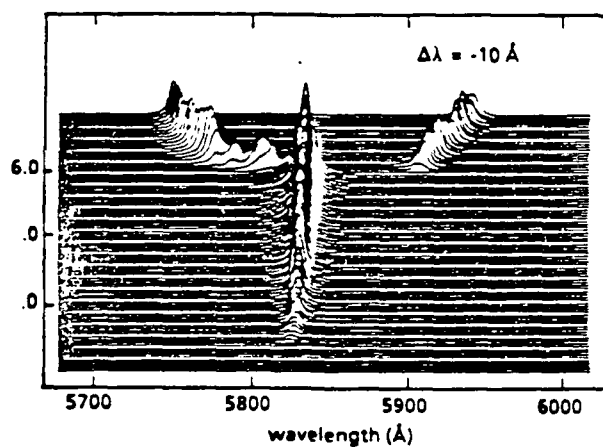
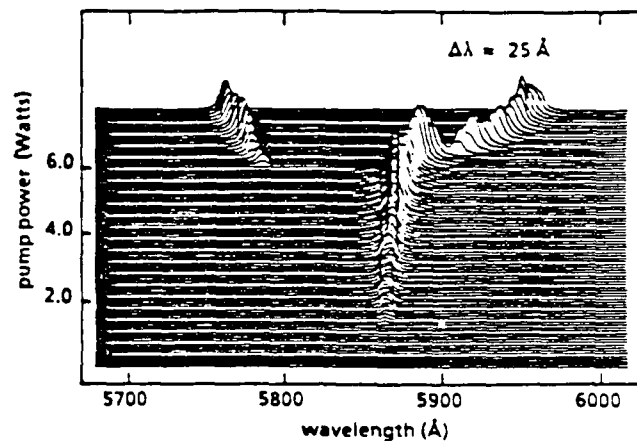
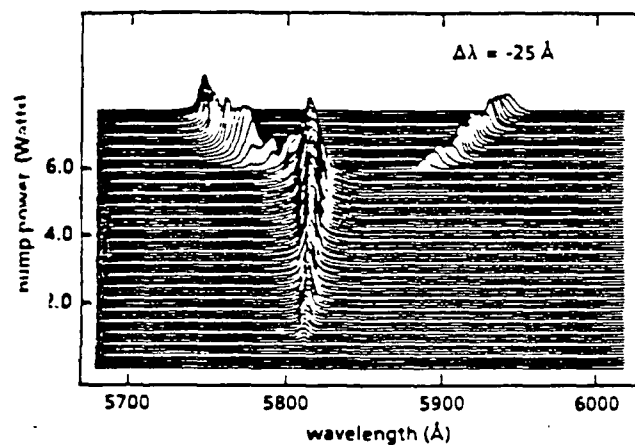
Low threshold $\ll 9$ times above threshold

Two-frequency operation whose splitting increases as the square root of the intensity.

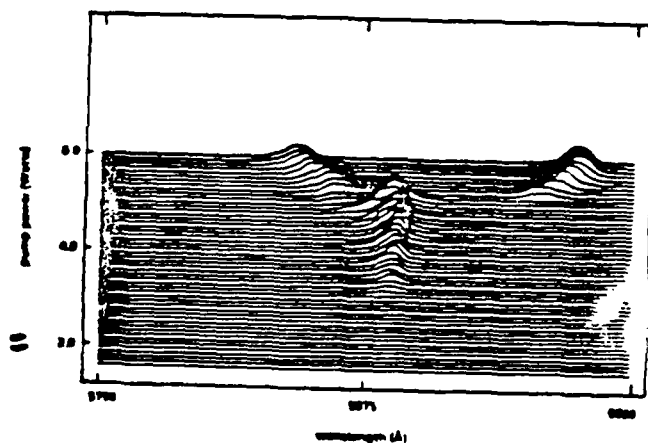
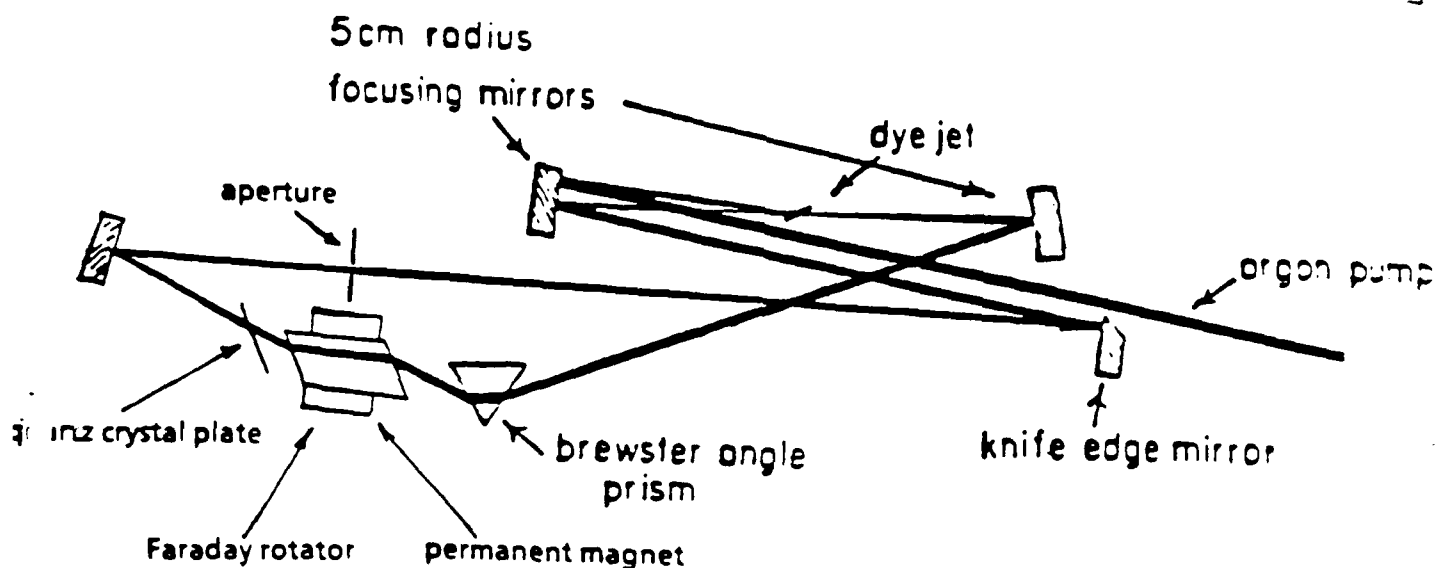
Discontinuous jumps in output intensity and associated hysteresis loops as a function of pump power.



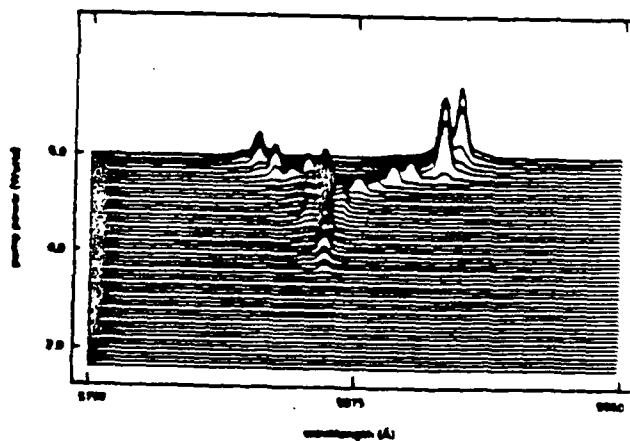
EFFECTS OF DETUNING



UNIDIRECTIONAL OPERATION



Bidirectional

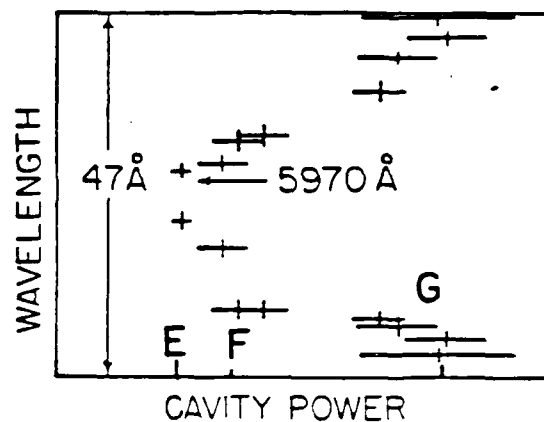
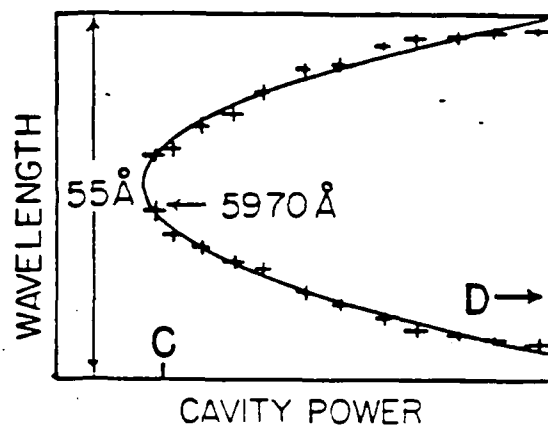


Unidirectional

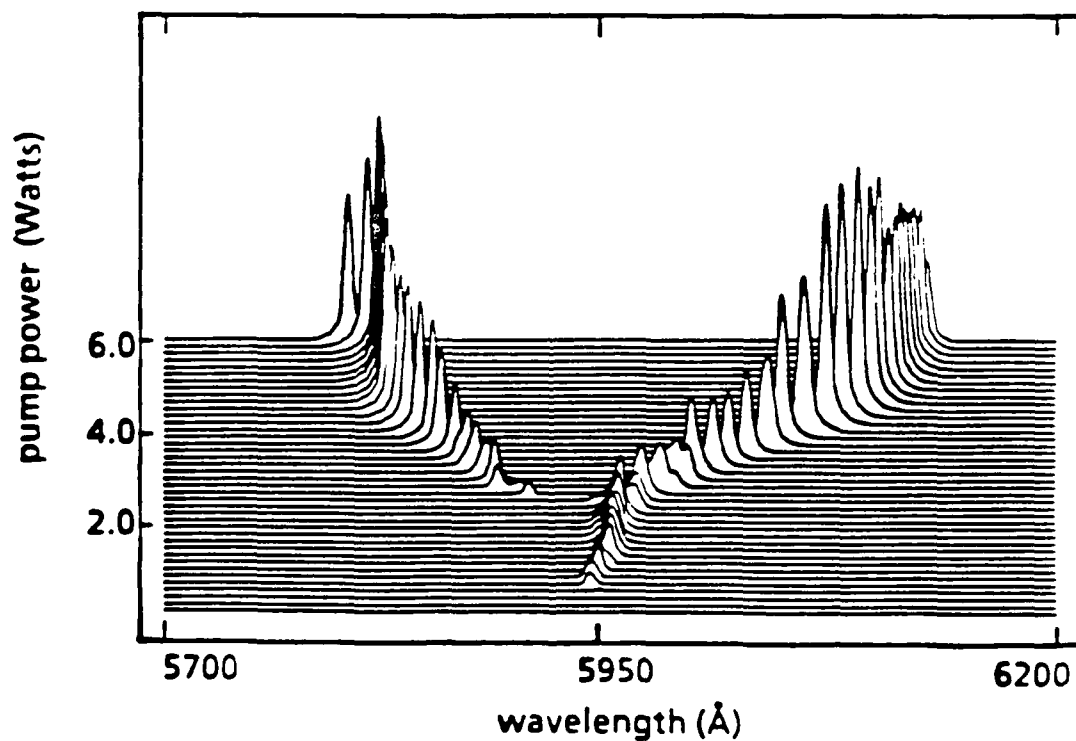
The two frequency instability is still present in the unidirectional laser.

The quartz crystal plate acts as an etalon and imposes a coarse mode structure on the spectrum.

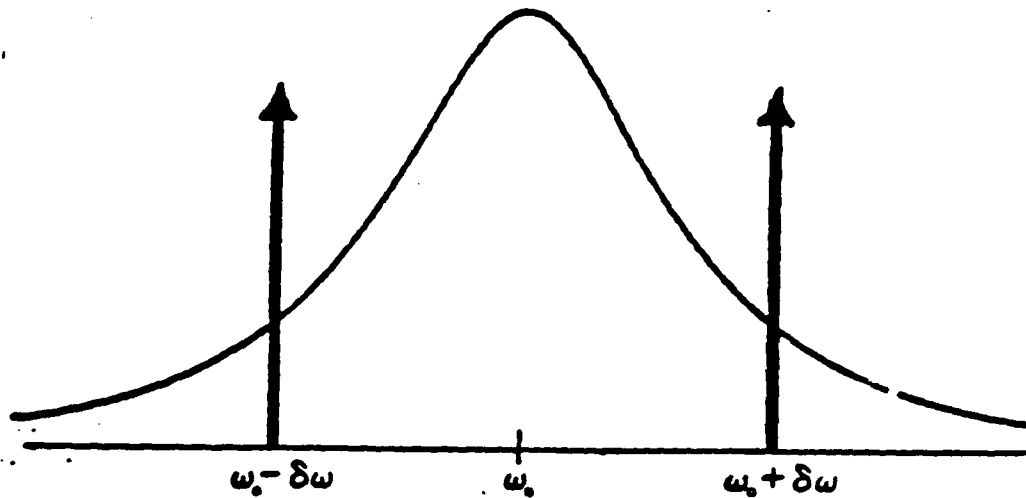
EFFECTS OF FREQUENCY DEPENDENT LOSS



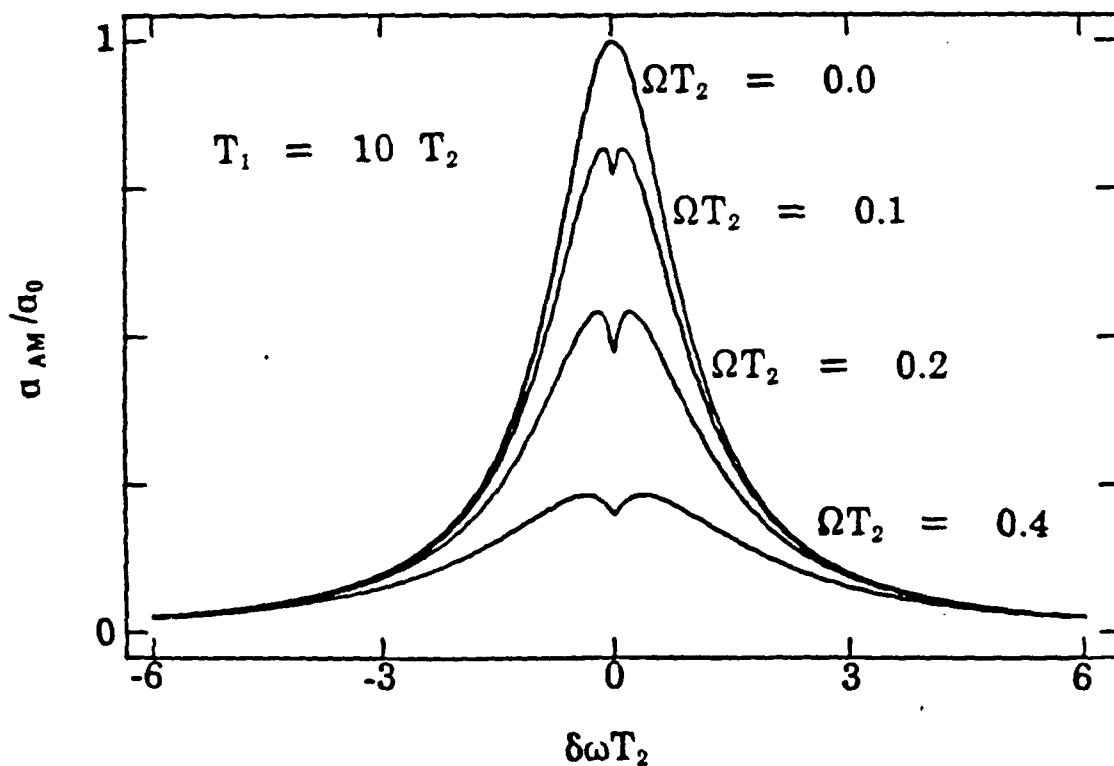
340Å SPLITTING



TWO-FREQUENCY ANALYSIS

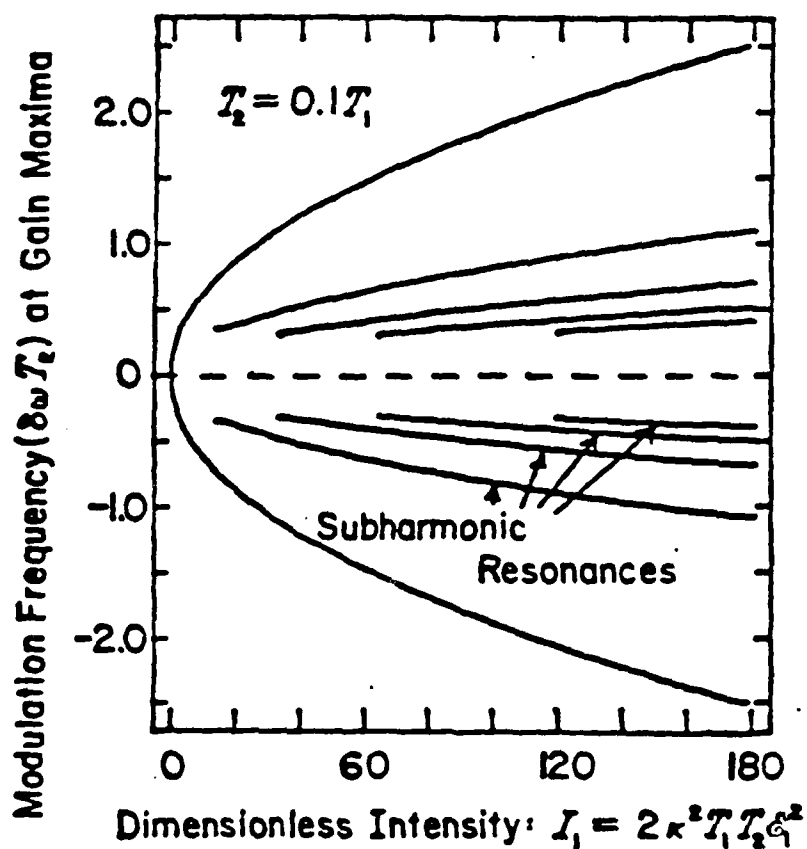
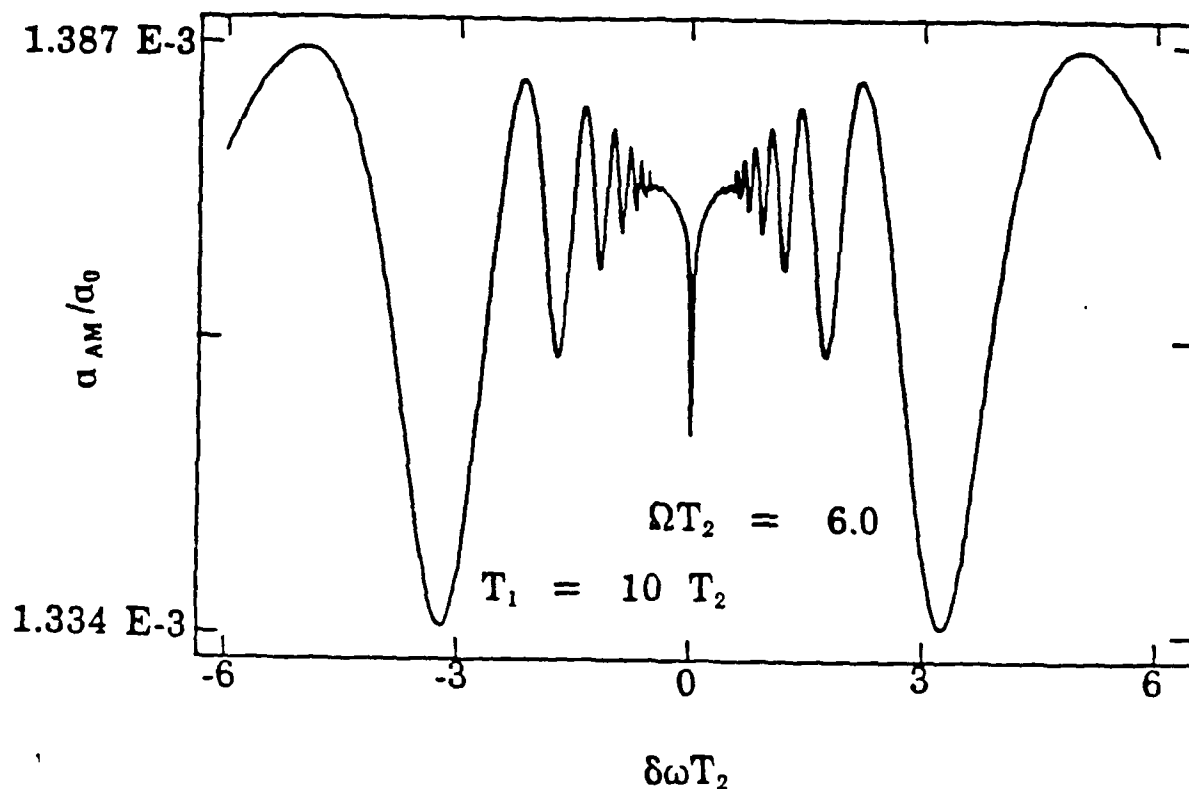


We analyze the atomic response to a field made up of two frequencies of equal amplitude. The two components are separated by $2\delta\omega$. $\delta\omega$ is referred to as the modulation frequency.

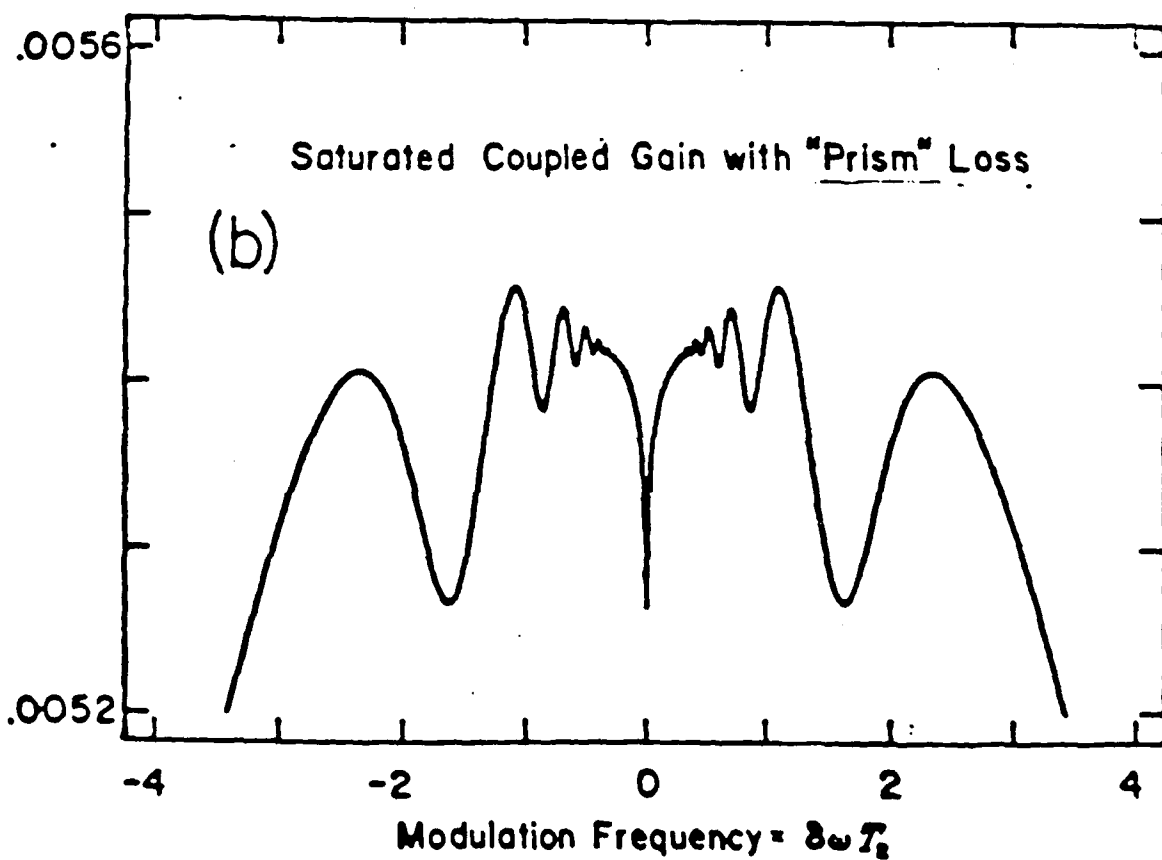
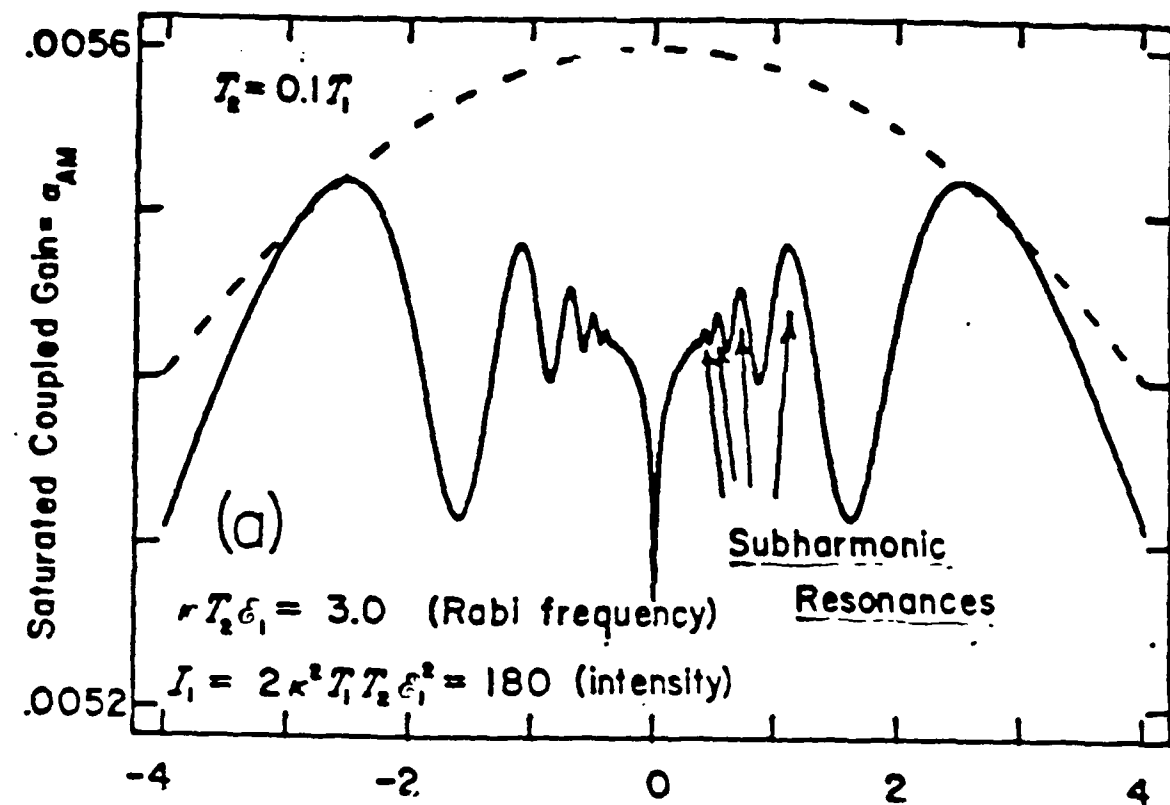


The saturated gain experienced by the two-frequency field exhibits a dip near zero modulation frequency.

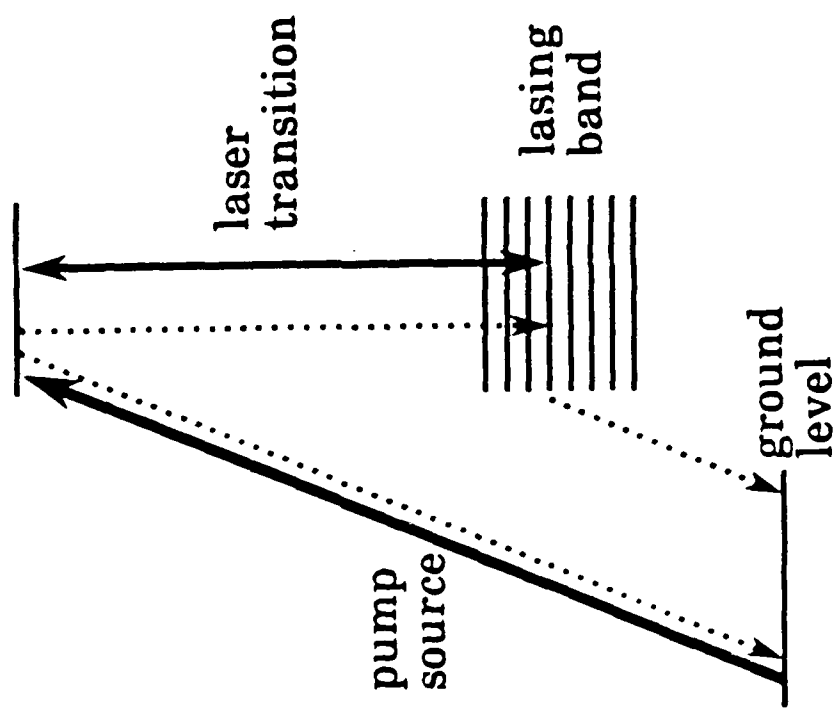
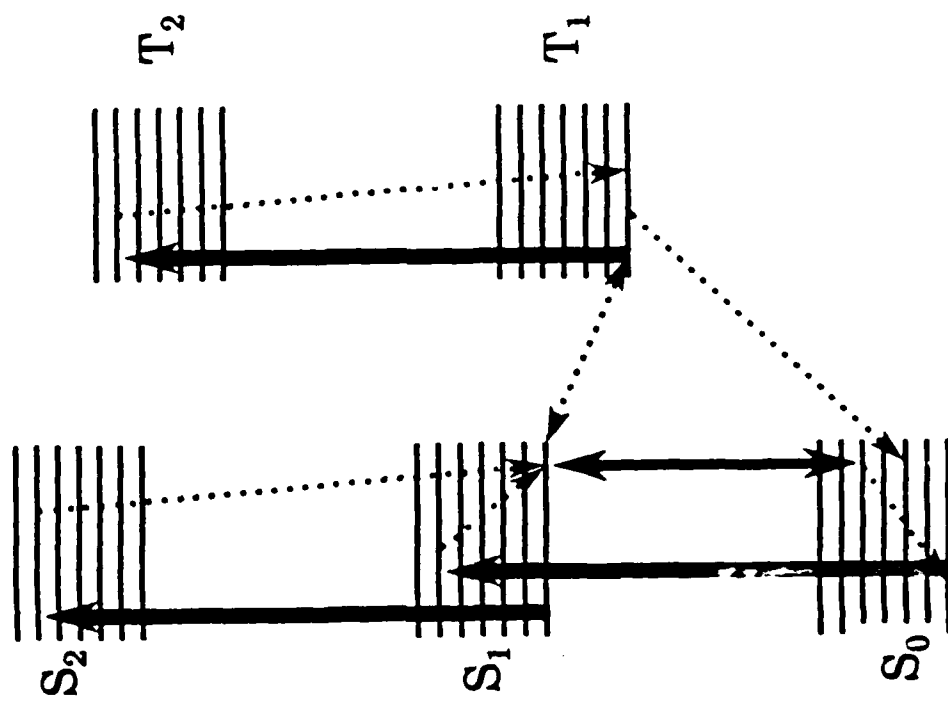
Maximum gain occurs for a nonzero modulation frequency.



For large field amplitudes the dip in the saturated gain develops structure. This structure shows subharmonic resonances of the Rabi frequency.



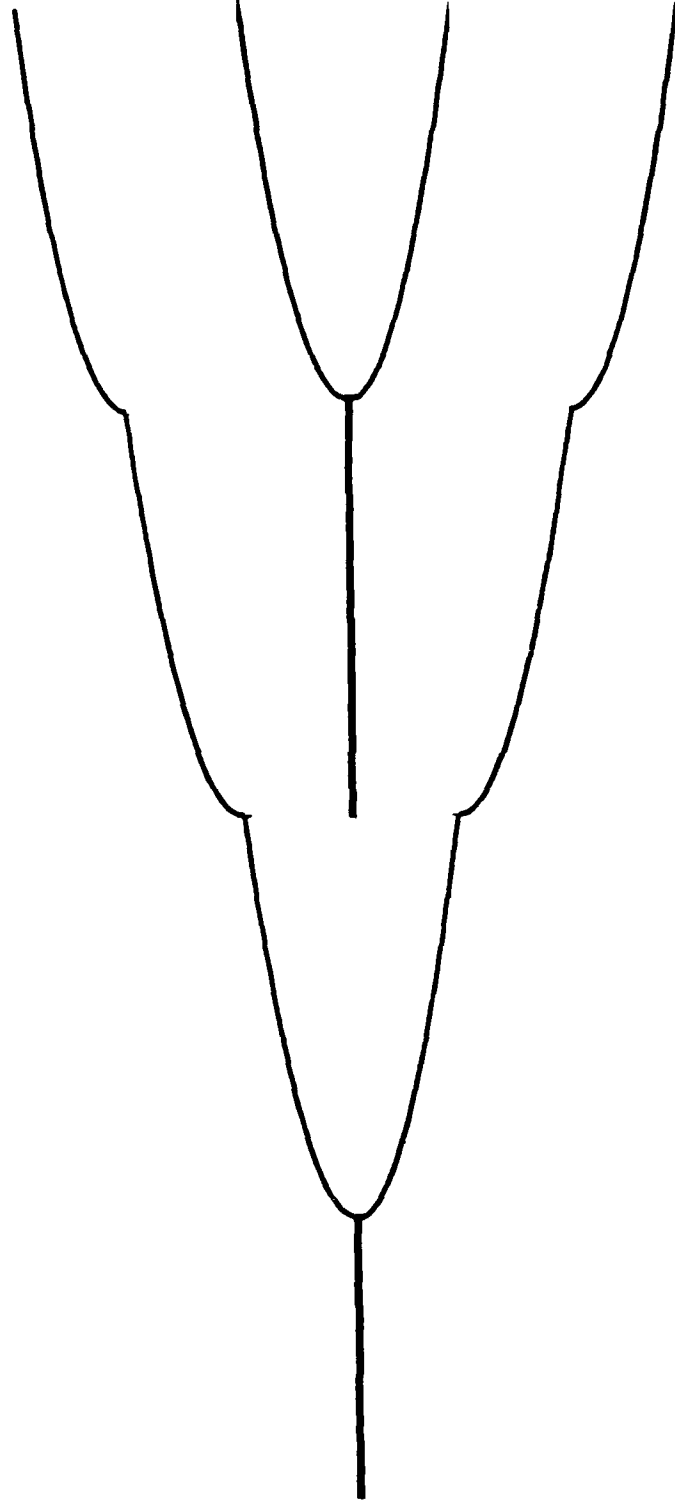
Dye Molecule Energy Level Structure



BAND MODEL EQUATIONS OF MOTION

$$\begin{aligned}
 \left[\frac{d}{dz} + \frac{1}{c} \frac{d}{dt} \right] E &= \kappa \left[\sum_n P_n - E \right] \\
 \dot{D} &= \lambda \left[D_c - \sum_n A_n - D - Y_d D - Y_d \left[\sum_n P_n^* E + \sum_n P_n E^* \right] \right] \\
 \dot{P}_n &= \left[-Y_p + i\Delta_n \right] P_n + Y_p E f_n \left[D - A_n \right] \\
 \dot{A}_n &= -Y_d A_n + Y_d f_n D + Y_d \left[\sum_n P_n^* E + \sum_n P_n E^* \right]
 \end{aligned}$$

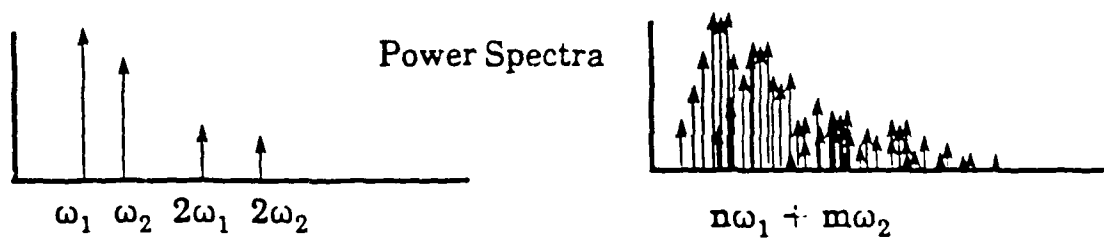
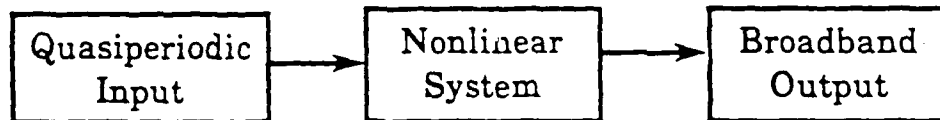
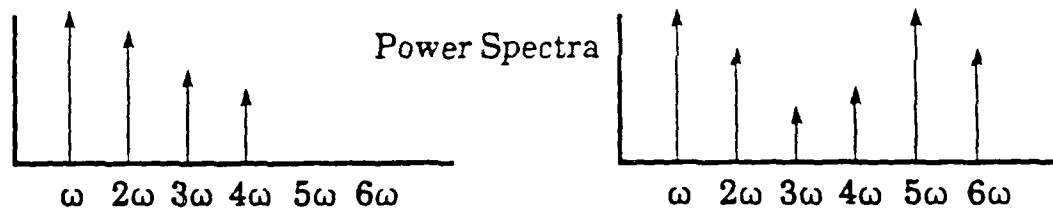
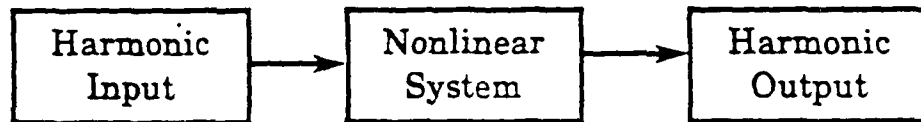
BAND MODEL PREDICTIONS



A series of multichromatic states of operation

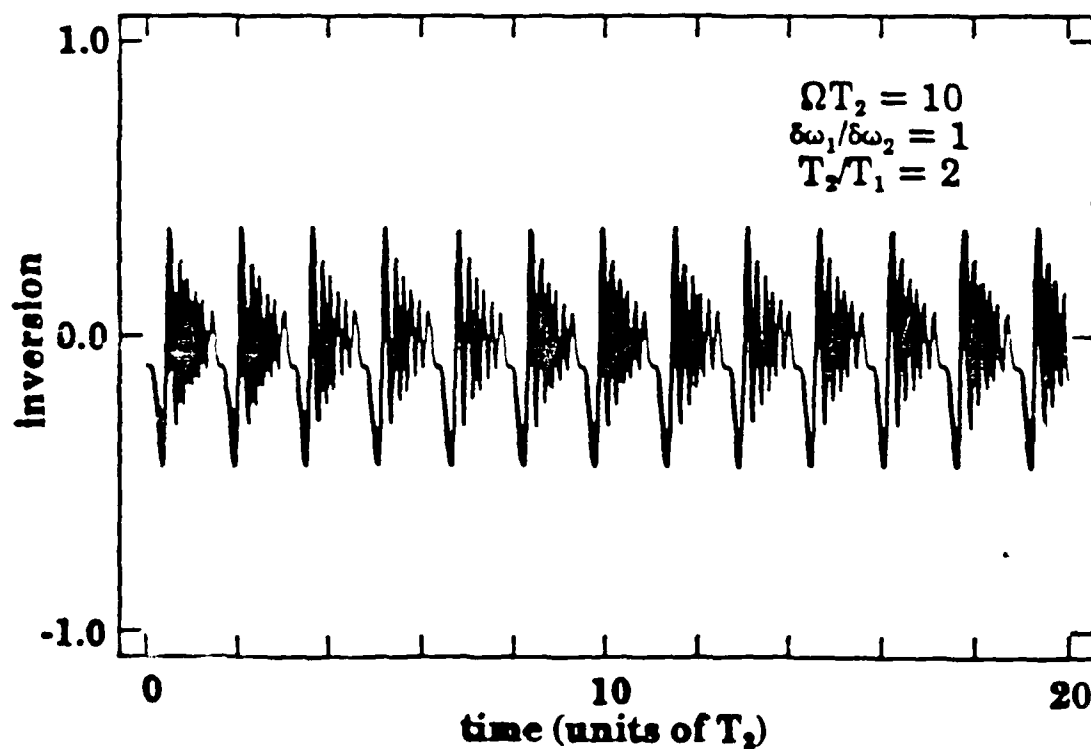
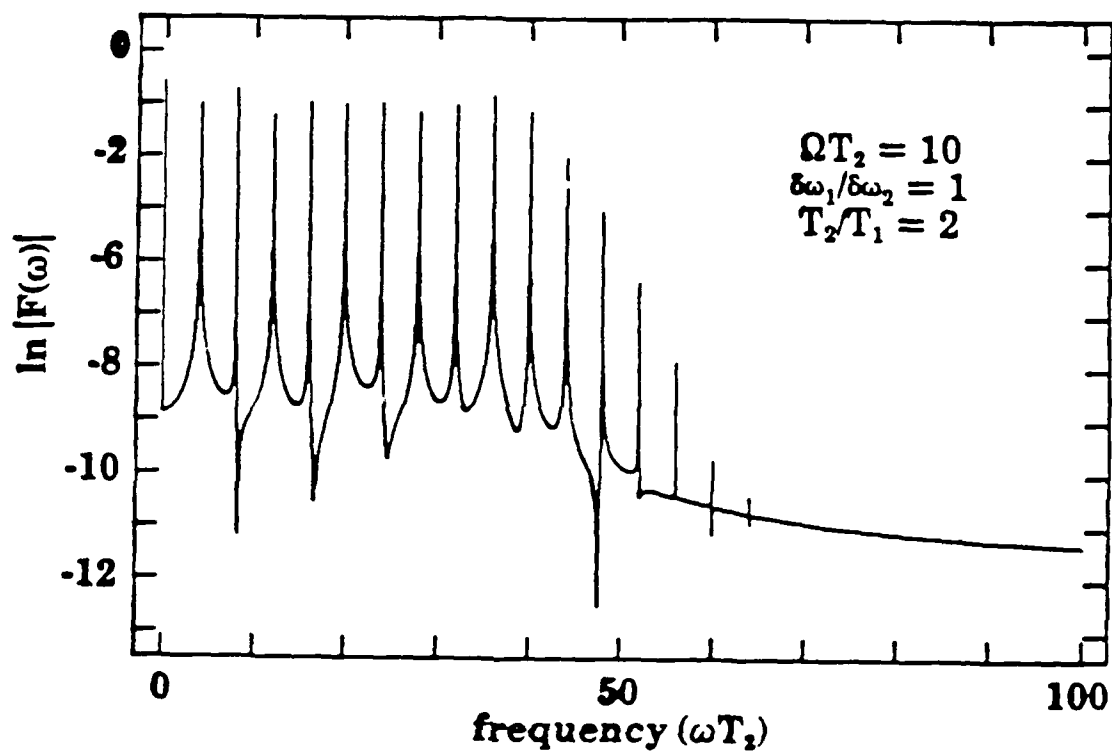
No hysteresis is predicted by the model except in the case where $Y_a > Y_d$.

BROADBAND OUTPUT

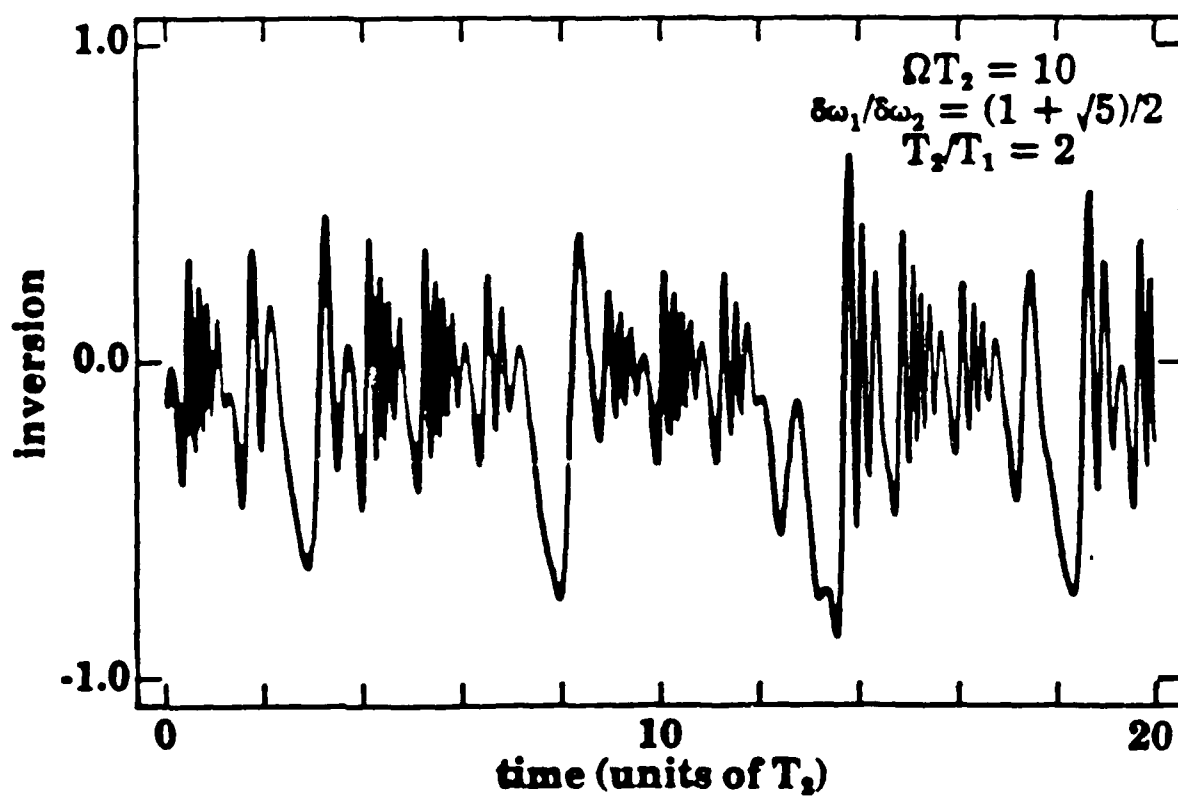
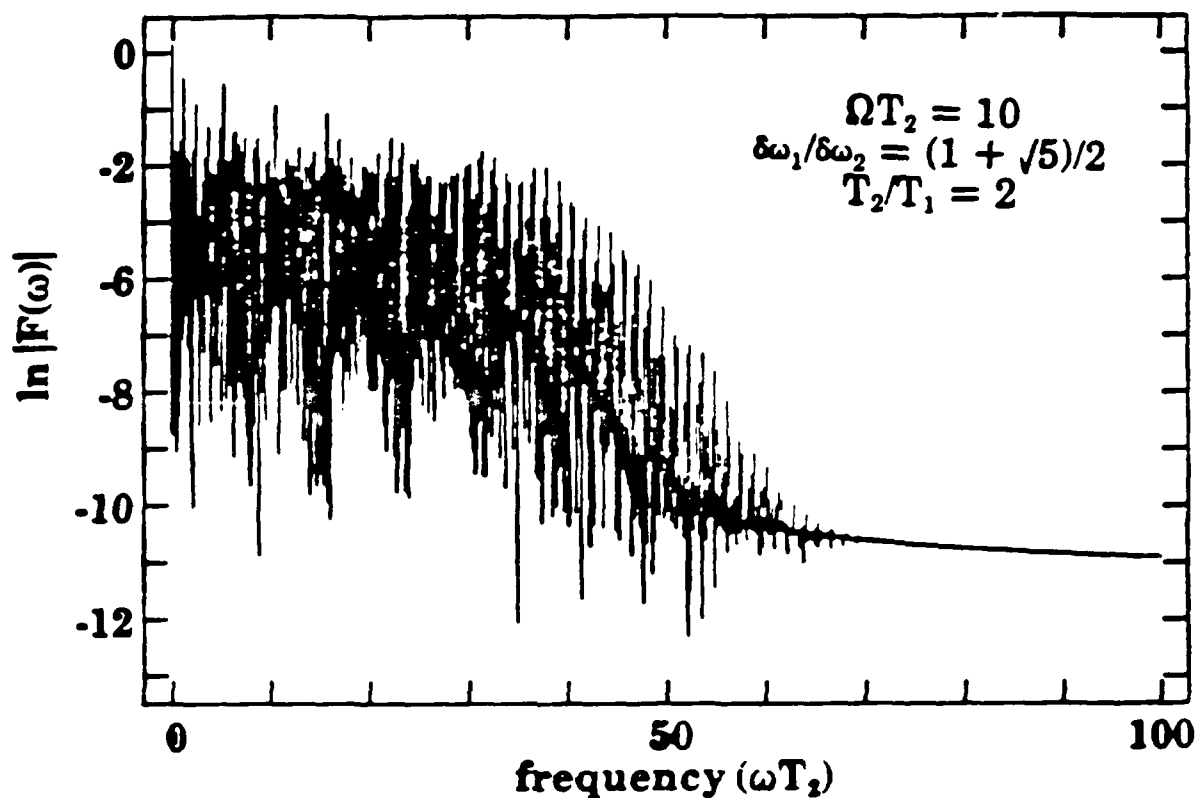


Driving nonlinear systems with two incommensurate frequencies can produce broadband output

RESULTS OF NUMERICAL CALCULATION COMMENSURATE MODULATION FREQUENCIES

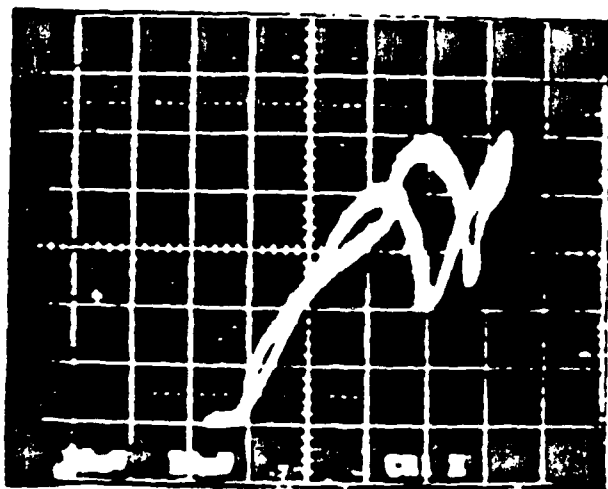
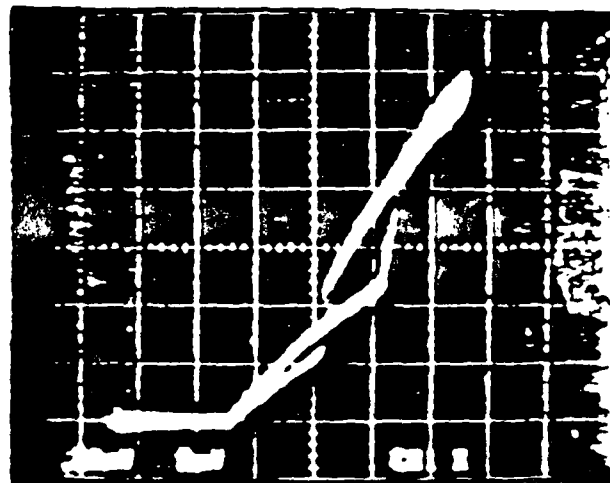
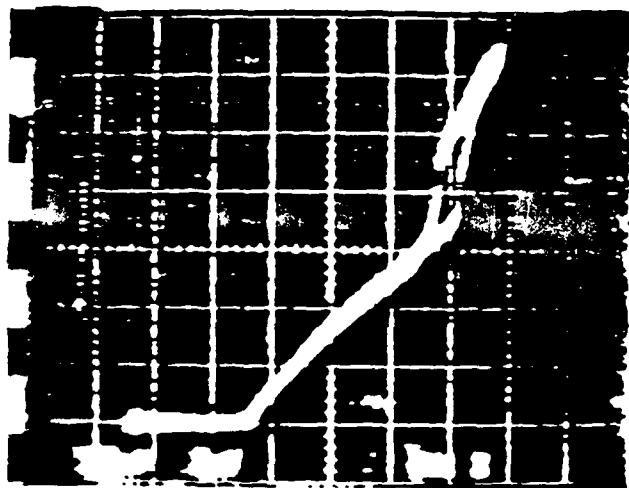


RESULTS OF NUMERICAL CALCULATION INCOMMENSURATE MODULATION FREQUENCIES

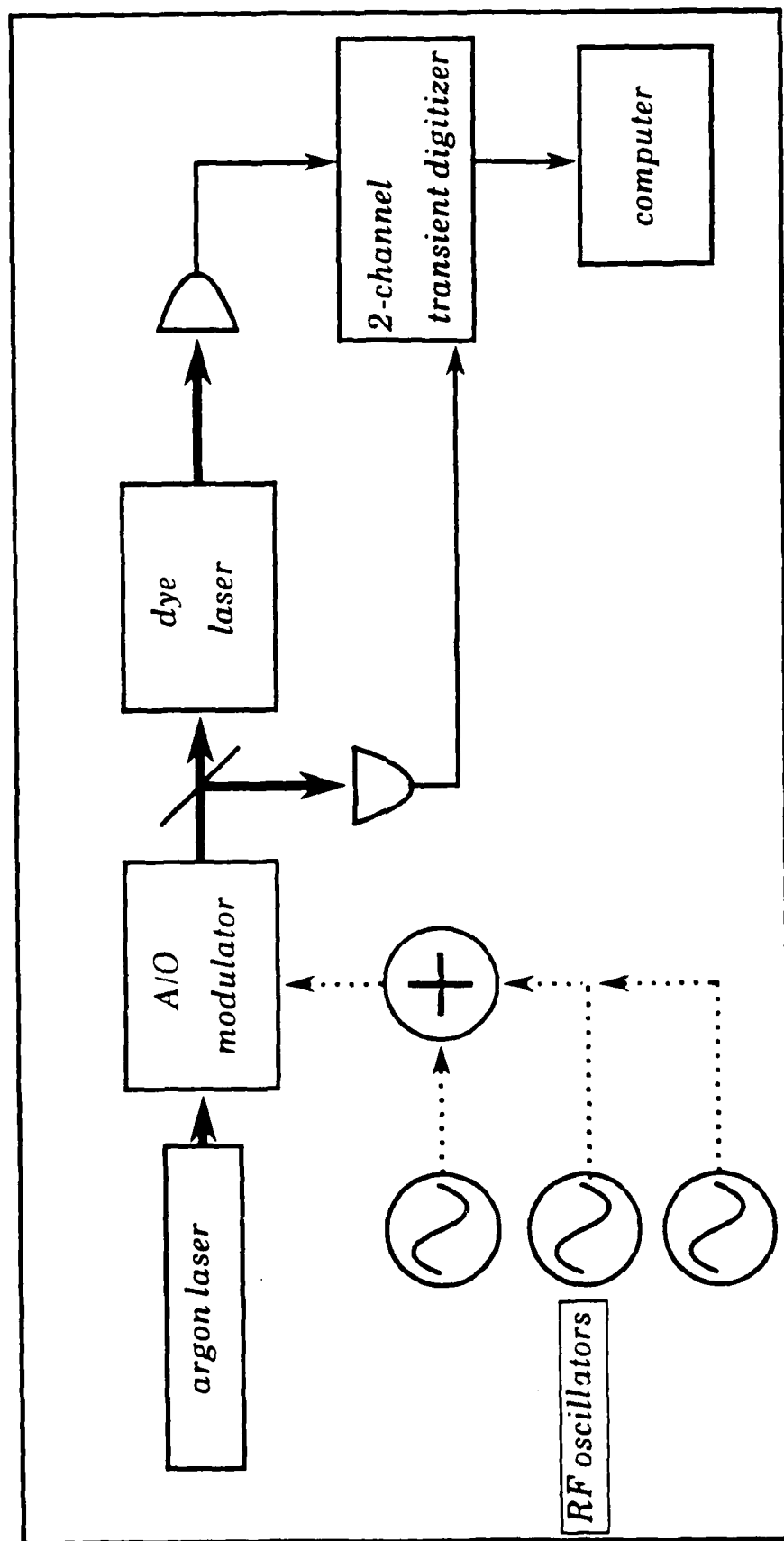


Dye Laser Output vs. Argon Laser Input: modulation above threshold

VARIOUS CAVITY CONFIGURATIONS

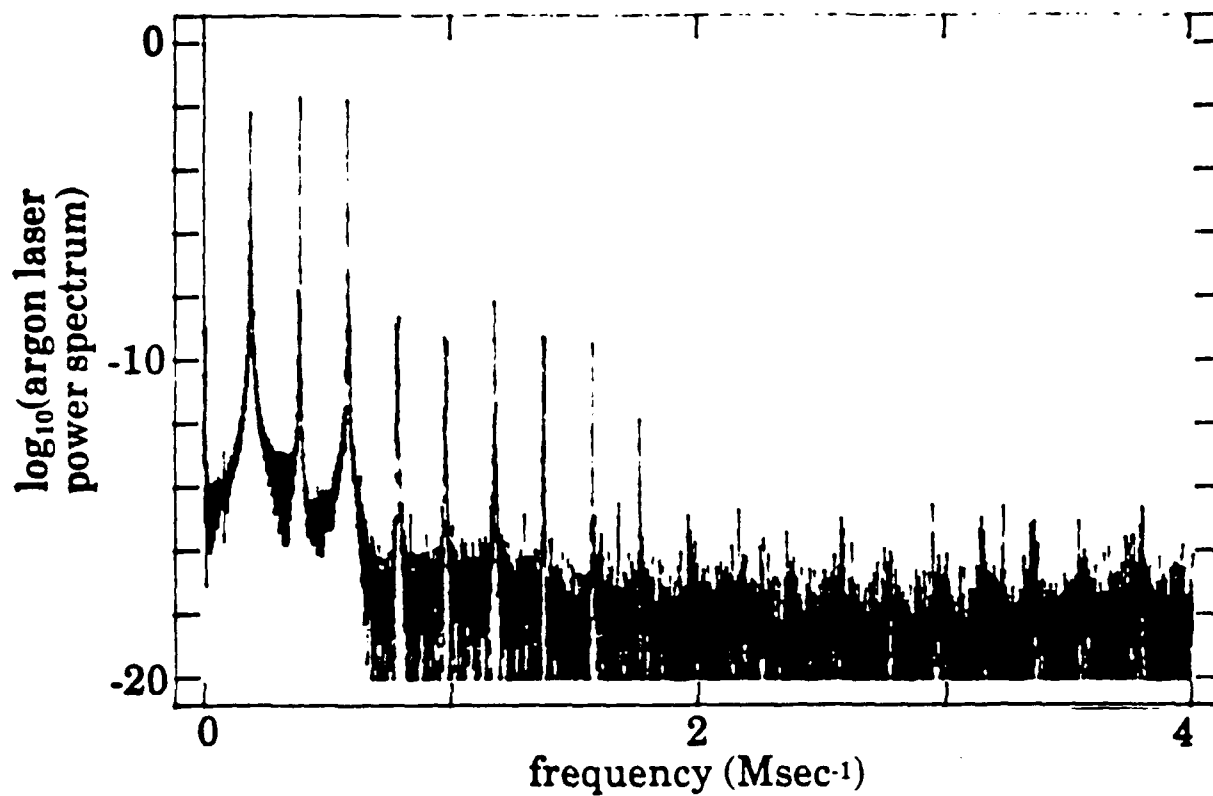


EXPERIMENTAL SETUP

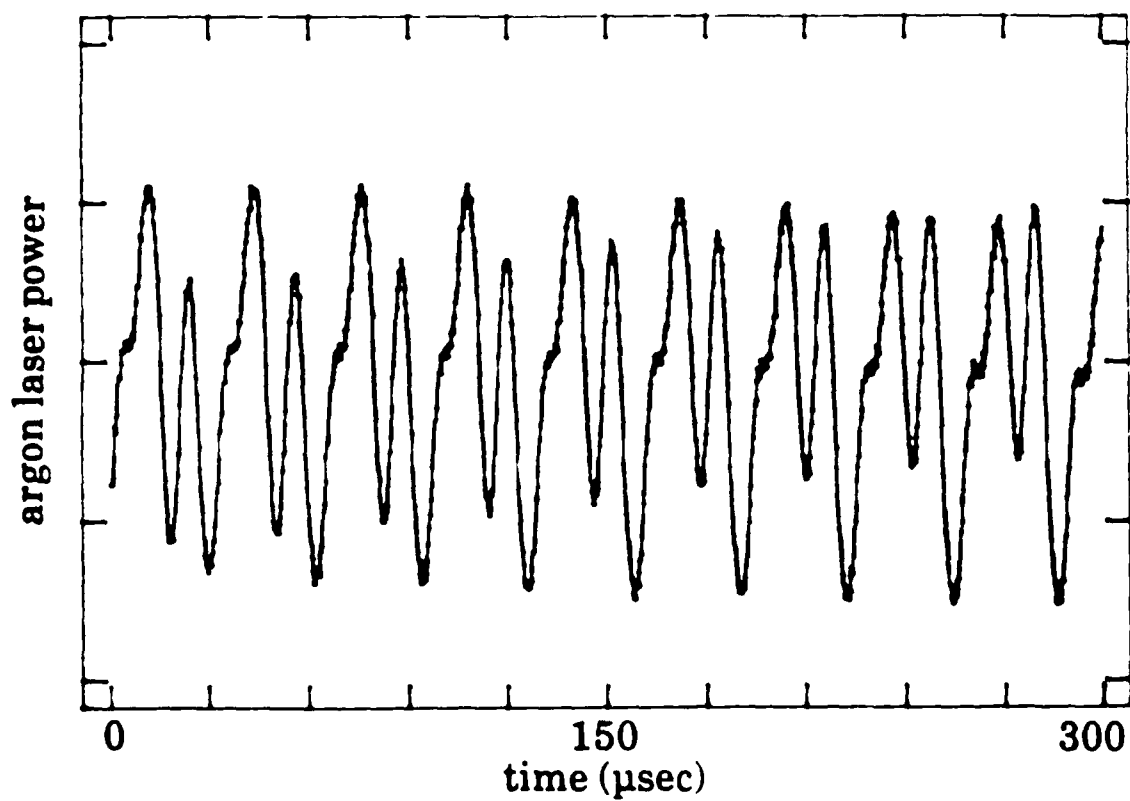


COMMENSURATE MODULATION FREQUENCIES

Input spectrum

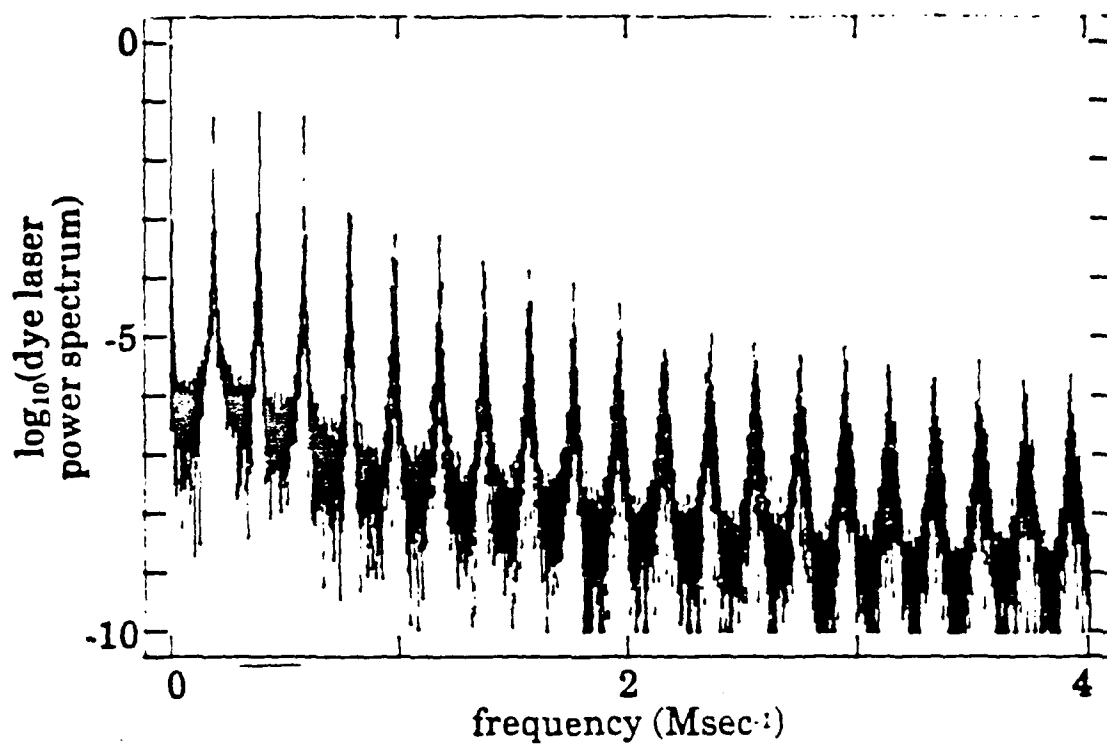


Input time series

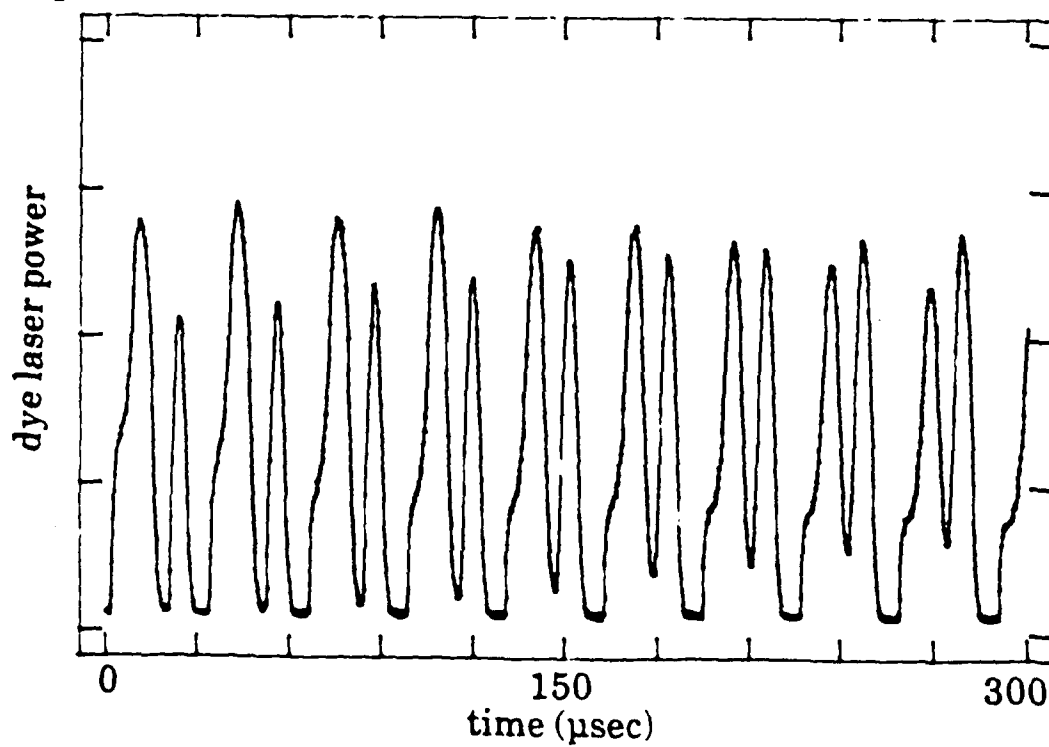


COMMENSURATE MODULATION FREQUENCIES

Output spectrum

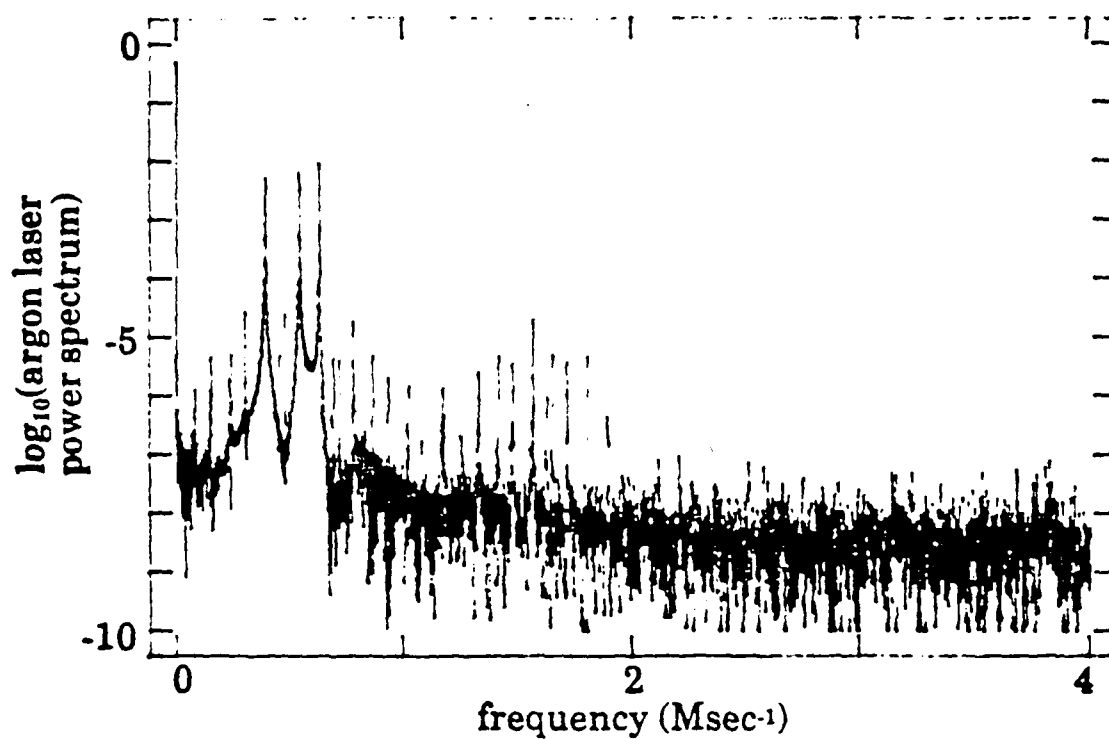


Output time series

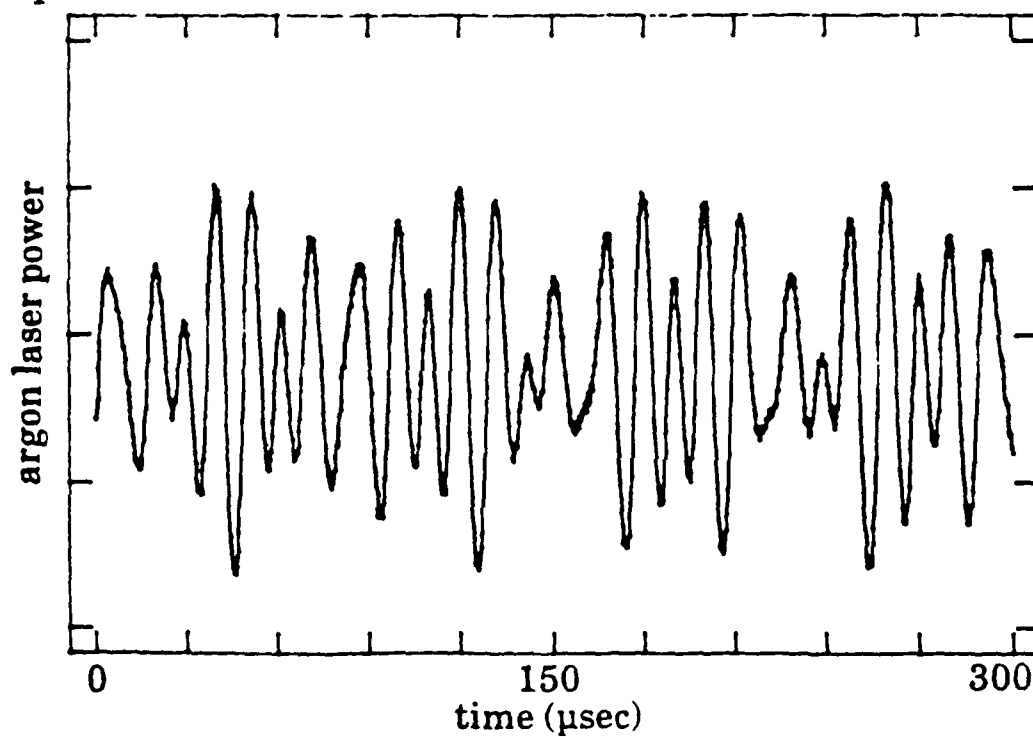


INCOMMENSURATE MODULATION FREQUENCIES

Input spectrum

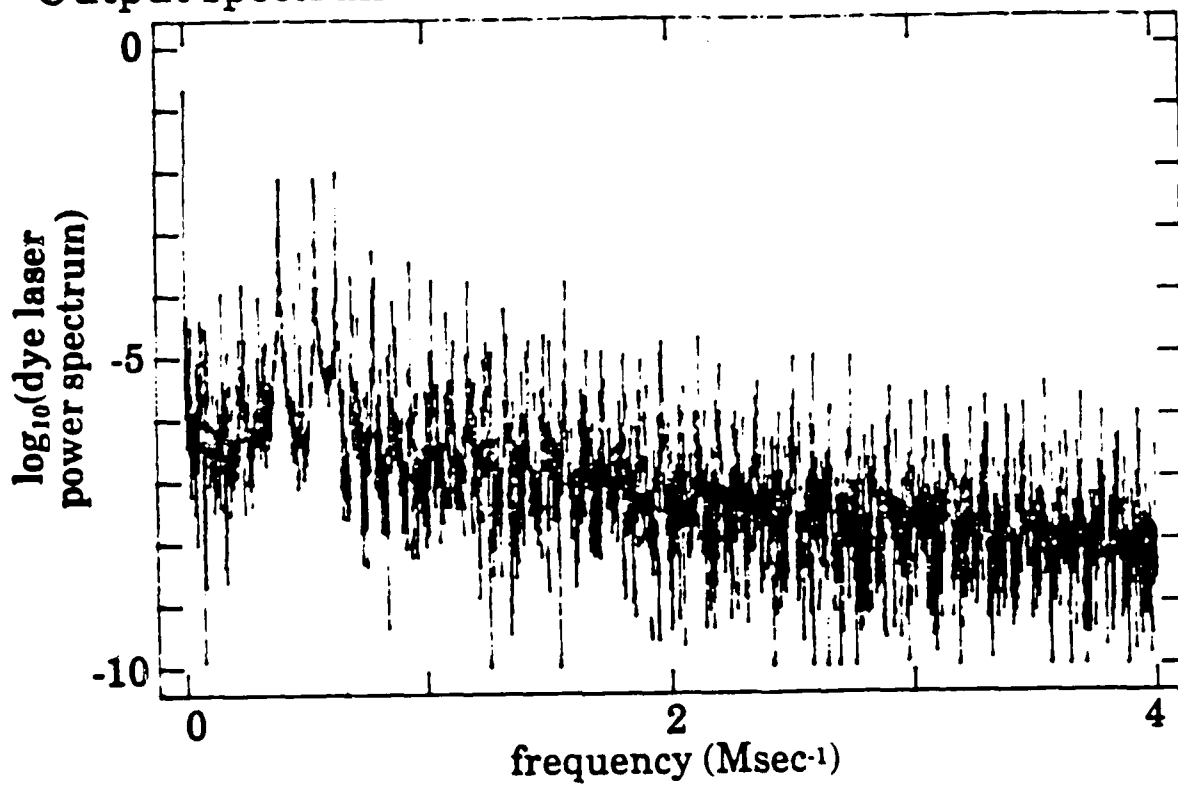


Input time series

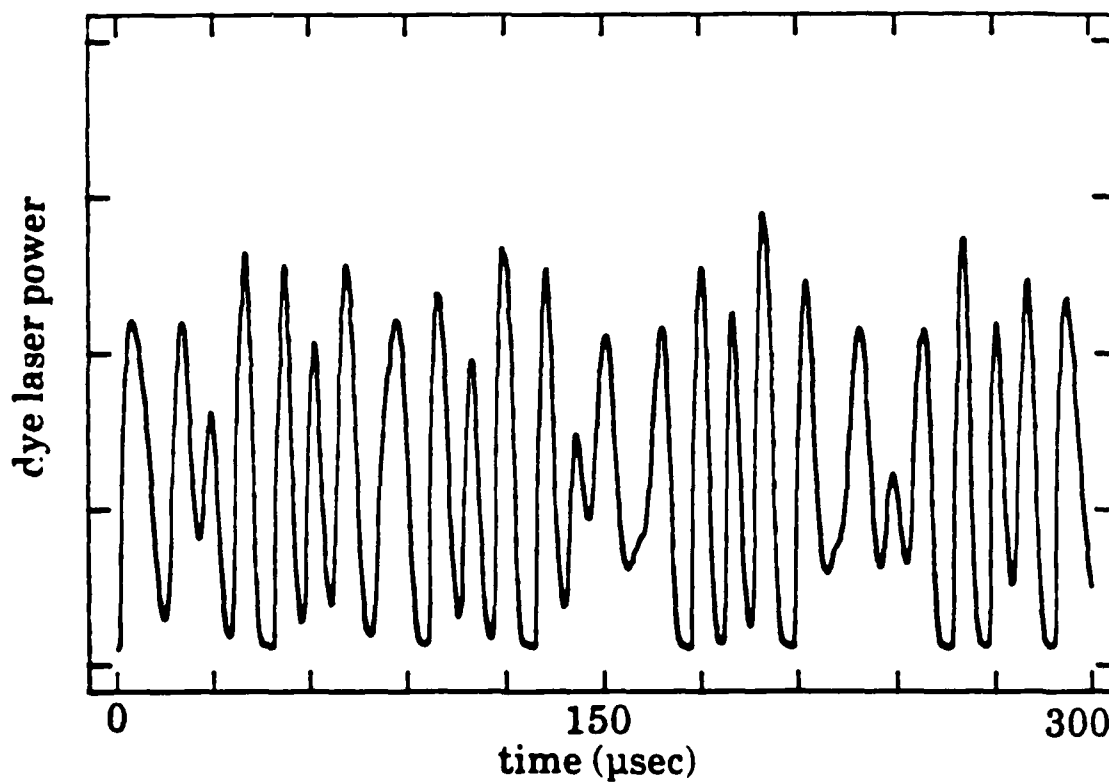


INCOMMENSURATE MODULATION FREQUENCIES

Output spectrum



Output time series



**CENTER FOR OPTO-ELECTRONIC SYSTEMS RESEARCH
MODULATION TECHNIQUES: ALEXANDRITE LASERS**

Modulation Techniques in Homogeneous Systems to Determine Decay Rates

hole burning

inhomogeneous broadening

homogeneous broadening

pump-probe techniques

AM modulation techniques

AM sensitivity (lock-in detection)
FM noise insensitive
single laser experiment

Applications of AM Spectroscopy

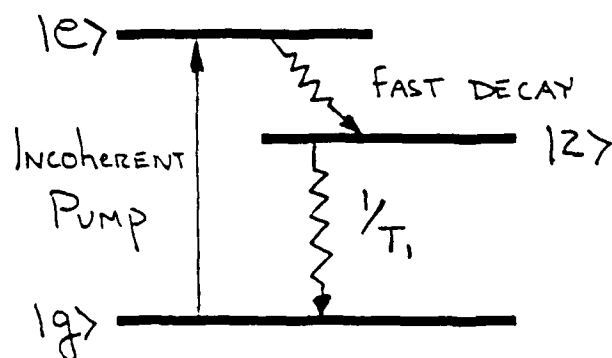
probe gain, or absorption in presence of saturating field

single mode stability analysis

measure "hidden" non-radiative decay rates

sensitivity of gain transition to pump noise

Three Level Systems

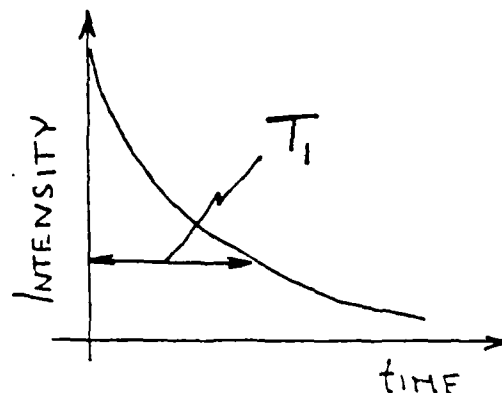


$1/T_1$ - Population Decay RATE

Fluorescent Decay Rate

$$p_2(t) = p_2(0) e^{-t/T_1}$$

TURN OFF PUMP AND MONITOR the FLUORESCENCE

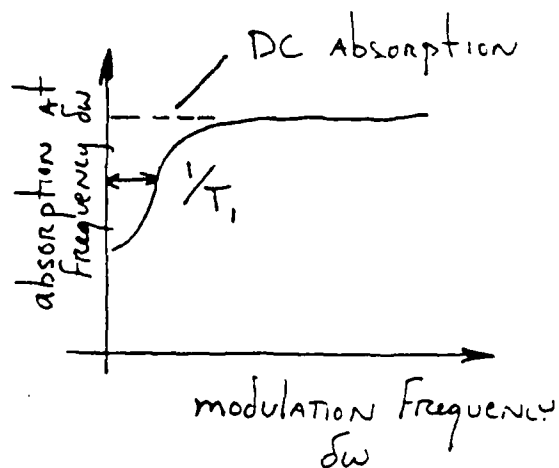


Modulation Measurement

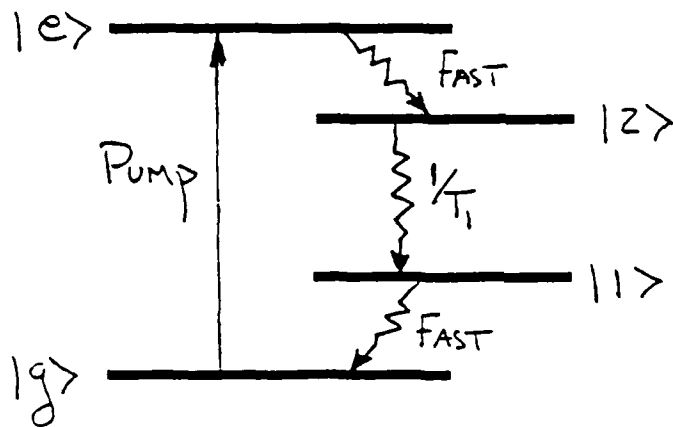
MODULATE the Pump at $\delta\omega$

$$\alpha = \frac{\alpha_0}{1+I_0} \left\{ 1 - \frac{2I_0(1+I_0)}{(1+I_0)^2 + (\delta\omega T_1)^2} \right\}$$

$$I_0 = \frac{I}{I_{SAT}}$$



Four Level Systems



"IDEAL" FOUR-LEVEL
SYSTEM

fluorescent emission rate measurement
cannot determine if non-radiative decay
from level 1 is slow

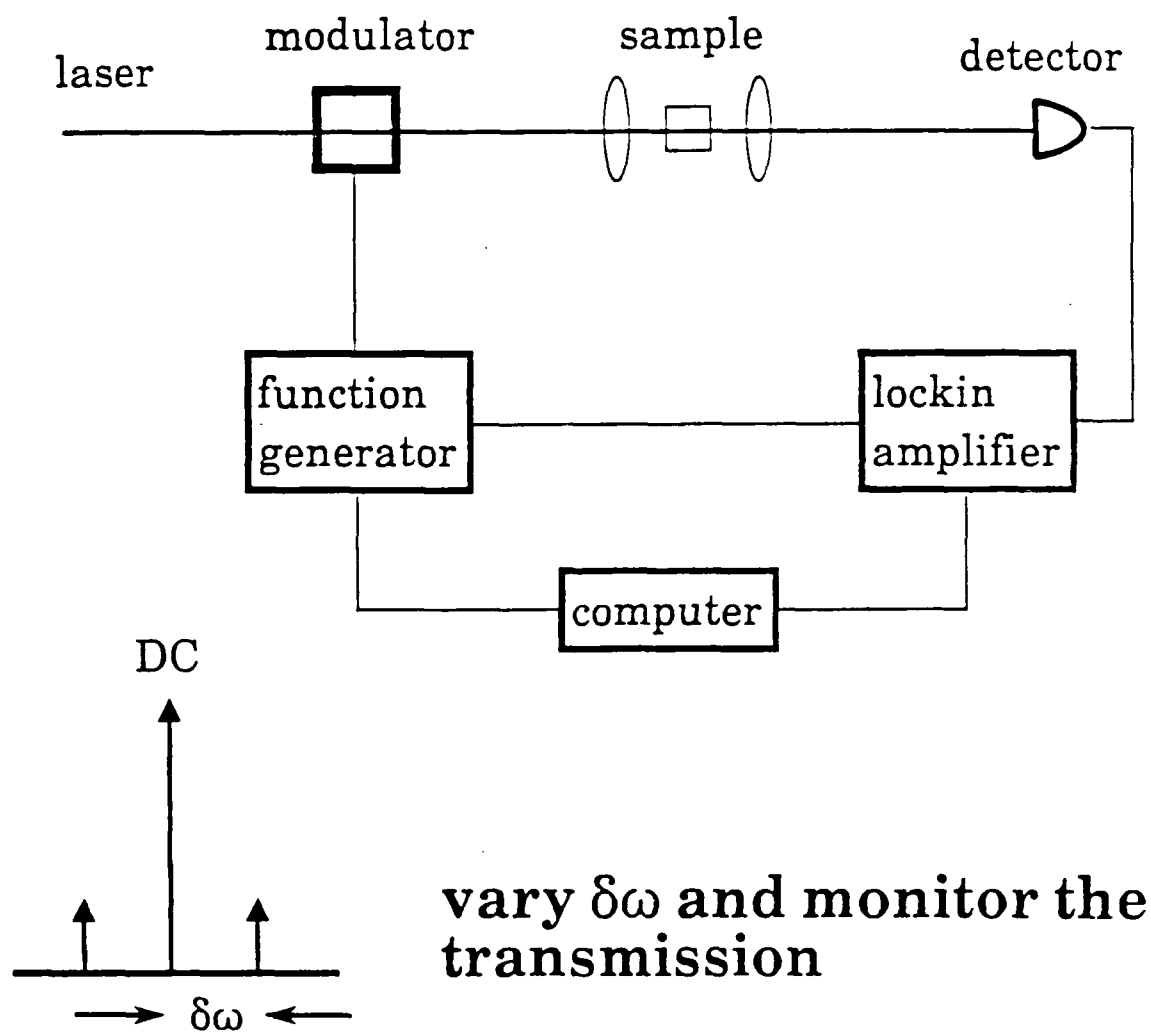
modulation measurement determines the
population cycling rate

slow decay from level 1 may cause
instabilities

Single Laser AM Experiments

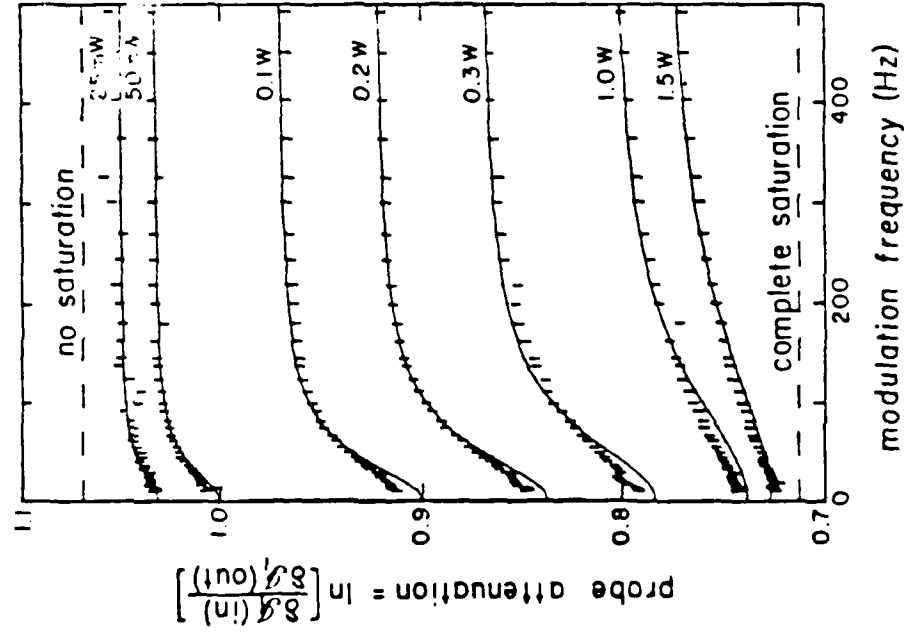
ruby

alexandrite

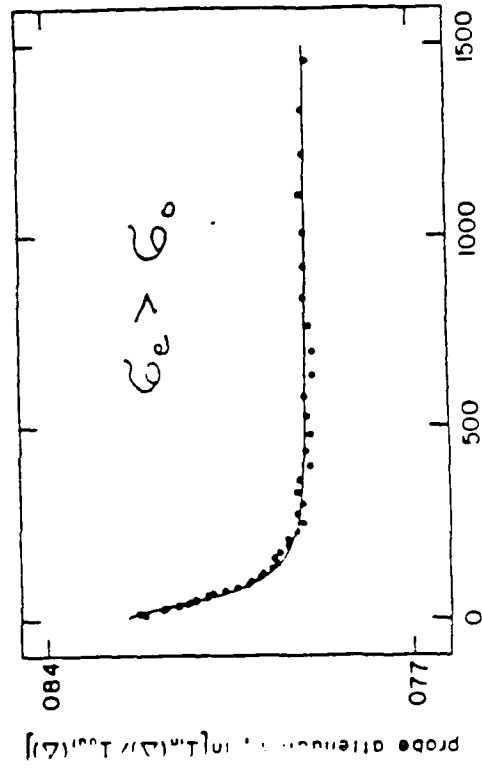
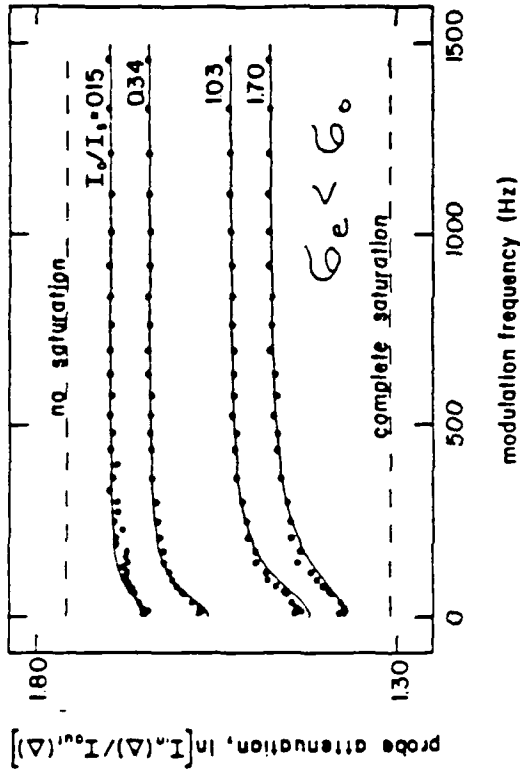


Single Laser AM Data

RUBY DATA



ALEXANDRITE DATA



Results of Single-Laser AM Experiments

a hole in the absorption spectrum of the probe fields is observed centered at DC

the hole has width $1/T_1$ for weak DC field strength

hole broadens as $1 + I / I_{\text{sat}}$

discrepancy with known $1/T_1$ rate in ruby

alexandrite reveals anti-hole due to excited state absorption

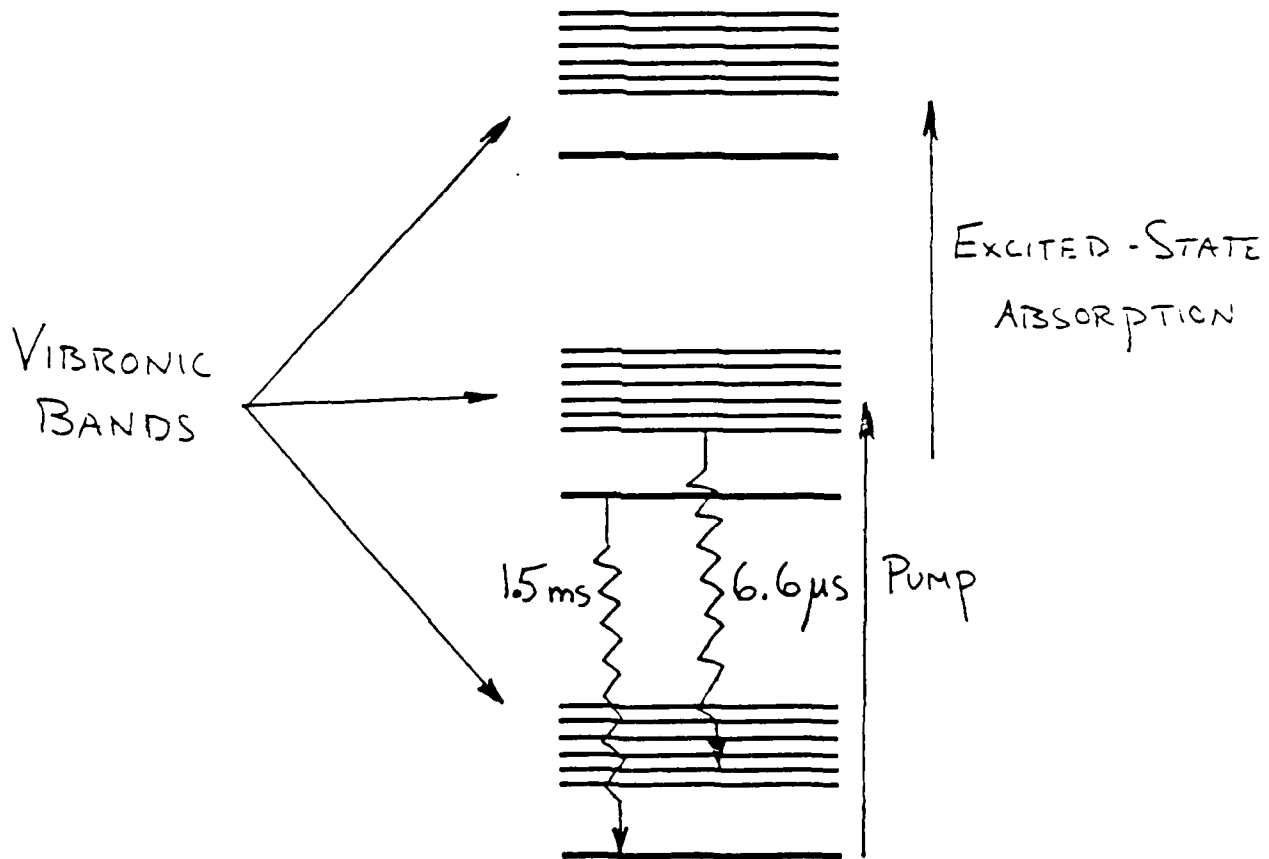
Alexandrite Level Structure

can operate as a three level laser similar to ruby

1.5 ms TRANSITION

can operate as a four level laser similar to dyes, a vibronic laser

6.6 μ s TRANSITION



Rate Equation Approximation

consider a two level system

optical Bloch equations:

$$\dot{u} = -u/T_2 - \Delta v$$

$$\dot{v} = \Delta u - v/T_2 + \kappa E(t)w$$

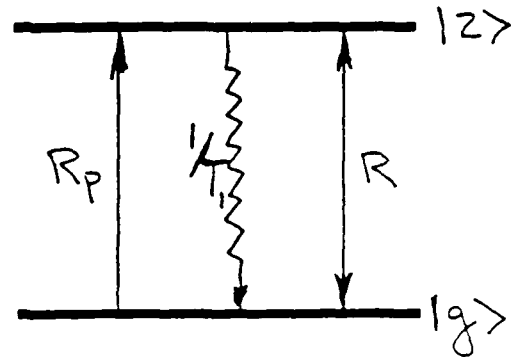
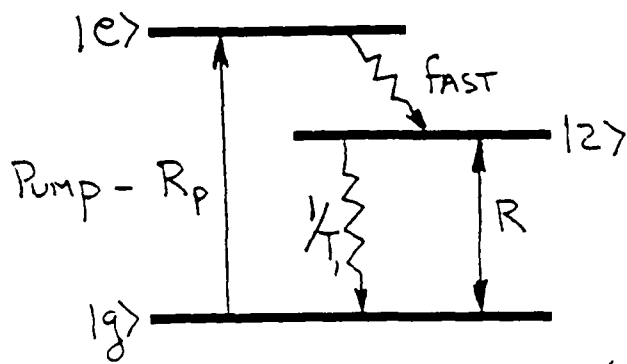
$$\dot{w} = -(w - w_{eq})/T_1 - \kappa E(t)v$$

collisional broadening, $1/T_2 \gg 1/T_1$

rate equation limit

Reduced Rate Equations

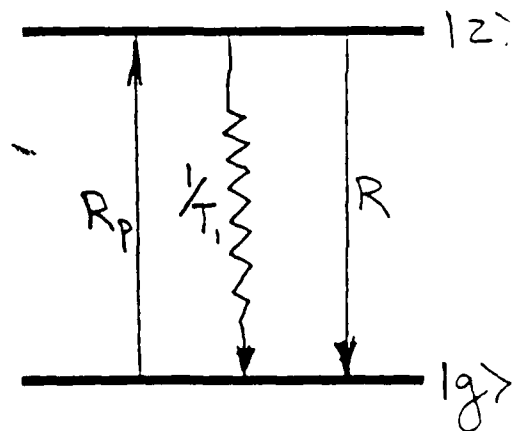
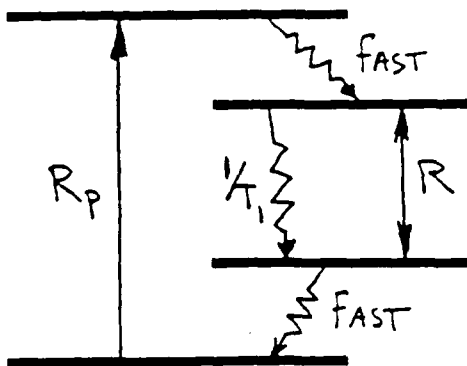
Three Level System



$$\dot{\rho}_e = (R_p + R) - (R_p + 2R + 1/T_1) \rho_e$$

$$\dot{\rho}_g = (1/T_1) - (R_p + 2R + 1/T_1) \rho_g$$

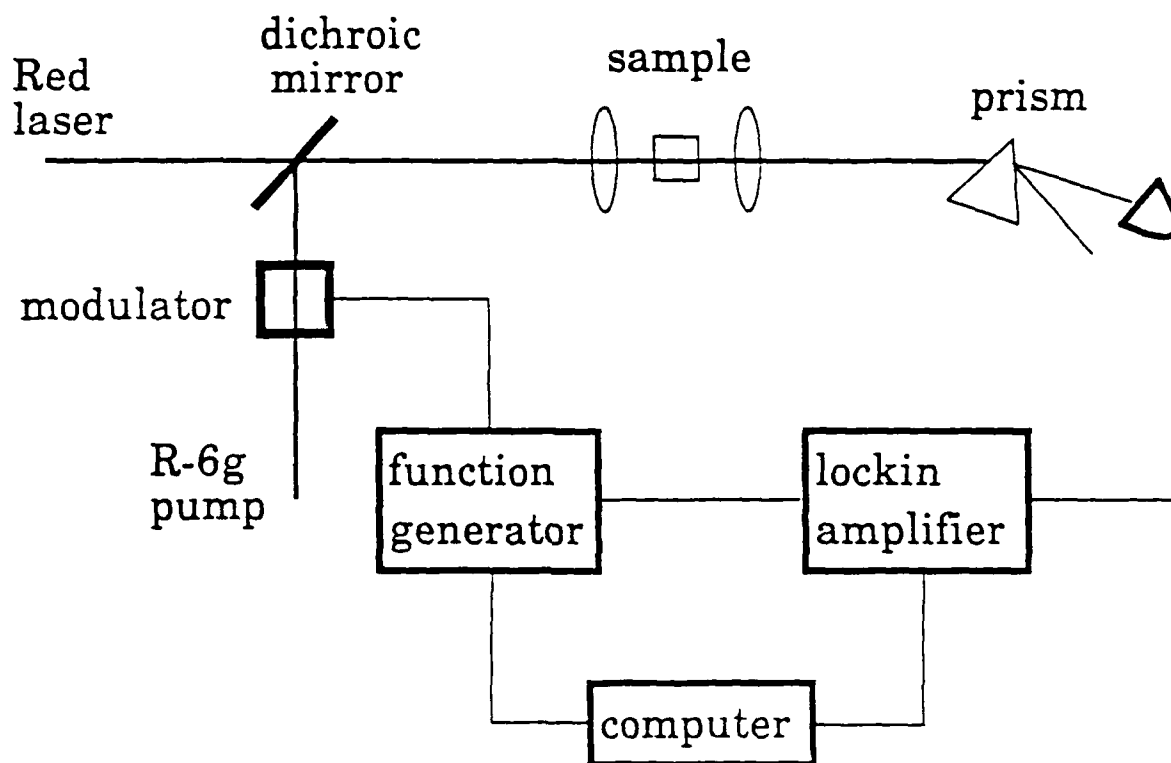
Four Level System



$$\dot{\rho}_e = (R_p) - (R_p + R + 1/T_1) \rho_e$$

$$\dot{\rho}_g = (R + 1/T_2) - (R_p + R + 1/T_1)$$

Multi-Level Two Laser AM Spectroscopy

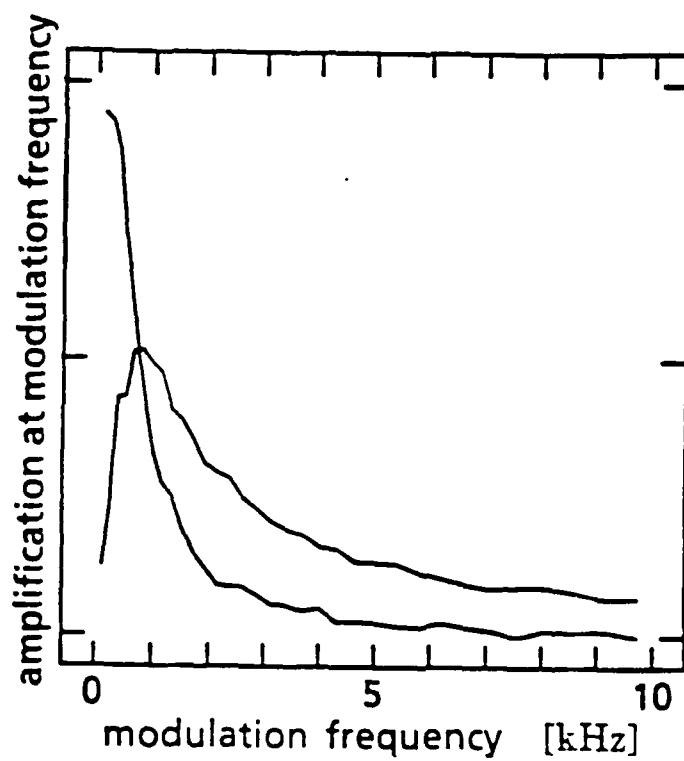


Experiments

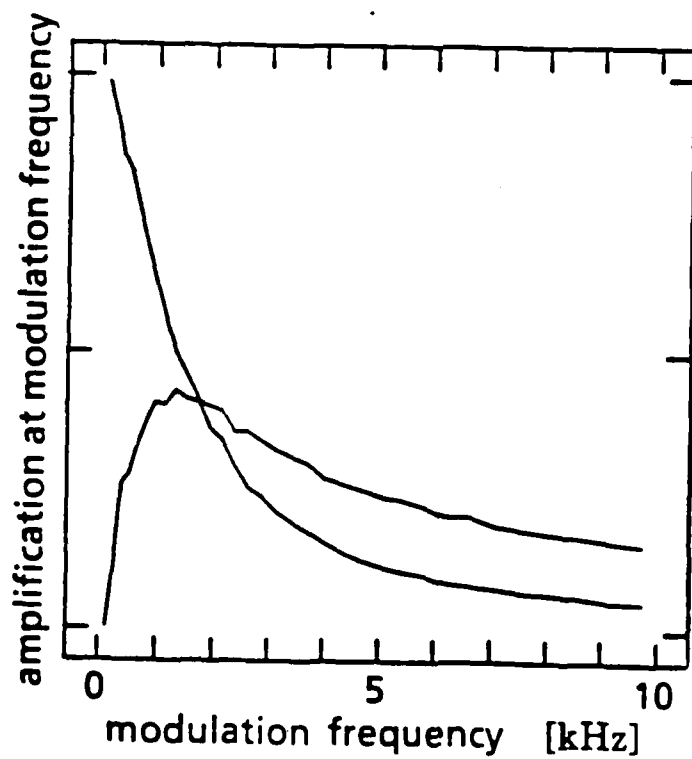
modulate pump to study pump noise

modulate laser tuned to inverted
transition to study single mode stability

Data

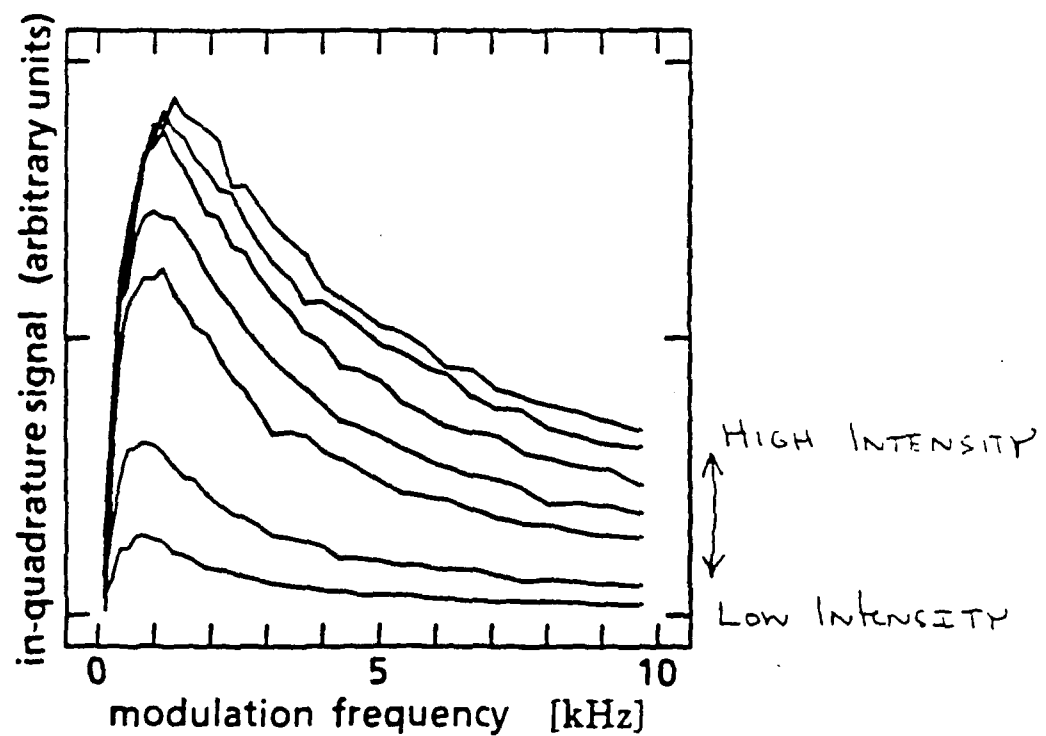
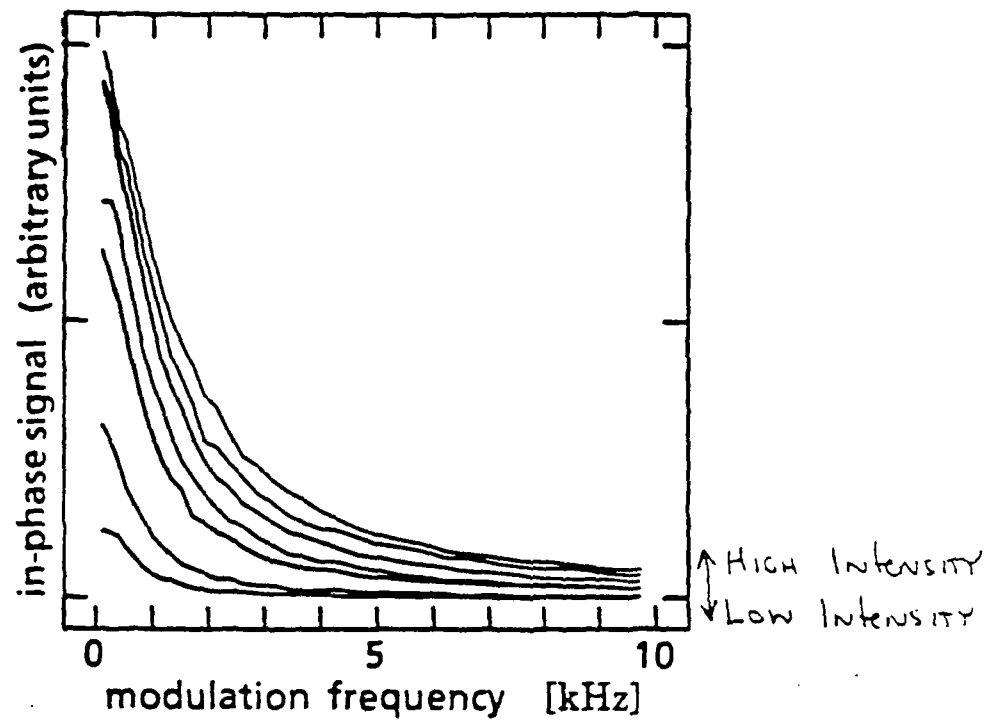


LOW
INTENSITY

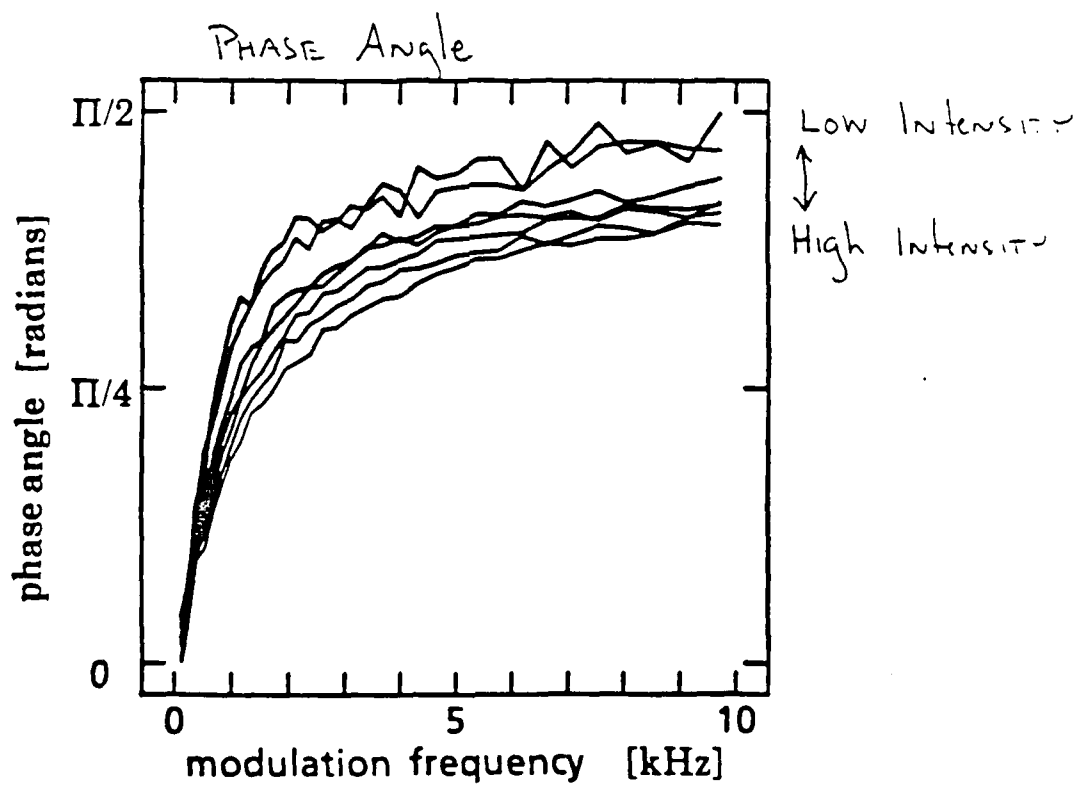
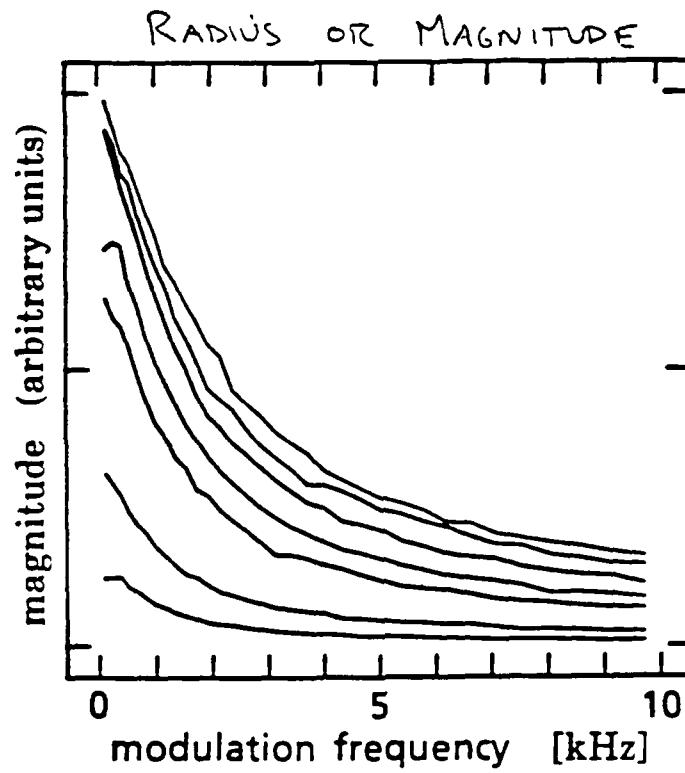


HIGH
INTENSITY

In-Phase and In-Quadrature

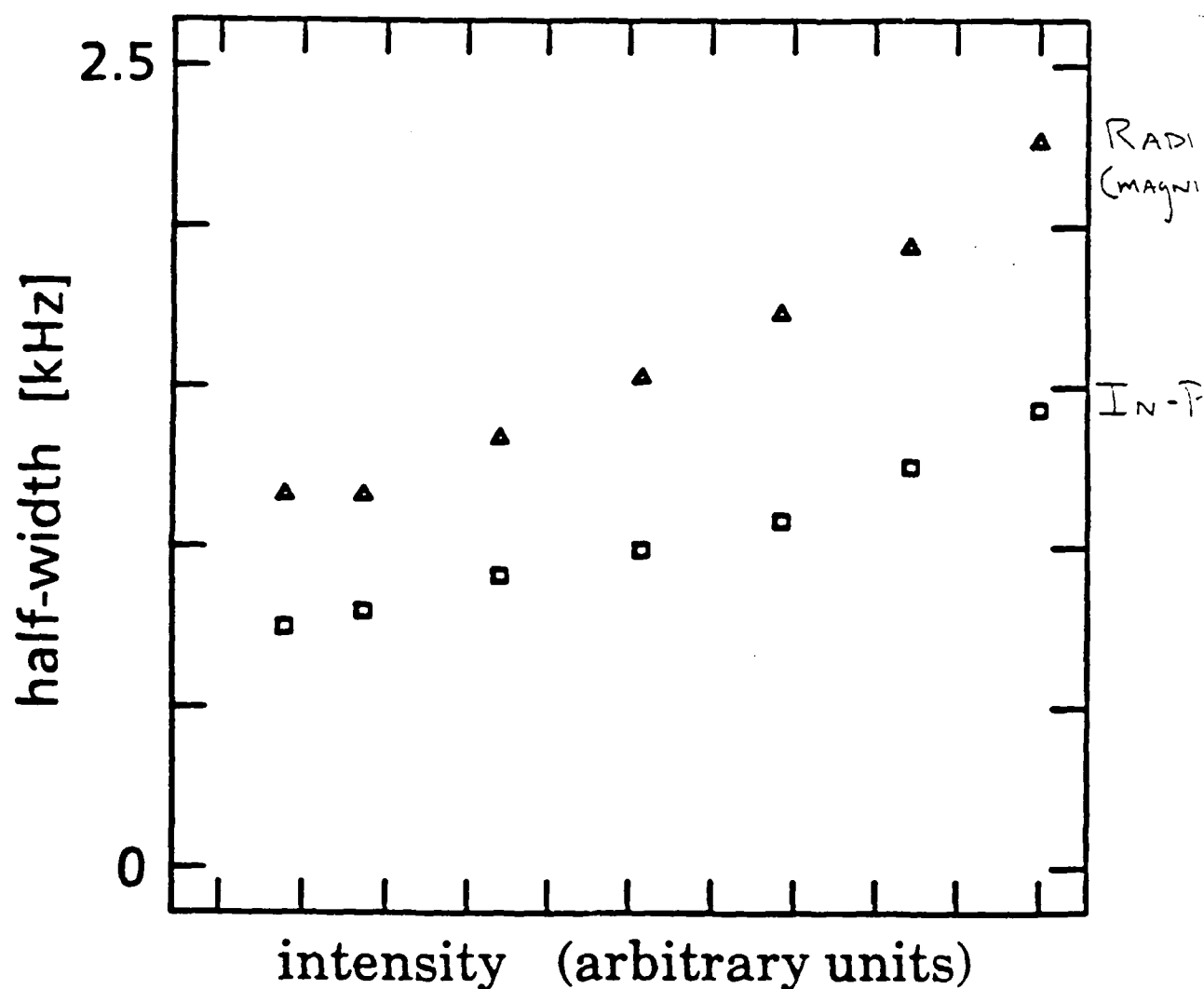


Magnitude and Angle



Variation of Half-Widths with Intensity

* WIDTH OF IN-PHASE SIGNAL should be
600 Hz, $1/T_1$ DECAY RATE AT
LOW INTENSITY



References for AM Spectroscopy

1. L.W. Hillman, R.W. Boyd, and C.R. Stroud, Jr. "Natural Modes for the Analysis of Optical Bistability and Laser Instability", Opt. Lett. **7**, 149-151, (1982).
2. L. W. Hillman, R. W. Boyd, J. Krasinski, and C. R. Stroud, Jr., "Observation of a Spectral Hole Due to Population Oscillations in a Homogeneously Broadened Optical Absorption Line", Opt. Comm., **65**, (1983).
3. M. S. Malcuit, R. W. Boyd, L. W. Hillman, J. Krasinski, and C. R. Stroud, Jr., "Saturation and Inverse-Saturation Absorption Line shapes in Alexandrite", J. Opt. Soc. Am. B, **1**, 73-75, (1984).
4. M. A. Kramer, R.W. Boyd, L. W. Hillman, and C. R. Stroud, Jr., "The Propagation of Modulated Optical Fields Through Saturable-Absorbing Media: A General Theory of Modulation Spectroscopy", J. Opt. Soc. Am. B **2**, Sept. (1985).

Laser Instability Publications

"Observation of Higher Order Dynamical States of a Homogeneously Broadened Laser," L.W. Hillman, J. Krasinski, R.W. Boyd, and C. R. Stroud, Jr., *Phys. Rev. Lett.* 52, 1605-1608 (1984).

"Dynamics of Homogeneously Broadened Lasers: Higher-Order Bichromatic States of Operation," L. Hillman, J. Krasinski, K. Koch, and C. R. Stroud, Jr., *J. Opt. Soc. Am. B* 2, 211-217 (1985).

"Propagation of Modulated Optical Fields Through Saturable-Absorbing Media: A General Theory of Modulation Spectroscopy," M.A. Kramer, R.W. Boyd, L.W. Hillman, and C.R. Stroud, Jr., *J. Opt. Soc. Amer. B* 2, 1444-1455 (1985).

"Instabilities and Higher-Order States of CW Ring Dye Lasers," K. Koch, S. Chakmakjian, and C. R. Stroud, Jr., in *Optical Instabilities* ed. R. W. Boyd, M. G. Raymer and L. M. Narducci, (Cambridge University Press, New York, 1986) pp. 274-276.

"Multimode Instabilities of Homogeneously Broadened Lasers," S. Chakmakjian, L.W. Hillman and, K. Koch, and C. R. Stroud, Jr., in *Optical Bistability III*, editors H. M. Gibbs, P. Mandel, N. Peyghambarian, and S. D. Smith (Springer Verlag, New York, 1986), pp 345-347.

"Multimode Instabilities in cw Dye Lasers," K. Koch, S. Chakmakjian, and L. W. Hillman, and C. R. Stroud, Jr., *Proceedings of SPIE Conference on Optical Chaos*, editors N. B. Abraham and J. Chrostowski, (SPIE, Bellingham, WA, 1986).

"Laser Instabilities," C. R. Stroud, Jr., in Proceedings of Twelfth International Nathiagali Summer College on Physics and Contemporary Needs, (1987).

"Observation of Resonances at Sub-Harmonics of the Rabi Frequency in the Saturated Absorption of a 100% Amplitude Modulated Laser Beam," S. Chakmakjian, K. Koch, and C. R. Stroud, Jr., *J. Opt. Soc. Amer B* 5, 2015 (1988).

"Subharmonic Instabilities in Resonant Interactions with Bichromatic Fields," Karl Koch, Brian J. Oliver, Stephen H. Chakmakjian, Lloyd W. Hillman, and C. R. Stroud, Jr., *J. Opt. Soc. Amer. B* 6, xxx (1989).

"Effects of Pump Modulation on a Four-Level Laser Amplifier," Stephen Chakmakjian, Karl Koch, Stephano Papademetriou, and C. R. Stroud, Jr., *J. Opt. Soc. Amer. B* 6, xxx (1989).

"Modulation Mixing in a Dye Laser," Karl Koch, Stephen H. Chakmakjian, Stephano Papademetriou, and C. R. Stroud, Jr., *Phys. Rev. A* 39, xxx (1989).

**Observation of resonances at sub-harmonics of the Rabi frequency in the saturated
absorption of a 100% amplitude modulated laser beam**

Stephen Chakmakjian, Karl Koch, and C.R. Stroud, Jr.

The Institute of Optics

University of Rochester

Rochester, NY 14627

Abstract

A series of resonances has been observed in the absorption of a 100% amplitude-modulated laser beam by an optically pumped sodium atomic beam. Resonances were observed when the modulation frequency was equal to the first, second, and third subharmonic of the Rabi frequency. The experimental results are compared with theory and the implications of these parametric resonances to laser instabilities are discussed.

INTRODUCTION

Researchers in the fields of modulation spectroscopy, optical bistability and laser instability have become interested in the interaction of intense, strongly modulated fields with atomic systems¹⁻⁷. A 100% amplitude-modulated (AM) field is a special case of strong modulation since the energy at the carrier frequency has been completely transferred into the modulation sidebands. In this paper we study the interaction of a 100% AM laser field with an ensemble of homogeneously broadened two-level atoms.

Under the influence of a strong resonant field the atomic variables undergo Rabi oscillations. If, in addition to the strong pump field, a weak probe field is applied, the probe field will see a complicated structure in its absorption spectrum due to the presence of the strong field. When it is detuned from the strong field by the strong-field Rabi frequency the probe field experiences a resonance in its absorption spectrum.⁸⁻¹⁰ These results have been experimentally confirmed¹¹⁻¹³. Sargent *et al.*¹⁴ have shown how modulation techniques can be employed to probe the saturated absorption of these strongly driven atoms. Modulation techniques alleviate the need for a second laser. Instead, the strong field is weakly modulated at a tunable frequency and the modulation sidebands probe the saturated absorption. Hillman *et al.*¹⁵ and Kramer *et al.*¹⁶ showed that the behavior seen in the absorption spectrum of the probe field is a result of the atomic response to the modulation tone in the field intensity. In their analysis they treated the interaction with the strong field to all orders, while the interaction with the sidebands was treated perturbatively. In the case of multiple strong fields it is necessary to treat all the field components and the combination tones to all orders.

Although the treatment of strong-modulation interactions is by no means complete, there has been experimental work in this area.^{17,18} These strong-modulation experiments yield different results from those seen in weak-modulation experiments. The atomic variables exhibit resonant behavior when the modulation frequency is approximately equal to the Rabi frequency or any subharmonic of the Rabi frequency. Bonch-Breuvich *et al.*¹⁷ performed an experiment with two strong radio-frequency fields tuned to a Zeeman

resonance in cadmium. One radio-frequency field was held at a constant frequency as the other field was tuned about the resonance to obtain an absorption spectrum. The absorption spectrum of the rf fields exhibited several subharmonic resonances. Thomann¹⁸ performed a three-field experiment at the sodium D₂ line resonance. The field was produced by strongly modulating a laser beam; the Rabi frequency was varied while the modulation frequency was held fixed. Although a center frequency, the carrier, was present in this experiment the physics is similar to the two-field experiments. At this point it is helpful to review the theoretical predictions for the problem.^{4,6,19-22}

THEORETICAL REVIEW

The response of an atomic system can be characterized, in part, by the rate at which it absorbs, or scatters, energy from a resonant laser beam. We employ a calculation developed by Hillman *et al.*⁶ to calculate the rate of absorption from the optical Bloch equations

$$\dot{u} = -u/T_2 - \Delta v, \quad (1a)$$

$$\dot{v} = \Delta u - v/T_2 + \kappa E(t)w, \quad (1b)$$

$$\dot{w} = -(\omega + 1)/T_1 - \kappa E(t)v, \quad (1c)$$

where Δ is the detuning, $1/T_2$ and $1/T_1$ are the transverse and longitudinal decay rates respectively. The dipole coupling constant, κ , is given by

$$\kappa = 2d/\hbar \quad (2)$$

where d is the dipole-moment matrix element and \hbar is Planck's constant. We are interested in the response of the atom to a 100% AM excitation. In this case the electric field amplitude can be written as

$$E(t) = 2E_1 \cos(\delta\omega t), \quad (3)$$

where $\delta\omega$ is the modulation frequency and the amplitude of the electric field is E_1 .

According to Floquet's theorem, the stationary-state response of the atomic variables can be expanded in a Fourier series of the modulation frequency $\delta\omega$. The atomic polarization components and the atomic inversion can be written

$$u(t) = \sum_{n=-\infty}^{\infty} u_n \exp(in\delta\omega t), \quad (4a)$$

$$v(t) = \sum_{n=-\infty}^{\infty} v_n \exp(in\delta\omega t), \quad (4b)$$

and

$$w(t) = \sum_{n=-\infty}^{\infty} w_n \exp(in\delta\omega t). \quad (4c)$$

The n^{th} harmonic components of the in-phase and in-quadrature dipole moments and of the atomic inversion are denoted by u_n , v_n , and w_n , respectively. We substitute Eqs. (4) into the Bloch equations, Eqs. (1), to obtain a set of recurrence relations between the harmonic components of the atomic variables. The ratio of the first harmonic component of the in-quadrature dipole moment to the zeroth harmonic (time-averaged) component of the inversion is expressed as a continued fraction

$$\frac{v_1}{w_0} = \frac{1}{B_1 + \frac{I_1}{B_2 + \frac{I_1}{B_3 + \frac{I_1}{B_4 + \dots}}}}, \quad (5)$$

where the single field intensity is

$$I_1 = (\kappa E_1)^2 T_1 T_2, \quad (6)$$

and the coefficients denoted by B_n are

$$B_n = 1 + in\delta\omega T_2 + \frac{(\Delta T_2)^2}{1 + in\delta\omega T_2}, \quad (7a)$$

for odd n , and

$$B_n = 1 + in\delta\omega T_1, \quad (7b)$$

for even n .

We can solve for the time-averaged component of the atomic inversion, w_0 , in terms of the continued fraction, and then write the excited state population

$$\rho_e = \frac{2I_1 \text{Re}\{v_1/w_0\}}{1 + 2I_1 \text{Re}\{v_1/w_0\}}. \quad (8)$$

We are ultimately interested in the absorption of the AM field. The average rate at which a two-level atom scatters light in the form of resonance fluorescence is proportional to the time-averaged absorption. The fluorescent emission rate is proportional to the excited state population. Consequently, for the case of a 100% AM excitation of a two-level atom, the rate of absorption of energy is proportional to the time-averaged component of the excited state population.

We plot the results of these calculations in Figs. 1 and 2. In Fig. 1 we plot the time-averaged excited-state population for a fixed Rabi frequency as a function of the modulation frequency, $\delta\omega T_2$. This curve is quite complicated and it shows several resonances in the absorption spectrum of the fields. To understand these peaks it is helpful to solve the problem in the absence of damping. In this case one obtains an analytic solution in which the time-averaged response of the population can be written in terms of $J_0(2\kappa E_1/\delta\omega)$. When we numerically pick off the position of each peak from Fig. 1, we find that the peaks occur whenever the factor $J_0(2\kappa E_1/\delta\omega)$ is equal to zero. The outermost peaks correspond to the first zero of J_0 . The next peaks at smaller values of $\delta\omega T_2$ correspond to the second zero of J_0 and are the first subharmonic resonances. In the limit of large arguments, x , the zeros of $J_0(x)$ become equally spaced versus x . It is in this limit that the resonances are best described as subharmonic resonances. In Fig. 2 the time-averaged population of the excited state is plotted versus the time-averaged dimensionless intensity, $2(\kappa E_1)^2 T_1 T_2$, for a fixed modulation frequency of three atomic linewidths. This is the form of our raw data. The resonances appear as enhancements in the absorption embedded in the usual single-field saturation curve. As the intensity is increased from zero we approach the first-order resonance. The second resonance, occurring at a higher intensity, is the first subharmonic resonance. The order of the subharmonic resonances increases as we look to higher dimensionless intensities. These resonances occur only when the modulation-interaction is strong, meaning the Rabi frequency, κE_1 , exceeds the natural linewidth of the transition, and the modulation depth is large, as in the case of 100% AM.

The dynamic behavior of the atomic variables also reflects the subharmonic behavior of the 100% AM interaction. In Figs. 3(a)-3(d), we show the phase plots formed by the in-quadrature atomic polarization and the inversion at each of the first four resonances (on-resonance excitation is used for the phase plots so that only the in-quadrature polarization is driven). Each figure depicts the trajectory followed by the atomic variables for a complete period of the modulation. Fig. 3(a) depicts the period-one behavior which occurs at the first resonance. Fig. 3(b) shows that a second cycle in the trajectory occurs at the second resonance, which is the first sub-harmonic resonance. Figs. 3(c) and 3(d) show the behavior at the third and fourth resonances respectively. We can compare this system to an anharmonic oscillator being driven every n^{th} cycle of its natural frequency. The oscillator can be driven effectively by the fundamental frequency or any subharmonic of the fundamental. This subharmonic driving is effective since the system responds at higher-harmonics of the driving frequency when the driving force is large enough to induce a nonlinearity.

EXPERIMENTAL SETUP

The experimental apparatus we used to study the absorption spectrum is shown in Fig. 4. The absorption is determined by measuring the total fluorescence from a small portion of the interaction region. We imaged the fluorescence from the interaction region onto a pinhole placed in front of a photo-multiplier tube. Spatially filtering the fluorescence signal limits the signal to that from a small region near the center of the laser beam where the intensity is constant to within 10%. This allows us to study atoms with equal Rabi frequencies. The detectors were dc-coupled to measure the time-averaged fluorescence.

Sodium was chosen as the atomic medium because it has a large oscillator strength and is readily made into a two-level atomic system. To obtain a two-level atomic system we resonantly excited the 3s to 3p transition with circularly-polarized light. A two-level system results from the pumping of population into the aligned magnetic sublevels²³. The atomic beam was collimated to provide a divergence angle of 1 milliradian with an

associated Doppler width of less than 2 MHz (this is 20% of the natural linewidth of the sodium transition). The atoms were excited by a circularly-polarized beam whose angular divergence was less than 1 milliradian (this angular spread accounts for no more than 1 MHz Doppler broadening). The laser field was the output of a frequency stabilized rhodamine 6G dye laser, whose full-width-frequency jitter was less than 1 MHz. The angular divergence of the laser and atomic beams together with the frequency jitter of the laser gave us a total systematic broadening of 4 MHz, or 40% of the natural linewidth. This systematic linewidth was verified by measuring the full spectral width of the atomic transition to be 14 MHz (the natural linewidth is 10 MHz).

We produced a 100% AM laser field with a modulation frequency, $\delta\omega/2\pi$, of 15 MHz, which is three times the transverse relaxation rate of the sodium D_2 line. The modulation was produced by passing the laser through a high efficiency acousto-optic modulator (AOM). A portion of the beam was up-shifted by the 30 MHz drive-frequency of the AOM. The diffraction efficiency was adjusted so that the power diffracted into the first-order beam was equal to that left in the zeroth-order undiffracted beam. We, then recombined the two orders to create the bichromatic field. The two beams were aligned with interferometric precision in order that a strong beat note of 30 MHz was clearly detected by a photo-diode measuring the far-field intensity. After recombination, the field state can be described in terms of a carrier, at the mean frequency of the two frequency components, that is 100% amplitude-modulated at one half the drive frequency of the AOM. Since the recombination geometry is different for each modulation frequency it was inconvenient for us to vary the modulation frequency in search of the resonances. Instead, we held the modulation frequency fixed and varied the Rabi frequency by sweeping the intensity of the laser. This was done with a set of linear polarizers and an electro-optic cell driven by our computer.

At each power setting we recorded the incident laser intensity along with the intensity of the fluorescence emitted by the atoms. Each data point was averaged 100 times over several milliseconds to integrate out any fast intensity fluctuations of the laser

field. All data was recorded with a 14 bit analog to digital converter on a PDP-11/23 microprocessor. The 40 db dynamic range provided by the digitization is necessary to match the dynamic range of our data.

EXPERIMENTAL RESULTS

We collected data for the AM field on-resonance and for a detuning of three linewidths. The modulation frequency was equal to three atomic linewidths for all the data we present in this paper ($\delta\omega T_2 = 3$). In Fig. 5 we plot the fluorescent intensity versus incident time-averaged intensity for on-resonance excitation. The resonances appear as bumps on the saturated absorption curve. The solid curve shows a theoretical fit to our data. A two-level theory is averaged over detuning and modulation frequency to model the very slight imperfect recombination of the two beams. When the two laser beams exiting the AOM are not perfectly aligned (see Fig. 4), the atoms see a moving interference pattern. If this pattern moves along the atomic-beam axis, the spread in atomic velocities causes the atoms to experience a spread in modulation frequencies.

Since we are mainly interested in the resonances, we can divide our data by a single-frequency absorption curve to obtain a normalized atomic response to the two-field excitation. This normalization flattens out the curve so that the resonances may be seen on a single expanded graph. In Fig. 6 we plot the normalized fluorescent intensity versus the parameter $\sqrt{2}\kappa E_1 T_2$. The parameter $\sqrt{2}\kappa E_1$ is the root-mean-square (rms) Rabi frequency. A distinct enhancement in the absorption of the fields occurs when the rms Rabi frequency is equal to $n(2\delta\omega)$, where n is the number of the resonance and $2\delta\omega$ is the frequency difference between the two field modes. We can observe the first order resonance and the first two subharmonic resonances with resonant excitation. With the fields detuned by three natural linewidths we have observed up to three subharmonic resonances. In Fig. 7 we have plotted the fluorescent intensity versus the rms Rabi frequency for resonant and detuned excitation (for the detuned case $\Delta T_2 = 3$). The resonances occur at lower intensities when the modulated field is detuned since the generalized Rabi frequency is larger for the same amount of incident laser power. We do not have an analytical

expression for the position of the resonance peaks. However, we find that the empirical formula

$$\left\{ (\sqrt{2} \kappa E_1)^2 + \Delta^2 \right\}^{1/2} = n (2\delta\omega), \quad (9)$$

describes the position of the resonances quite well for both detuned and resonant excitation. We can interpret the quantity on the left as the generalized Rabi frequency. A resonance occurs whenever the generalized Rabi frequency is equal to an integer, n , times the frequency separation, $2\delta\omega$, between the two fields. This formula for the resonances agrees with weak modulation experiments^{11,13}.

It is instructive to look at the positions of the resonances for the detuned and resonant modulated excitations. We used the computer to determine the position of the resonance peaks for the normalized data. The positions of these peaks for detuned and resonant excitation are plotted on the same graph in Fig. 8. The position of the n^{th} resonance for the detuned case appears at a lower intensity than the corresponding resonance for the case of zero detuning. The solid lines represent the theoretical predictions for the positions of the resonances according to Eq. (9).

CONCLUSIONS

We have presented both theory and experiment for the absorption of a 100% AM field by a closed two-level atomic system. The interaction reveals resonances at subharmonics of the Rabi frequency. We observed the first three resonances with resonant excitation, and we observed the first four resonances with detuned excitation. For resonant excitation, the absorption of the AM field is enhanced whenever the ratio $2\kappa E_1/\delta\omega$ is equal to a zero of the zeroth order Bessel function. In this paper we have presented an empirical relation for the occurrence of the resonances for both resonant and detuned excitation. The data agrees with this empirical prediction.

Our data shows the absorption of the bichromatic field is enhanced at the first-order resonance and at each of the subharmonic resonances. This result differs from that obtained by Thomann.¹⁸ The results of that experiment showed a decrease in the absorption at each resonance. In that experiment the field modulation index was no larger

than 0.65 so there was always a significant field component at the carrier frequency. When the carrier frequency is present it can beat with each of the modulation sidebands to produce overtones, at harmonics of the modulation frequency, in the atomic response. This beat frequency is one half the beat frequency arising between the two modulation sidebands. The harmonic overtones of these two sets of beat notes can destructively interfere in a three field experiment. This interference causes the absorption to diminish at each resonance.

We have demonstrated the complicated behavior of a purely bichromatic field interacting with a closed two-level atomic system. Subharmonic resonances occur due to the coherent nonlinear interaction of a multi-frequency field with an isolated atomic resonance. It is exactly this type of nonlinear interaction that determines the competition or cooperation between cavity modes in a laser gain medium. The same set of subharmonic resonances occur in a saturated two-level amplifier interacting with a modulated laser field. This provides a mechanism for multimode instabilities in a homogeneously broadened laser. Instabilities of this type have been observed.⁵

ACKNOWLEDGEMENTS

The authors wish to thank Lloyd W. Hillman for many useful conversations. We would like to acknowledge the Army Research Office for support of this research.

References

1. H. Risken and K. Nummedal, J. Appl. Phys. **39**, 4662-4672, (1968).
2. H. Risken and K. Nummedal, Phys. Lett. **26A**, 275-276, (1968).
3. B.J. Feldman and M.S. Feld, Phys. Rev. A **1**, 1375-1396, (1970).
4. N. Tsukada and T. Nakayama, Phys. Rev. A **25**, 964-977, (1982).
5. L. W. Hillman, J. Krasinski, R.W. Boyd, and C.R. Stroud, Jr., Phys. Rev. Lett. **52**, 1605-1608, (1984).
6. L.W. Hillman, J. Krasinski, K. Koch, and C.R. Stroud, Jr., J. Opt. Soc. Am. B. **2**, 211-217, (1985).
7. T. Ogawa and E. Hanamura, Appl. Phys. B **43**, 139-153, (1987).
8. B. R. Mollow, Phys. Rev. A **5**, 2217-2222, (1972).
9. R. Saxena and G. S. Agarwal, J. Phys. B: Atom. Molec. Phys. **12**, 1939-1951, (1979).
10. R. W. Boyd, M. G. Raymer, P. Narum, and D. J. Harter, Phys. Rev. A **24**, 411-423, (1981).
11. F. Y. Wu, S. Ezekiel, M. Ducloy, and B. R. Mollow, Phys. Rev. Lett. **38**, 1077-1080, (1977).
12. D. J. Harter, P. Narum, M. G. Raymer, and R. W. Boyd, Phys. Rev. Lett. **46**, 1192-1195, (1981).
13. M.T. Gruneisen, K. R. MacDonald, and R. W. Boyd, J. Opt. Soc. Am. B **5**, 123-129, (1988).
14. M. Sargent III, P.E. Toschek, H.G. Danielmeyer, Appl. Phys. **11**, 55-62, (1976).

15. L.W. Hillman, R.W. Boyd, and C.R. Stroud, Jr., Opt. Lett. 7, 426-428, (1982).
16. M. A. Kramer, R.W. Boyd, L. W. Hillman, and C. R. Stroud, Jr., J. Opt. Soc. Am. B 2, 1444-1455,(1985).
17. A. M. Bonch-Bruevich, T.A. Vartanyan, and N. A. Chigir, Sov. Phys. JETP 50, 901-906, (1979).
18. P. Thomann, J. Phys. B: Atom. Molec. Phys. 13, 1111-1124, (1980).
19. P. Thomann, J. Phys. B: Atom. Molec. Phys. 9, 2411-2419, (1976).
20. G.I. Toptygina and E.E. Fradkin, Sov. Phys. JETP 55, 246-251, (1982).
21. An. A. Mak, S. G. Przhibel'skii, and N. A. Chigir, Seriya Fizicheskaya 47, 1976-1983, (1983).
22. G. S. Agarwal and N. Nayak, J. Opt. Soc. Am. B 1, 164-168, (1984).
23. J. A. Abate, Opt. Commun. 10, 269-272, (1974).

Figure Captions

- Fig. 1** The time-averaged excited state population as a function of modulation frequency, $\delta\omega T_2$. The Rabi frequency is held fixed, $\kappa E_1 T_2 = 10$, while the modulation frequency, $\delta\omega T_2$, is varied to observe the subharmonic resonances. The detuning is zero, $\Delta T_2 = 0$.
- Fig. 2** The time-averaged excited-state population as a function of intensity. The modulation frequency is held fixed, $\delta\omega T_2 = 3$, while the time-averaged dimensionless intensity, $2(\kappa E_1)^2 T_1 T_2$, is varied to observe the resonances. The detuning is zero, $\Delta T_2 = 0$.
- Fig. 3** The trajectories of the atomic inversion and the in-quadrature polarization. We plot the atomic inversion versus the atomic polarization at the first four resonances. The modulation frequency for each of the figures is $\delta\omega T_2 = 3$. In Fig. 3(a) the Rabi frequency corresponds to the first resonance. The next three figures show the behavior at the first three subharmonic resonances (b) $n = 2$, (c) $n = 3$, and (d) $n = 4$. The detuning is zero, $\Delta T_2 = 0$.
- Fig. 4** The experimental apparatus. The diagram is labeled with the following notation: SDL - stabilized dye laser; AOM - acousto-optic modulator; M - mirrors; BS - beam splitter; LP - linear polarizer; EOM - eletro-optic modulator; $\lambda/4$ - quarter-wave plate; Na - sodium oven; AB - atomic beam; PH - pin-hole; PMT - photo-multiplier tube; PD - photo-diode; PDP-11/23- micro-computer.

- Fig. 5 The time-averaged fluorescent intensity versus time-averaged incident intensity. The raw data is plotted with dots and the solid curve represents a best theoretical fit. The modulation frequency is fixed, $\delta\omega T_2 = 3$, and the detuning is zero, $\Delta T_2 = 0$.
- Fig. 6 The normalized time-averaged fluorescent intensity versus rms Rabi frequency for resonant excitation. The fluorescence data from Fig. 5 was normalized by a single field saturation curve to flatten out the resonant peaks. The Rabi resonance and the first two subharmonic resonances are shown.
- Fig. 7 Normalized time-averaged fluorescent intensity versus rms Rabi frequency for resonant and detuned excitation. The dotted curve represents the data for the resonant case, $\Delta T_2 = 0$. The dashed line represents data for the detuned case, $\Delta T_2 = 3$. The resonant peaks occur at lower Rabi frequencies for the detuned case. The modulation frequency is $\delta\omega T_2 = 3$.
- Fig. 8 The position of the subharmonic resonances versus resonance number for resonant and detuned excitation. The rms Rabi frequency, $\sqrt{2}\kappa E_1 T_2$, corresponding to the n^{th} resonance is plotted versus n . The circles represent the data for resonant excitation, $\Delta T_2 = 0$. The squares represent the data for detuned excitation, $\Delta T_2 = 3$. The solid line represents the empirical expression in Eq. (9) for resonant excitation $\Delta T_2 = 0$. The dashed line represents Eq. (9) for $\Delta T_2 = \delta\omega$. The modulation frequency is $\delta\omega T_2 = 3$.

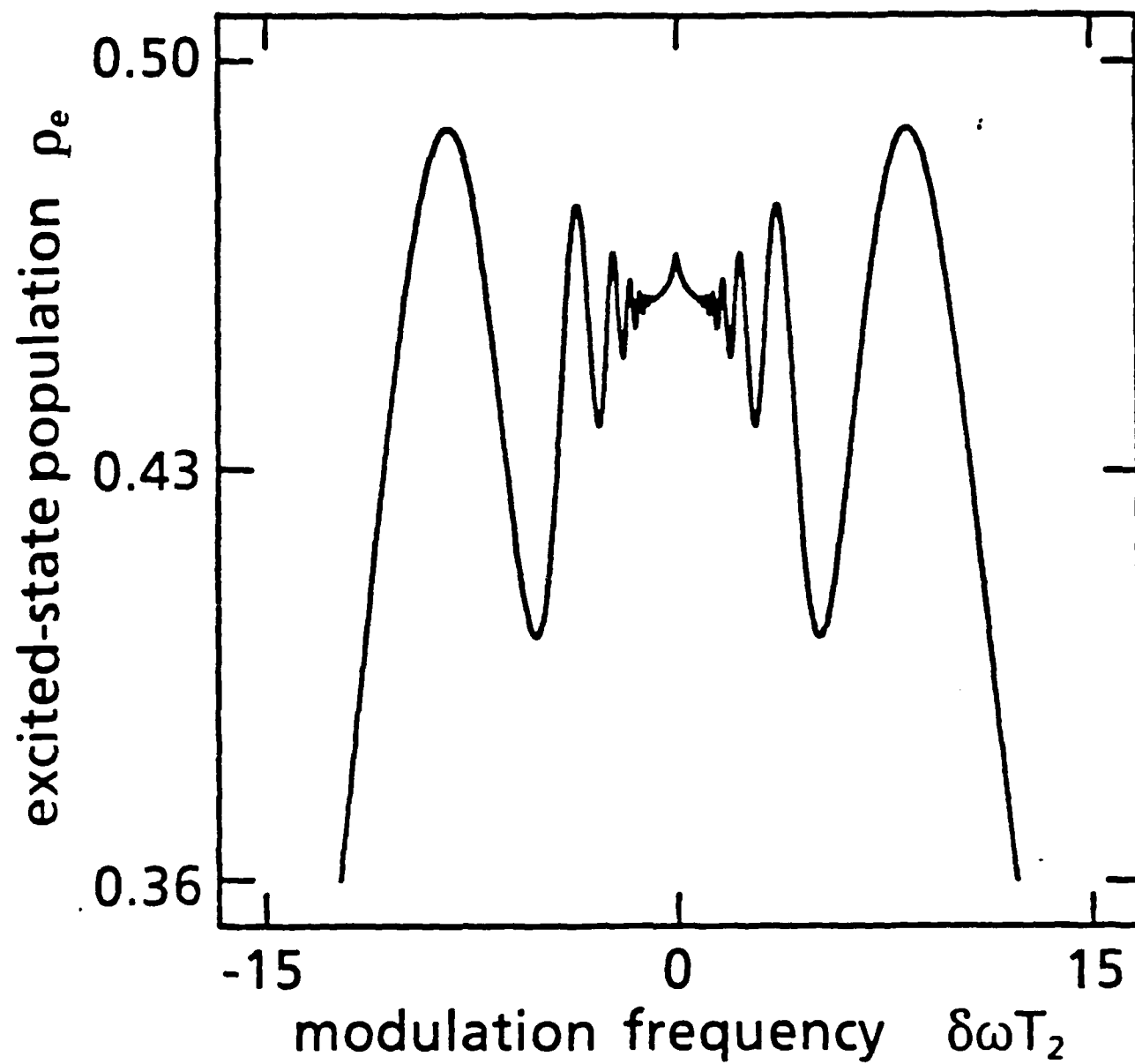


Fig. 1

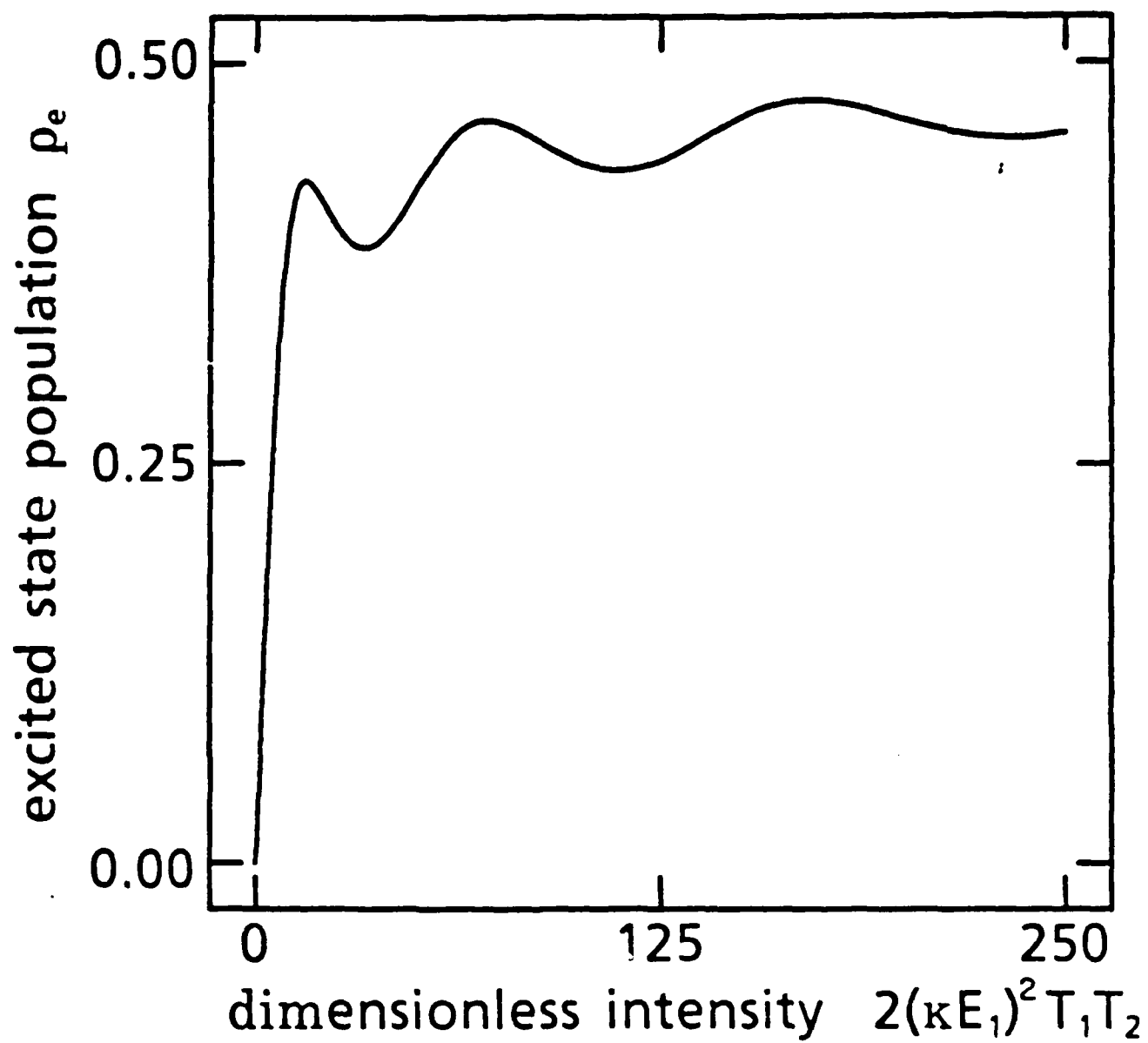


Fig 2

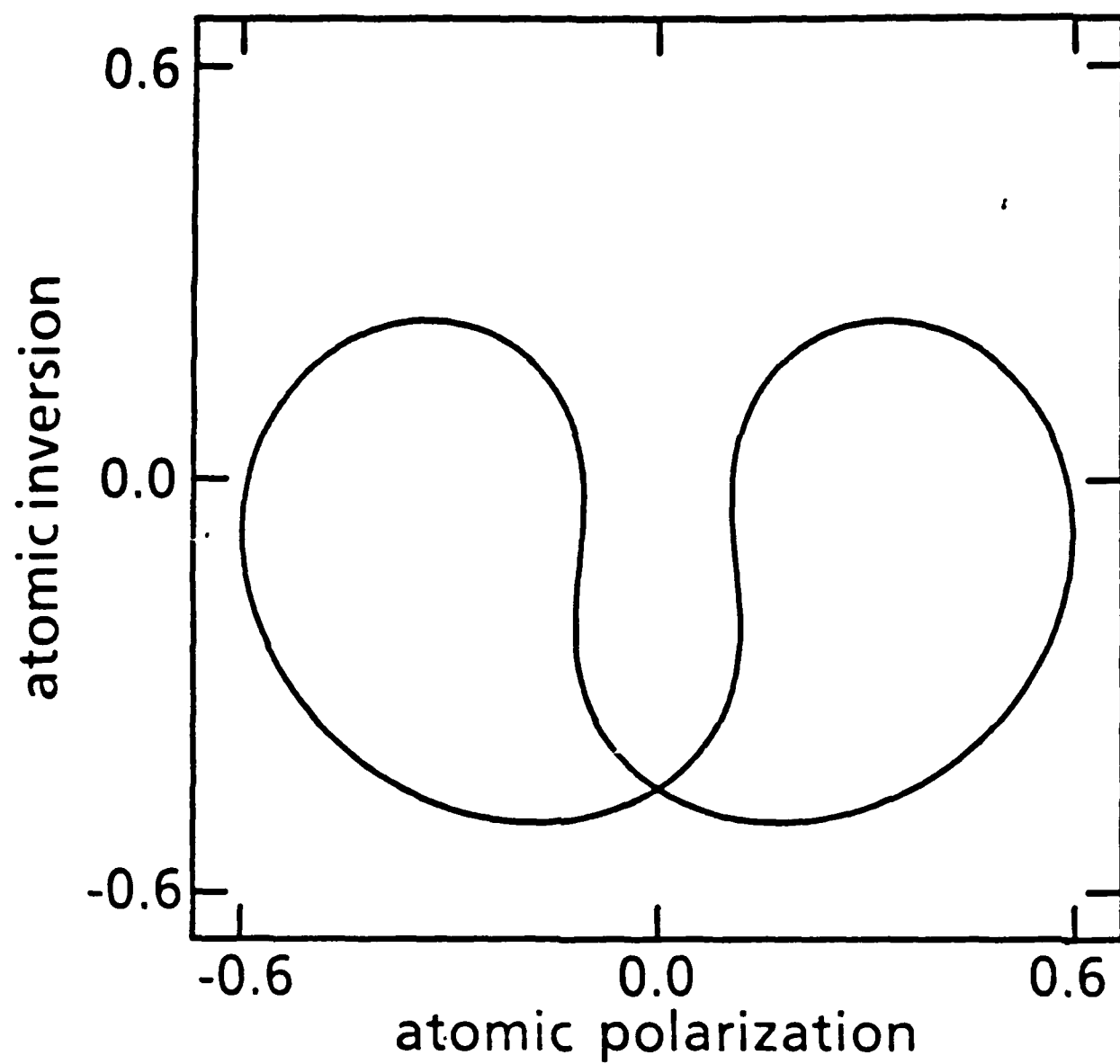


Fig 3a

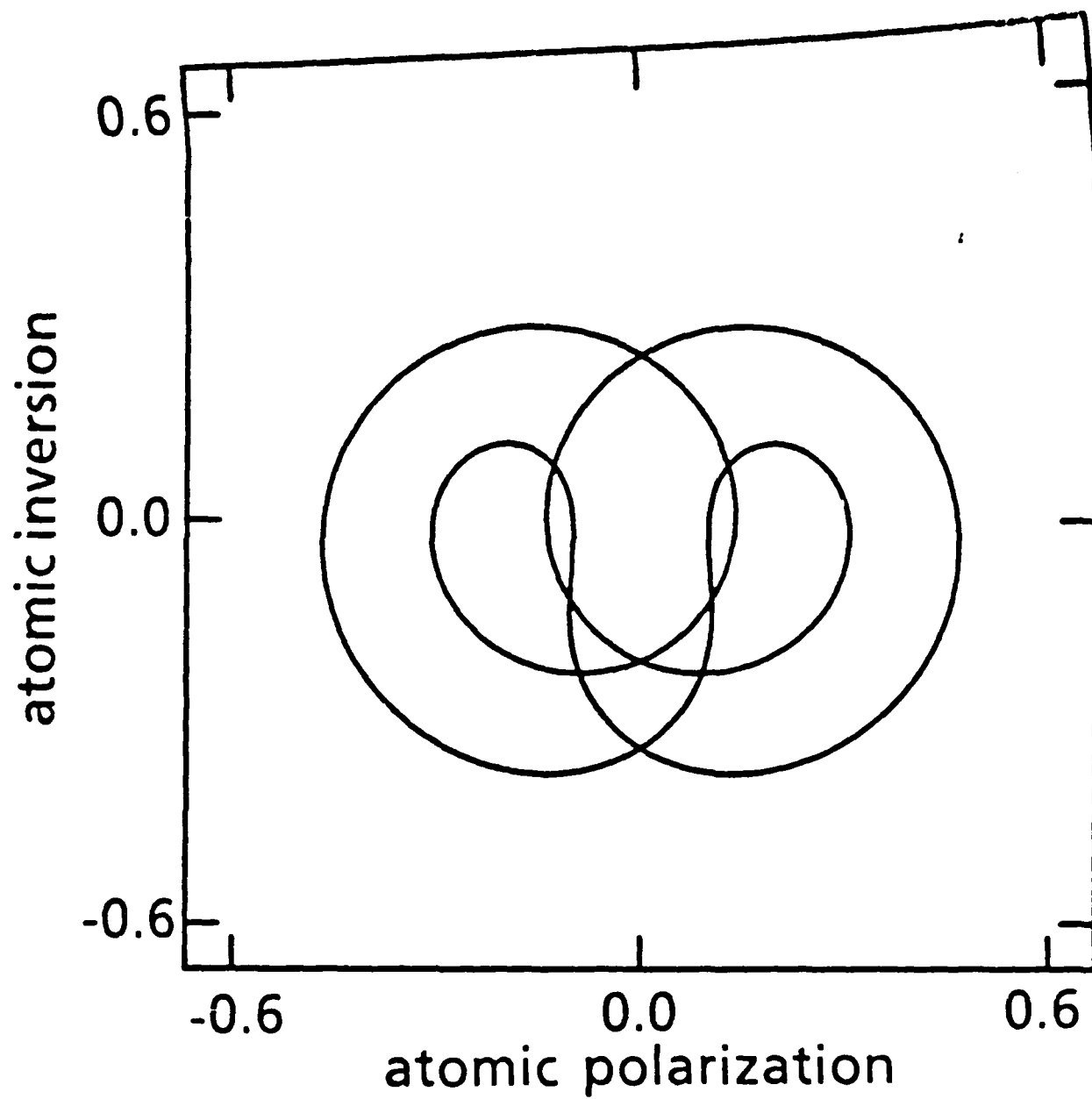


Fig 3b

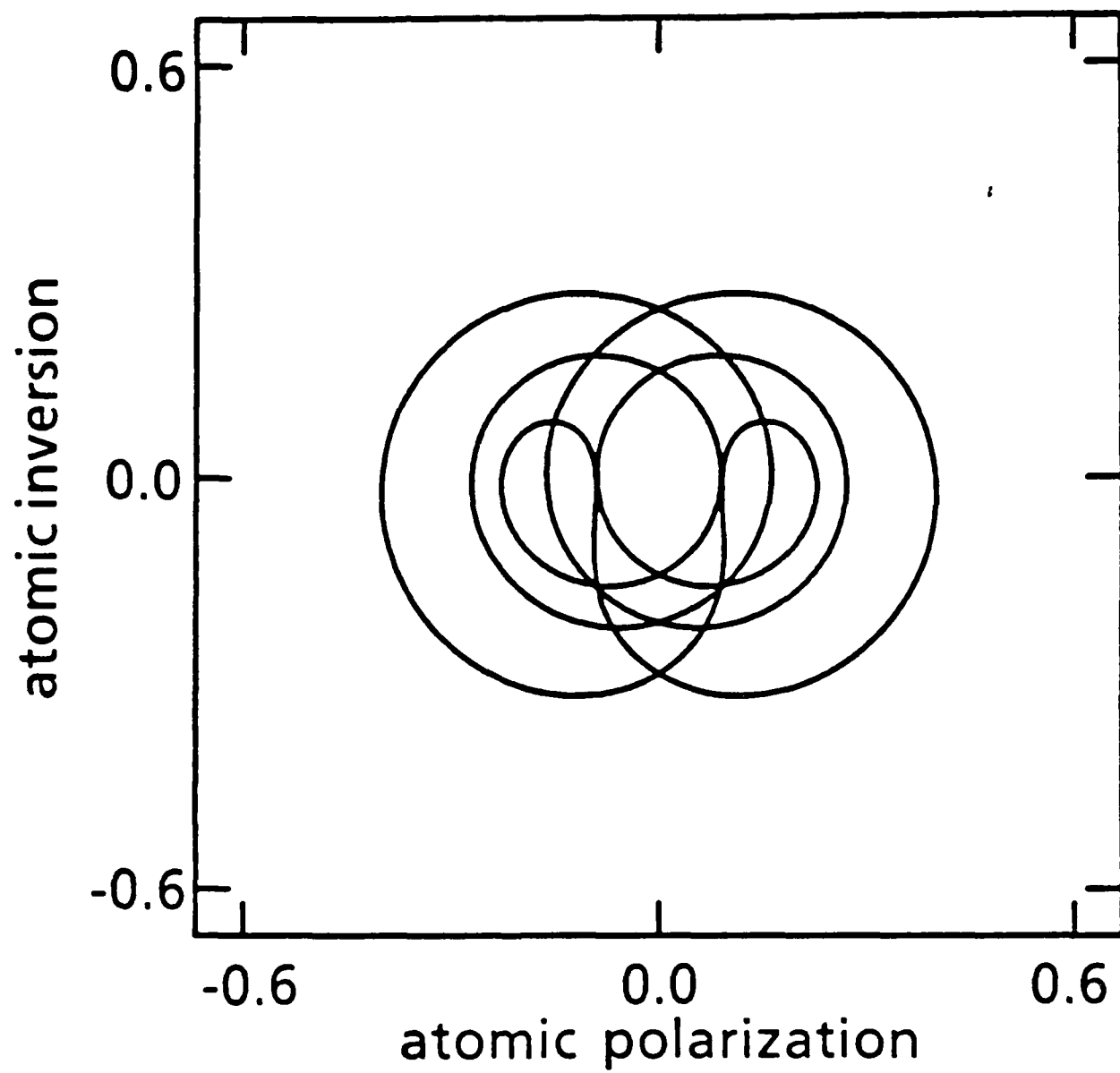


Fig 3c

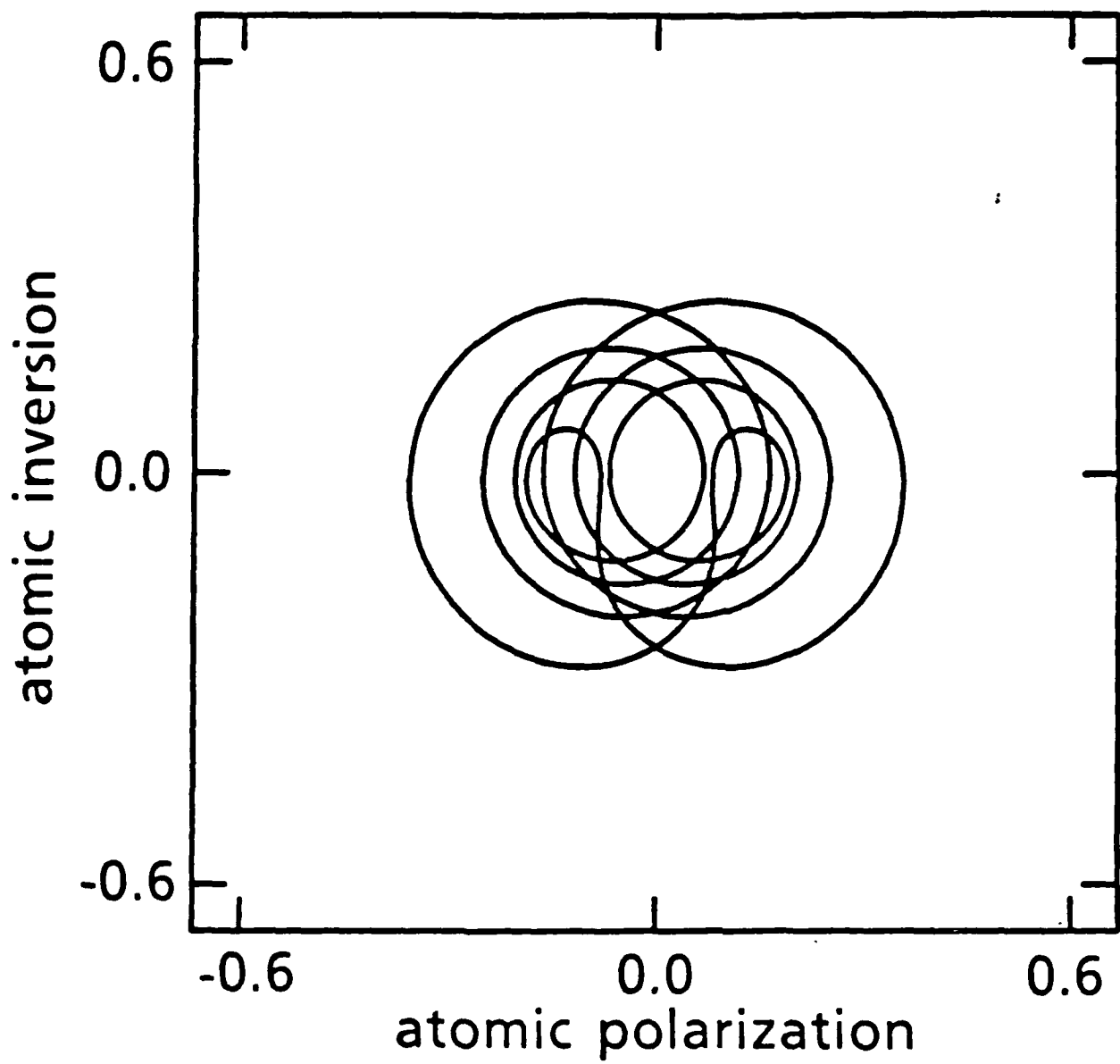


Fig 3d

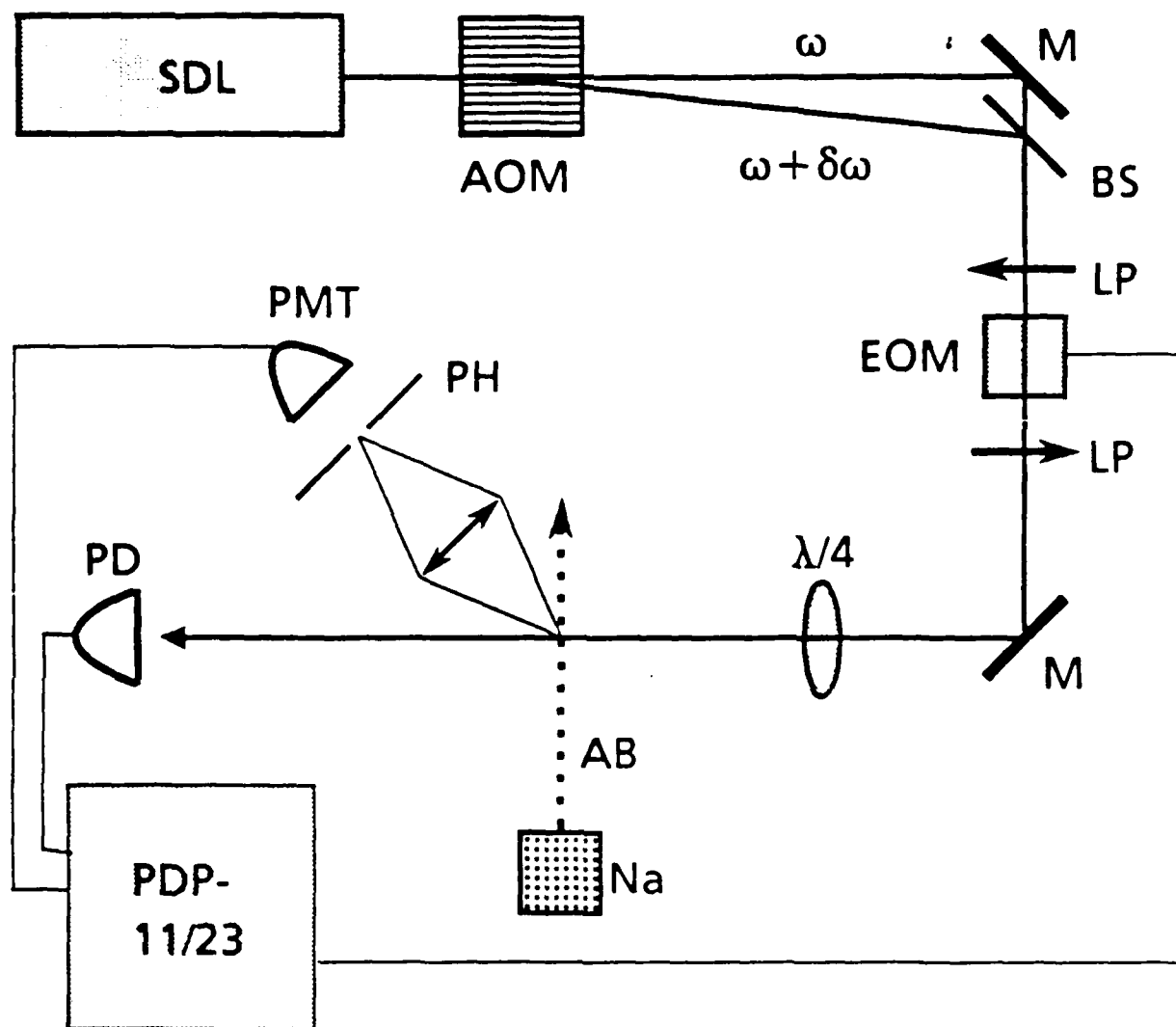


Fig 4

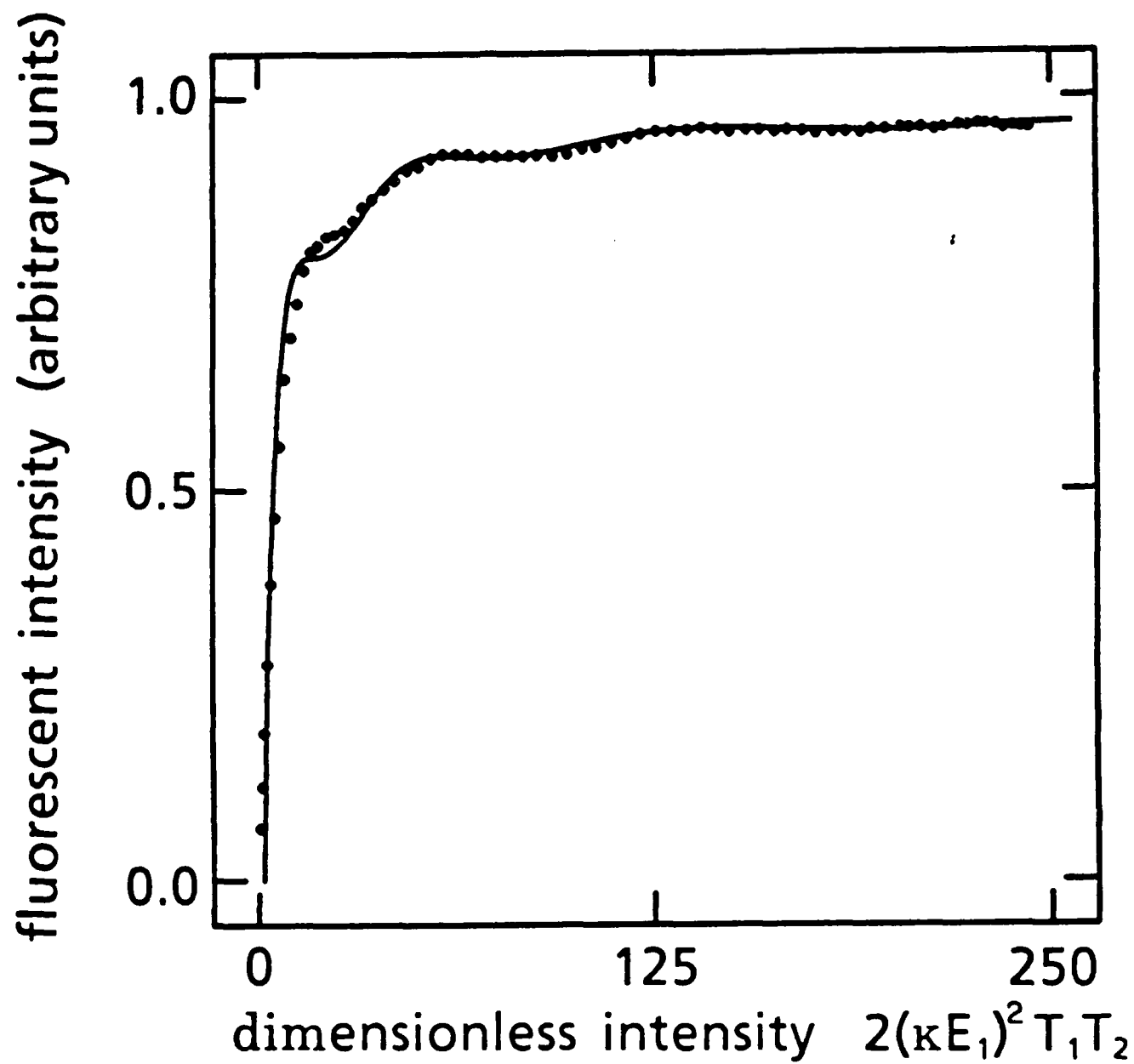


Fig 5

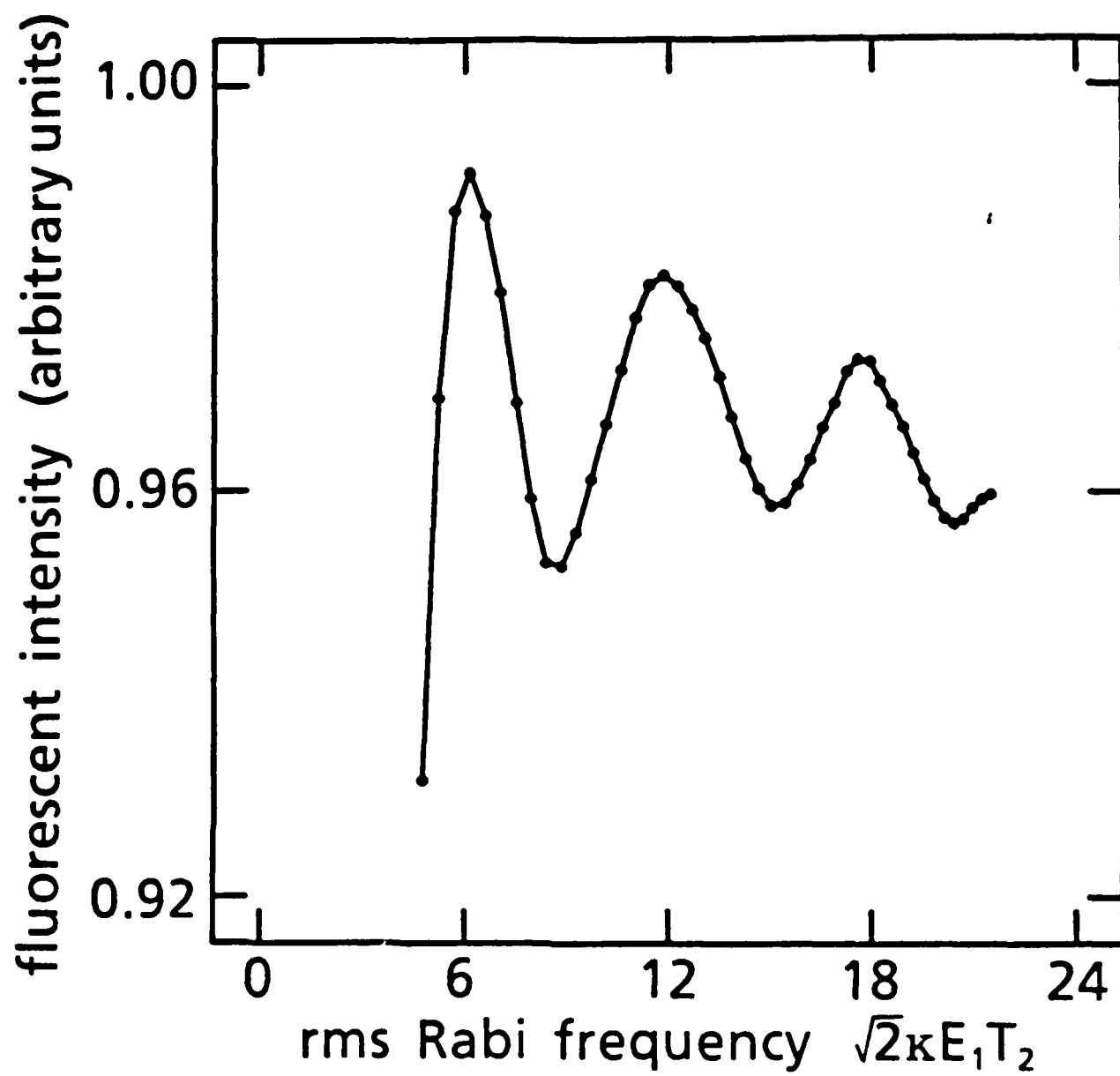


Fig 6

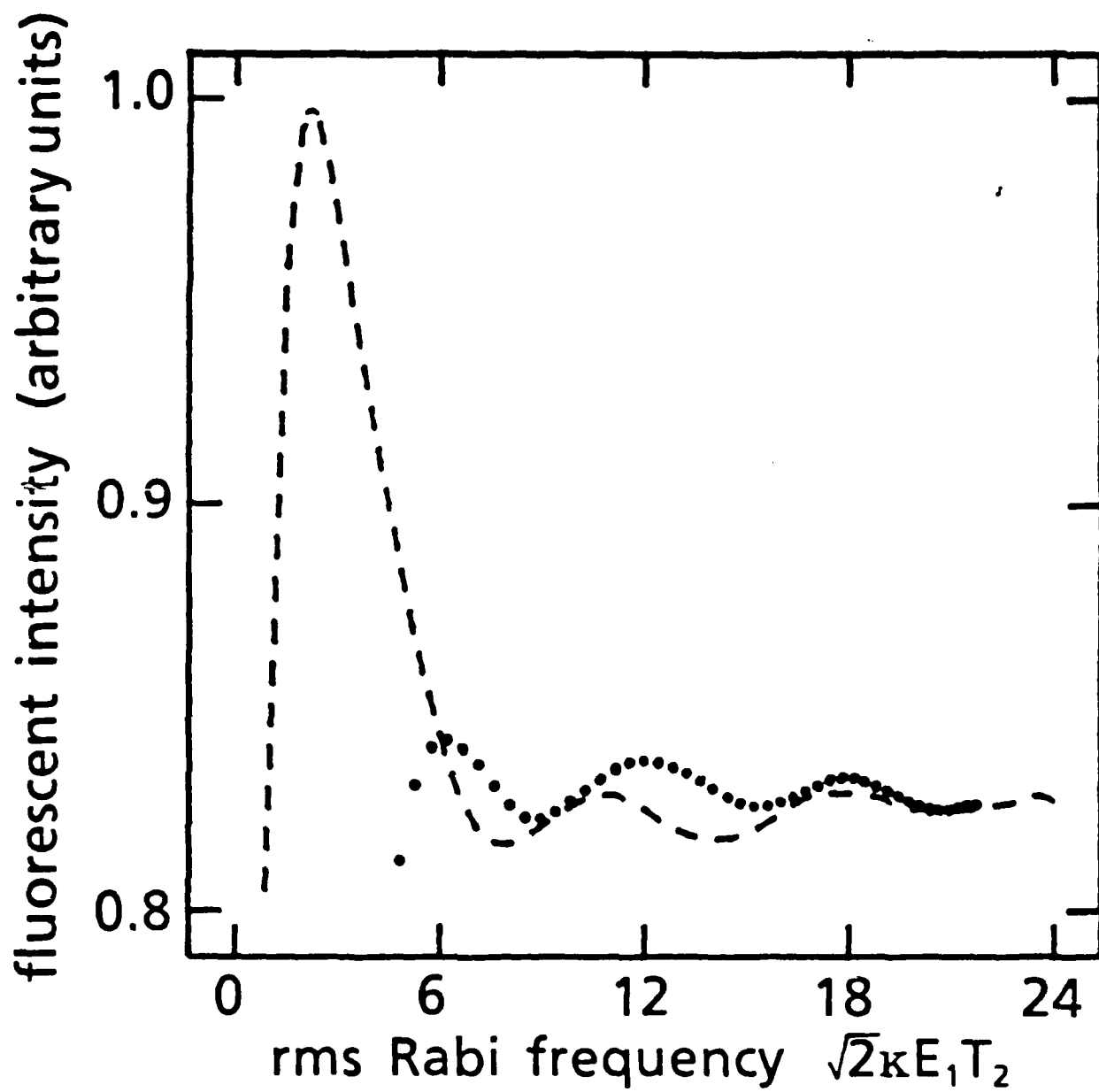


Fig 7

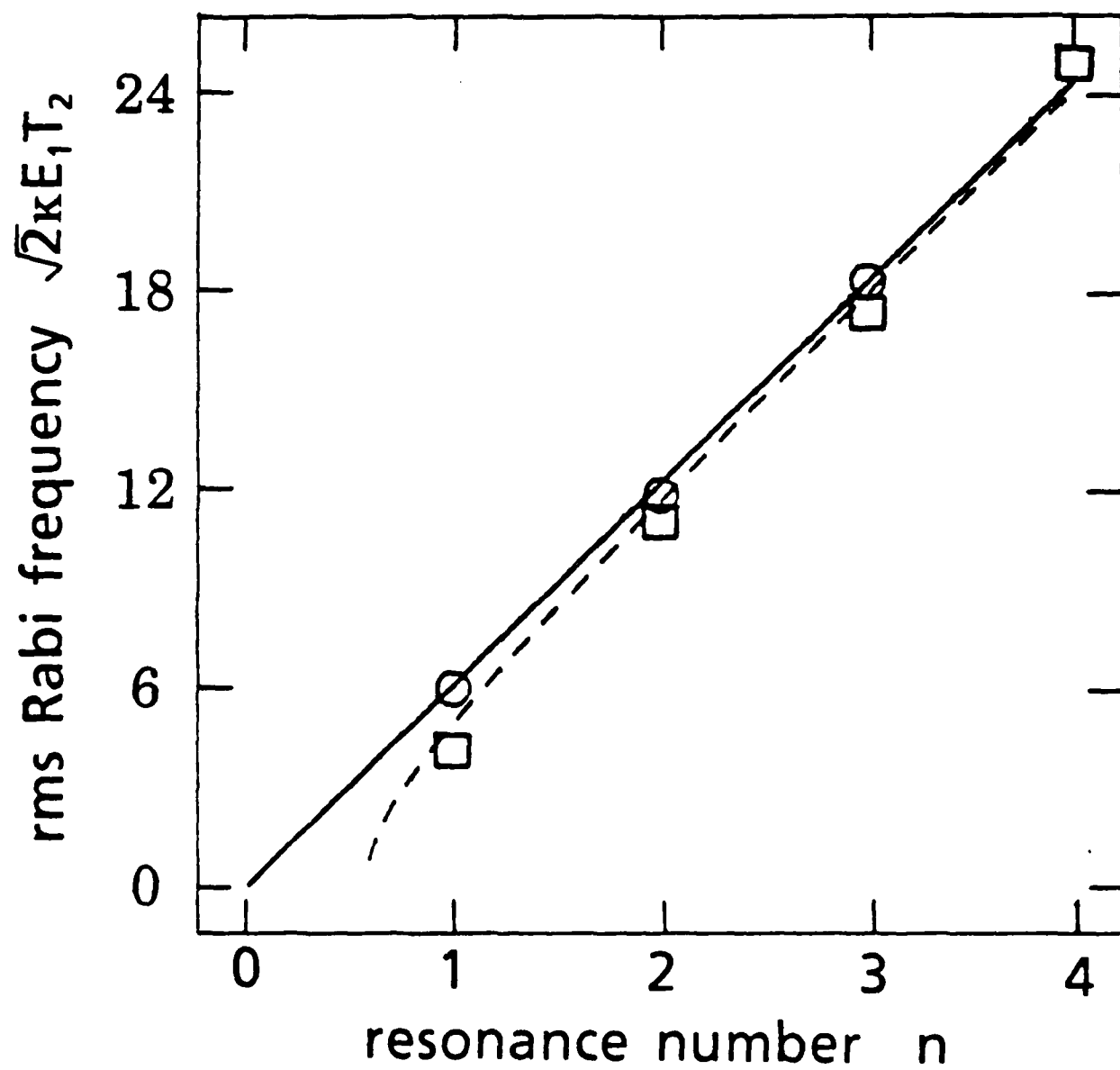


Fig 8

Subharmonic instabilities in resonant interactions with bichromatic fields

Karl Koch, Brian J. Oliver, Stephen H. Chakmakjian, C. R. Stroud, Jr.

**The Institute of Optics
University of Rochester
Rochester, NY 14627**

and

**Lloyd W. Hillman
School of Electrical Engineering
Cornell University
Ithaca, NY 14853**

Abstract

We consider the interaction of two 100% amplitude-modulated fields with a two-level system. The analysis includes a discussion of the stability of an amplitude-modulated laser field to the growth of subharmonic amplitude-modulated fields.

1. Introduction

Recently, a great deal of interest has focused on instabilities in laser systems¹⁻². Motivation of this interest is provided by a desire to understand the complicated dynamics of nonlinear systems. Optical systems provide a convenient ground for rigorously examining these dynamics. The laser is a specific example of a rigorously describable optical system containing the nonlinear interaction of light with matter. Subharmonic instabilities have been observed in a number of different lasers³⁻⁵. Subharmonic instabilities have become especially interesting, since a sequence of period doublings has been identified as a possible route to chaos.

Instabilities in lasers have existed since the first demonstration of a laser by Maiman⁶. Lasers have operated in a number of states since that first demonstration. The complications introduced by pump fluctuations, spatial hole burning, inhomogeneous broadening, etc., have enhanced this variety of available states. The continuous-wave ring dye laser is a homogeneously broadened laser that contains few of these additional complications, yet still displays a rich variety of operational states. Hillman *et al.*⁵ observed a continuous-wave dye laser, initially operating at a single frequency, go unstable and begin oscillating at two frequencies. As the pump power was increased, the two components of the laser spectrum separated with a linear dependence on the electric field strength of the laser. When the separation of the spectral components reached $\sim 80\text{\AA}$, the laser encountered another instability threshold. The two-frequency state then collapsed to another two-frequency state of smaller frequency separation. On increasing the pump power still further, this new two-frequency state behaved similarly to the initial two-frequency state.

The physical mechanism, for these new states of dye laser operation, is not well understood. There have been a number of theoretical treatments of a multimode laser⁷⁻¹¹. Unfortunately, none of them has provided an explanation for all the features of the experimental results. The most successful theoretical model⁹⁻¹¹ takes

the molecular structure of the laser-dye molecule into account. However, the actual physical mechanism responsible for the instability remains to be seen.

In an attempt to develop physical intuition for the problem of a nonlinear system being driven by a two-component field, we previously examined the gain for such a field driving a two-level atom⁸. These calculations showed that the gain of the two-component field displays resonances when the frequency separation of the two fields is equal to the Rabi frequency or a subharmonic of the Rabi frequency.

In this paper we consider the stability of a bichromatic laser field. Since a general self-consistent solution to the multimode laser equations is not available, the stability analysis must be carried out in some other manner. The equations could be numerically integrated; however, the parameter space is too large for such a solution to provide intuition. An alternative is to calculate the atomic response to the laser field and examine the gain experienced by a probe field. When the probe-field gain exceeds the laser-field gain, an instability will occur. In this paper we will discuss the stability of a bichromatic field to the growth of a bichromatic probe field using just such an alternative.

The analytic description of the interaction of four field components with a resonant medium is a very cumbersome task. The nonlinear response of the medium produces combination tones of the field components in the polarization of the medium. When the frequencies of the combination tones are incommensurate with one another, the medium can exhibit a broadband spectral response¹². The analytic description of such a problem becomes extremely difficult. However, if the frequencies of the combination tones are commensurate, one can employ Floquet's theorem¹³ to analytically study the problem. Neglecting dispersion in the cavity, the mode frequencies are all commensurate with one another. The mode frequencies are integer multiples of the inverse of the cavity round-trip time. Therefore, the simplest physical situation is one in which the field frequencies are commensurate

with each other. The most elementary four-component field is one in which each field component creates a degenerate beat frequency with the nearest other field component. We will examine such a field and further specify the problem by considering only subharmonic probe fields. These probe fields are especially interesting as they give us insight into possible physical mechanisms for subharmonic instabilities. This same analysis could be carried out for other subharmonic fields, such as the $\frac{1}{2}$ -subharmonic observed in period doubling sequences. The techniques used in the analysis of such a field would be identical, however the dimension of the matrices used in the solution would be larger. The stability of bichromatic fields to harmonic bichromatic probe fields will be the subject of a future paper¹⁴. For simplicity, the fields are symmetrically placed about the atomic resonance frequency; the extension of the problem to include asymmetric field states is straight forward. Figure 1 shows the spectrum of this symmetric field.

2. Outline of the calculation

The general expression for a four-component field is better understood by first analyzing the single 100% amplitude-modulated (AM) field. The expression for such a field is written as a two component field or a single component with a sinusoidal amplitude.

$$E_1(t) = 2 \xi (\cos(\omega + \delta\omega)t + \cos(\omega - \delta\omega)t) \quad (1a)$$

$$= 4 \xi \cos\delta\omega t \cos\omega t. \quad (1b)$$

The amplitude of each frequency component is equal to 2ξ .

The use of complex phasor diagrams to describe the phase relationships between many-component fields can be very helpful. The complex phasor for a 100% AM field is a vector that oscillates along a line through the origin. The amplitude of the field determines the length of the vector; the modulation frequency determines the vector's rate of oscillation. In defining the field above, we chose an arbitrary phase factor so the complex phasor lies along the real axis of the complex plane.

There are two independent subharmonic probe fields at each modulation frequency. When the field is symmetric about the atomic resonance, as in our case, the independent probe fields are in-phase or in-quadrature to the strong field; these phasors will be along the real or imaginary axes respectively. The expression for the 100% AM perturbative fields will be similar to the expression above; however, in general there will be a phase difference between the oscillations of the perturbative fields and the strong field. With these considerations in mind, we choose the perturbation to the 100% AM field for our calculations to be of the form

$$\delta E(t) = 4 \delta \xi' \cos(\frac{1}{3}\delta\omega t + \theta') \cos\omega t - 4 \delta \xi'' \sin(\frac{1}{3}\delta\omega t + \theta'') \sin\omega t. \quad (2)$$

In Eq. (2), the amplitude of the in-phase (in-quadrature) probe field is $\delta \xi'$ ($\delta \xi''$). The phase between the oscillations of the strong field and the in-phase (in-quadrature) subharmonic probe field is θ' (θ''). The total field is the sum of Eq. (1) and Eq. (2).

The optical Bloch equations model the response of a two-level atom coherently driven by an optical field¹⁵. In a reference frame rotating at the frequency, ω , the optical Bloch equations are

$$\dot{u} = -\Omega''(t) w - u/T_2, \quad (3a)$$

$$\dot{v} = \Omega'(t) w - v/T_2, \quad (3b)$$

$$\dot{w} = \Omega''(t) u - \Omega'(t) v - (w - w_{eq})/T_1, \quad (3c)$$

in which

$$\Omega'(t) = 2\kappa [\delta \xi' \cos(\frac{1}{3}\delta\omega t + \theta') + \xi \cos\delta\omega t], \quad (4a)$$

$$\Omega''(t) = 2\kappa \delta \xi'' \sin(\frac{1}{3}\delta\omega t + \theta''), \quad (4b)$$

and $\kappa = 2d/\hbar$. The dipole-moment matrix element between the two levels is d and \hbar is Planck's constant. The slowly varying amplitudes of the in-phase (in-quadrature) part of the dipole moment is u (v). The inversion of the two-level system is w ; w_{eq} is the value the inversion decays to in the absence of a coherent field. The relaxation

times of the inversion and polarization are T_1 and T_2 , respectively. The field components that are in-phase (in-quadrature) to the rotating frame are $\Omega'(t)$ ($\Omega''(t)$).

Floquet's theorem tells us, in the stationary state the atomic variables will respond at harmonics of the driving field modulation frequency. So, in the stationary state we express the atomic variables as Fourier series in the modulation frequency.

$$u = \sum_{n=-\infty}^{\infty} u_n \exp(\frac{1}{3}in\delta\omega t) , \quad v = \sum_{n=-\infty}^{\infty} v_n \exp(\frac{1}{3}in\delta\omega t) , \quad w = \sum_{n=-\infty}^{\infty} w_n \exp(\frac{1}{3}in\delta\omega t) \quad (5)$$

This assumption leads to the following recurrence relations

$$(1 + \frac{1}{3}in\delta\omega T_2) u_n = (\delta\Omega'' w_{n-1} + \delta\Omega''^* w_{n+1}) T_2 , \quad (6a)$$

$$(1 + \frac{1}{3}in\delta\omega T_2) v_n = (\delta\Omega' w_{n-1} + \delta\Omega'^* w_{n+1} + \Omega' w_{n-3} + \Omega' w_{n+3}) T_2 , \quad (6b)$$

$$(1 + \frac{1}{3}in\delta\omega T_1) w_n = w_{eq} \delta_{n,0} - (\delta\Omega'' u_{n-1} + \delta\Omega''^* u_{n+1} + \delta\Omega' v_{n-1} + \delta\Omega'^* v_{n+1} + \Omega' v_{n-3} + \Omega' v_{n+3}) T_1 , \quad (6c)$$

in which

$$\Omega' = \kappa \xi , \quad (7a)$$

$$\delta\Omega' = \kappa \delta \xi' \exp(i\theta') , \quad (7b)$$

$$\delta\Omega'' = i\kappa \delta \xi'' \exp(i\theta'') , \quad (7c)$$

and the asterisk denotes a complex conjugate. The Kronecker delta function is $\delta_{n,0}$.

We solve for u and v in the first two recurrence relations and eliminate them from the third relation. The third relation then becomes a function of the Fourier components of w alone.

$$a_n w_{n-6} + b_n w_{n-4} + c_n w_{n-2} + d_n w_n + e_n w_{n+2} + f_n w_{n+4} + g_n w_{n+6} = w_{eq} \delta_{n,0} \quad (8)$$

in which

$$a_n = L_{n-3} \Omega'^2 T_1 T_2 , \quad (9a)$$

$$b_n = (L_{n-1} + L_{n-3}) \Omega' \delta\Omega' T_1 T_2 , \quad (9b)$$

$$c_n = (L_{n-1} (\delta\Omega''^2 + \delta\Omega'^2) + (L_{n+1} + L_{n-3}) \Omega' \delta\Omega'^*) T_1 T_2 , \quad (9c)$$

$$d_n = (1 + \frac{1}{3} \sin \delta \omega T_1 + (L_{n+1} + L_{n-1}) (|\delta \Omega''|^2 + |\delta \Omega'|^2) T_1 T_2 + (L_{n+3} + L_{n-3}) \Omega'^2 T_1 T_2), \quad (9d)$$

$$e_n = (L_{n+1} (\delta \Omega''^{*2} + \delta \Omega'^{*2}) + (L_{n-1} + L_{n+3}) \Omega' \delta \Omega') T_1 T_2, \quad (9e)$$

$$f_n = (L_{n+1} + L_{n+3}) \Omega' \delta \Omega'^* T_1 T_2, \quad (9f)$$

$$g_n = L_{n+3} \Omega'^2 T_1 T_2, \quad (9g)$$

and

$$L_n = (1 + \frac{1}{3} \sin \delta \omega T_2)^{-1}. \quad (9h)$$

This recurrence relation, Eq. (8), can be rewritten as a three-term recurrence relation; the terms are products of matrixes and vectors.

$$P_n W_{n-2} + Q_n W_n + R_n W_{n+2} = D_n \quad (10)$$

in which

$$P_n = \begin{bmatrix} a_{3n-2} & b_{3n-2} & c_{3n-2} \\ 0 & a_{3n} & b_{3n} \\ 0 & 0 & a_{3n+2} \end{bmatrix}, \quad Q_n = \begin{bmatrix} d_{3n-2} & e_{3n-2} & f_{3n-2} \\ c_{3n} & d_{3n} & e_{3n} \\ b_{3n+2} & c_{3n+2} & d_{3n+2} \end{bmatrix},$$

$$R_n = \begin{bmatrix} g_{3n-2} & 0 & 0 \\ f_{3n} & g_{3n} & 0 \\ e_{3n+2} & f_{3n+2} & g_{3n+2} \end{bmatrix},$$

$$D_n = w_{eq} \begin{bmatrix} 0 \\ \delta_{n,0} \\ 0 \end{bmatrix}, \text{ and } W_n = \begin{bmatrix} w_{3n-2} \\ w_{3n} \\ w_{3n+2} \end{bmatrix}. \quad (11)$$

We solve this three-term recurrence relation using matrix continued fractions¹⁶. The solution is given in Appendix A. Now that we have determined the atomic response, we calculate the gain experienced by the probe fields.

The time-averaged product of the probe field and the time derivative of the polarization gives the gain experienced by the probe field. The gain of the in-phase subharmonic probe field is proportional to the real part of the first harmonic of v .

$$d\delta\xi'/dz = \alpha \operatorname{Re}\{v_1 \exp(-i\theta')\} / 2\kappa T_2 \quad (12a)$$

The gain of the in-quadrature subharmonic probe field is proportional to the imaginary part of the first harmonic of u .

$$d\delta\xi''/dz = \alpha \operatorname{Im}\{u_1 \exp(-i\theta'')\} / 2\kappa T_2 \quad (12b)$$

3. Discussion of results

In Fig. 2 we plot the in-phase subharmonic probe-field gain as a function of modulation frequency for various strong-field intensities. At low intensities the probe-field gain is a Lorentzian in modulation frequency with a width of $1/T_2$. As the intensity of the strong field is increased, the gain curve develops a dip near zero modulation frequency. The dip has a width of $1/T_1$. The presence of this dip implies that the probe field will experience the greatest gain for a nonzero modulation frequency. In Fig. 3 we plot the in-quadrature subharmonic probe-field gain as a function of modulation frequency for various strong-field intensities. Again we see that at low intensities the probe-field gain is a Lorentzian in modulation frequency with a width of $1/T_2$. As the strong-field intensity is increased, the gain curve develops an anti-dip near zero modulation frequency.

The calculations have shown both quadratures of the probe-field gain to be independent of θ' and θ'' . In Appendix B we show analytically that the in-quadrature subharmonic probe-field gain is independent of θ'' . The independence of subharmonic gain from the phase difference between the oscillations of the probe field and the oscillations of the strong field, implies that the subharmonic component

of the polarization is directly proportional to the subharmonic field. In contrast, it can be shown that the harmonic probe-field gain exhibits a strong dependence on the phase difference between the strong-field oscillations and the harmonic probe-field oscillations¹⁴. Also, if the amplitude of the probe fields is increased, so that their interaction can no longer be considered only to first order, the gain of the subharmonic field becomes dependent on θ . The independence of the gain from the phase implies the instabilities predicted may be symmetry-breaking instabilities. The phase of the light field for a laser at the first laser threshold displays similar behavior¹⁷.

In Figs. 4 and 5 we show, respectively, the in-phase and in-quadrature subharmonic probe-field gains for larger strong-field intensities. In both cases, additional structure begins to develop about the initial feature. The additional maxima and minima seem to move out with a parabolic dependence on intensity.

In Figs. 6 and 7 we plot the peak positions of the subharmonic gain curves as a function of modulation frequency and amplitude of the strong field. Here we can clearly see the peaks move out to higher frequencies linearly as the electric field increases. This linear dependence suggests a connection between these resonances and the Rabi frequency. In contrast to the two-field problem, where the position of the resonances are found to be independent of the damping rates⁸, the position of the subharmonic probe-field resonances do display a dependence on damping. The maxima occurring at the largest modulation frequency varies most drastically with variation of the ratio between T_1 and T_2 . The subsequent peaks vary less and less sensitively. The physical mechanism responsible for this behavior is not well understood. Some of the features, however, are similar in behavior to that seen in multiphoton absorption¹⁸. Subharmonic resonances such as these are also present in the two-frequency problem and have also been predicted in other multichromatic analyses¹⁸.

In Fig. 8 we show the strong-field gain as a function of modulation frequency for a fixed strong-field amplitude. In reference 8 the maxima in the strong-field gain curve were found to occur where the zeroth order Bessel function, $J_0(2\kappa\xi / \delta\omega)$ is equal to zero. For large Rabi frequencies, $\kappa\xi$, and small modulation frequencies, $\delta\omega$, the zeroes of the Bessel function become equally spaced. It is in these regimes that the resonances become subharmonics. In Fig. 9 we plot the in-phase, in-quadrature, and strong-field gains as a function of modulation frequency for the same parameters as Fig. 8. At this intensity the in-quadrature probe-field gain is always positive; it exceeds the strong-field gain for all modulation frequencies, except in the vicinity of the absolute maxima of the strong-field gain curve. The in-phase probe-field gain takes on both positive and negative values as a function of modulation frequency. It can also be noted that the oscillations in modulation frequency of the two subharmonic gain curves are 180° out of phase with the oscillations in modulation frequency of the strong-field gain. It is important to remember, however, the frequency separation of the probe fields is one third the modulation frequency, $\delta\omega$. This means the presence of a frequency-dependent loss influences the two curves differently. For instance, a frequency-dependent loss that is larger for larger frequencies, reduces the strong-field curve more than the probe-field curve. This reduction makes the probe-field gain larger than the strong-field gain. If the strong field is the field in a laser, this reduction allows the probe field sufficient gain to overcome losses and begin oscillation. The severity of the frequency-dependent loss determines the point at which the instability will occur. The experiments of Hillman *et al.*⁶ and Stroud *et al.*¹⁹ confirm these conclusions.

In Fig. 10 and Fig. 11 we plot a series of in-phase and in-quadrature subharmonic probe-field gain curves for fixed strong-field amplitude as a function of modulation frequency and three different ratios of damping times. The ratios chosen are indicative of collisional dephasing ($T_2 \ll T_1$), strong collisions ($T_2 = T_1$), and

radiative broadening ($T_2 = 2 T_1$). These plots indicate the shape of the in-phase gain curve is not a strong function of the ratio of damping times. However, as noted before, the positions of the maxima do show a dependence on the ratio between T_1 and T_2 . The in-quadrature subharmonic probe-field gain does indicate a dependence on the ratio of T_1 and T_2 for modulation frequencies less than $1/T_2$. However, for modulation frequencies greater than the linewidth, $1/T_2$, the curves are quite similar in form and only show a weak dependence on the ratio of T_1 to T_2 .

Conclusions

We have calculated the atomic response to a pair of 100% AM fields. We used this solution to calculate the gain seen by a 100% AM subharmonic probe field. The subharmonic probe field sees a Lorentzian lineshape in modulation frequency for the limit of small amplitude. As the strong-field amplitude is increased it modifies the lineshape experienced by the subharmonic probe field. The lineshape contains a primary resonance and subharmonic resonances of this primary resonance. The position of the resonances varies linearly with the Rabi frequency of the strong field. The location of the resonances also depends on the ratio of the inversion decay rate to the dipole decay rate.

We have also observed the gain of the subharmonic probe field to be independent of the phase between the oscillations of the strong field and the oscillations of the subharmonic probe field. This independence of phase implies the subharmonic response of the atom is directly proportional to the subharmonic field. It also predicts the instabilities will be independent of this phase difference.

The calculations also reveal that the 100% AM strong field is stable to the growth of subharmonic fields if there are no frequency-dependent loss mechanisms. However, if frequency-dependent loss mechanisms are present, we predict the 100% AM field will go unstable. The point at which the field goes unstable depends on the

severity of the frequency-dependent loss. This conclusion agrees well with observed instabilities in cw dye lasers^{5,19}.

Acknowledgements

We thank the Army Research Office-University Research Initiative for financial support of this work.

Appendix A

In this appendix we outline the method for calculating the gain of the subharmonic probe fields.

The larger harmonic components of w must become less significant if the Fourier series in Eq. (5) are to converge and the rotating-wave approximation is to remain valid. Therefore, we assume the harmonic components of the inversion, w_n , are negligible for $n > N$. With this assumption, the recurrence relation, Eq. (10), for $n = N$ can be written as

$$P_N W_{N-2} + Q_N W_N = 0, \quad (A1)$$

which implies

$$W_N = -Q_N^{-1} P_N W_{N-2}. \quad (A2)$$

The recurrence relation, Eq. (10), for $n = N-2$ can now be written as

$$P_{N-2} W_{N-4} + (Q_{N-2} - R_{N-2} Q_N^{-1} P_N) W_{N-2} = 0, \quad (A3)$$

which implies

$$W_{N-2} = -(Q_{N-2} - R_{N-2} Q_N^{-1} P_N)^{-1} P_{N-2} W_{N-4}. \quad (A4)$$

We continue in such a fashion, defining the larger index Fourier amplitudes in terms of the lower index Fourier amplitudes, until we reach the relation for $n = 2$. This relation has the following form.

$$W_2 = -(Q_2 - R_2(Q_4 - R_4(\dots(Q_{N-2} - R_{N-2} Q_N^{-1} P_N)^{-1} P_{N-2})^{-1} P_{N-4} \dots)^{-1} P_6)^{-1} P_4)^{-1} P_2 W_0, \quad (A5)$$

or more simply

$$W_2 = M W_0, \quad (A6)$$

where M is the matrix continued fraction, with elements m_{ij} . This expression, Eq. (A6), relates the harmonic components w_4 , w_6 , and w_8 to the harmonic components w_0 , w_2 , and w_{2^*} . Strictly speaking, the matrix, M , is a function of N . However, N is chosen sufficiently large so that M becomes independent of N to the desired accuracy of the calculation. This is our criterion of convergence. Since the inversion, w , is a real quantity, the Fourier components obey the relation

$$w_n = w_n^* . \quad (A7)$$

We now consider Eq. (8) for the cases $n = -4, -2, 0, 2, \text{ and } 4$. Using Eqs. (A6) and (A7) we write these five relations in matrix form as

$$S W = W_0 \quad (A8)$$

Where the vectors W and W_0 are

$$W = \begin{bmatrix} w_4^* \\ w_2^* \\ w_0 \\ w_2 \\ w_4 \end{bmatrix} , \quad \text{and} \quad W_0 = \begin{bmatrix} 0 \\ 0 \\ w_{eq} \\ 0 \\ 0 \end{bmatrix} . \quad (A9)$$

And the matrix S has elements s_{ij} where

$$\begin{aligned} s_{11} &= d_{-4} + a_{-4} m_{33}^* + b_{-4} m_{23}^* + c_{-4} m_{13}^* , \\ s_{12} &= e_{-4} + a_{-4} m_{32}^* + b_{-4} m_{22}^* + c_{-4} m_{12}^* , \\ s_{13} &= f_{-4} + a_{-4} m_{31}^* + b_{-4} m_{21}^* + c_{-4} m_{11}^* , \\ s_{14} &= g_{-4} , \\ s_{15} &= 0 , \\ s_{21} &= c_{-2} + a_{-2} m_{23}^* + b_{-2} m_{13}^* , \\ s_{22} &= d_{-2} + a_{-2} m_{22}^* + b_{-2} m_{12}^* , \\ s_{23} &= e_{-2} + a_{-2} m_{21}^* + b_{-2} m_{11}^* , \\ s_{24} &= f_{-2} , \\ s_{25} &= g_{-2} , \\ s_{31} &= b_0 + a_0 m_{13}^* , \\ s_{32} &= c_0 + a_0 m_{12}^* , \\ s_{33} &= d_0 + a_0 m_{11}^* + g_0 m_{11} , \end{aligned} \quad (A10)$$

$$\begin{aligned}
s_{34} &= s_{32}^* , \\
s_{35} &= s_{31}^* , \\
s_{41} &= a_2 , \\
s_{42} &= b_2 , \\
s_{43} &= c_2 + f_2 m_{11} + g_2 m_{21} , \\
s_{44} &= d_2 + f_2 m_{12} + g_2 m_{22} , \\
s_{45} &= e_2 + f_2 m_{13} + g_2 m_{23} , \\
s_{51} &= 0 , \\
s_{52} &= a_4 , \\
s_{53} &= b_4 + e_4 m_{11} + f_4 m_{21} + g_4 m_{31} , \\
s_{54} &= c_4 + e_4 m_{12} + f_4 m_{22} + g_4 m_{32} , \text{ and} \\
s_{55} &= d_4 + e_4 m_{13} + f_4 m_{23} + g_4 m_{33} .
\end{aligned}$$

Equation (A8) represents a system of five linear equations with five unknowns. The solution gives us expressions for w_0 , w_2 , w_4 , and their complex conjugates. We can use these expressions to find the other Fourier components of w . From Eq. (6a) and Eq. (6b) we can then determine the Fourier components of u and v that determine the gain.

Appendix B

In this appendix we show that the gain of the in-quadrature subharmonic probe field is independent of the phase difference, θ'' , between the oscillations of the subharmonic probe field and the strong 100% AM field.

The solution for the atomic response to a single resonant 100% AM field has been found in reference 8. If we linearize the Bloch equations about this solution, the equation of motion for the perturbation to the slowly varying amplitude of the in-phase dipole moment becomes

$$\delta \dot{u} = -\delta \Omega''(t) w_{AM} - \delta u / T_2 . \quad (B1)$$

Where δu is the perturbation to the slowly varying amplitude of the in-phase dipole moment. The perturbative field in-quadrature to the 100% AM field is $\delta\Omega''(t)$. The stationary solution for the inversion to the Bloch equations driven by a resonant 100% AM field is w_{AM} . Recall w_{AM} can be written as

$$w_{AM} = \sum_{n=-\infty}^{\infty} w_n \exp(in\delta\omega t) . \quad (B2)$$

If $\delta\Omega''(t) = 2\delta\Omega'' \sin(\frac{1}{3}\delta\omega t + \theta'')$ we can employ Floquet's theorem and write the stationary solution to Eq. (B1) as

$$\delta u = \sum_{n=-\infty}^{\infty} \delta u_n \exp(\frac{1}{3}in\delta\omega t) . \quad (B3)$$

This assumption leads to the following recurrence relation

$$(1 + \frac{1}{3}in\delta\omega T_2) \delta u_n = i\delta\Omega'' T_2 (w_{(n-1)/3} \exp(i\theta'') - w_{(n+1)/3} \exp(-i\theta'')) . \quad (B4)$$

The gain of the in-quadrature subharmonic probe field is proportional to

$\delta u_1 \exp(-i\theta'')$. From Eq. (B4) we find

$$\delta u_1 \exp(-i\theta'') = i\delta\Omega'' T_2 w_0 / (1 + \frac{1}{3}i\delta\omega T_2) . \quad (B5)$$

The right hand side of Eq. (B5) is independent of θ'' ; this implies the in-quadrature subharmonic probe-field gain is independent of the phase difference between the oscillations of the in-quadrature probe field and the oscillations of the strong field.

REFERENCES

1. This issue of the journal is a special issue on instabilities in optically active media. N. B. Abraham, L. A. Lugiato, and L. M. Narducci, *J. Opt. Soc. Am. B* 2, 7 (1985).
2. This issue of the journal is a special issue on laser instabilities. D. K. Bandy, A. N. Oraevsky, and J. R. Tredicce, *J. Opt. Soc. Am. B* 5, 879-1215 (1988).
3. C. O. Weiss and J. Brock, *Phys. Rev. Lett.* 57, 2804 (1986).
4. R. S. Gioggia and N. B. Abraham, *Phys. Rev. Lett.* 51, 650 (1983).
5. L. W. Hillman, J. Krasinski, R. W. Boyd, and C. R. Stroud, Jr., *Phys. Rev. Lett.* 52, 1605 (1984).
6. T. H. Maiman, *Nature* 187, 493 (1960).
7. L. A. Lugiato, L. M. Narducci, E. V. Eschenazi, D. K. Bandy, and N. B. Abraham, *Phys. Rev. A* 32, 1563 (1985).
8. L. W. Hillman, J. Krasinski, K. Koch, and C. R. Stroud, Jr., *J. Opt. Soc. Am. B* 2, 211 (1985).
9. H. Fu and H. Haken, *Phys. Rev. A* 36, 4802 (1987).
10. H. Fu and H. Haken, *J. Opt. Soc. Am. B* 5, 899-908 (1988).
11. H. Fu and H. Haken, *Phys. Rev. Lett.* 60, 2614-2617 (1988).
12. Y. Pomeau, B. Dorizzi, and B. Grammaticos, *Phys. Rev. Lett.* 56, 681 (1986).
13. E. T. Whittaker and G. N. Watson, *Modern Analysis*, (Cambridge University, Cambridge, 1965).
14. To be published K. Koch, B. J. Oliver, S. H. Chakmakjian, C. R. Stroud, Jr., and L. W. Hillman
15. L. Allen and J. Eberly, *Optical Resonance and Two-Level Atoms*, (John Wiley & Sons, Inc. New York, 1975).
16. H. Risken and H. D. Vollmer, *Z. Physik B* 39, 339 (1980).
17. H. Haken, *Synergetics*, (Springer-Verlag, Berlin, 1983).
18. G. S. Agarwal and N. Nayak, *J. Phys. B* 19, 3385 (1986).
19. C. R. Stroud, Jr., K. Koch, and S. H. Chakmakjian, in *Optical Instabilities*, eds. R. W. Boyd, M. G. Raymer, and L. M. Narducci (Cambridge University, Cambridge, 1986) pp. 274-276.

Figure Captions

- Figure 1. The applied field spectrum. We plot the spectrum of the field used for the calculation as vertical arrows. The field is assumed to be symmetrically placed about the atomic resonance, ω_{atom} . The atomic resonance is graphically displayed as a Lorentzian lineshape. The field is made up of frequency components at $\omega - 3\delta\omega$, $\omega - \delta\omega$, $\omega + \delta\omega$, and $\omega + 3\delta\omega$. The components at $\omega + 3\delta\omega$ and $\omega - 3\delta\omega$ are referred to as the strong field in the text.
- Figure 2. In-phase subharmonic probe-field gain. We plot the in-phase subharmonic probe-field gain as a function of $\delta\omega$, for various values of the strong-field intensity. A dip in the center of the gain curve develops at low intensity. This means that the maximum gain occurs for nonzero modulation frequencies. The time-averaged strong-field intensity, $I_1 = 2(\kappa\xi_1)^2 T_1 T_2 = 0, \frac{1}{2}, 1, 2, 3, 4, 5, 6$. The inversion decay time $T_1 = 10 T_2$.
- Figure 3. In-quadrature subharmonic probe-field gain. We plot the in-quadrature subharmonic probe-field gain as a function of $\delta\omega$, for various values of the strong-field intensity. In contrast to the in-phase subharmonic probe-field gain, the in-quadrature subharmonic probe-field gain develops an antidip near the center of the gain curve. The intensities and decay times are the same as in Fig. 2.
- Figure 4. In-phase subharmonic probe-field gain. We plot the in-phase subharmonic probe-field gain as a function of $\delta\omega$, for larger values of the strong-field intensity. Structure develops within the dip that formed at low intensity. The additional structure appears at subharmonics of the main resonance. The time-averaged strong-field intensity, $I_1 = 2(\kappa\xi_1)^2 T_1 T_2 = 10, 20, 30, 40, 50, 60, 70, 80, 90, 100$. The inversion decay time $T_1 = 10 T_2$.

Figure 5. In-quadrature subharmonic probe-field gain. We plot the in-quadrature subharmonic probe-field gain as a function of $\delta\omega$, for larger values of the strong-field intensity. Additional structure appears outside the antidip formed at low intensity. These peaks also appear at subharmonics of the main resonance. The time-averaged strong-field intensity, $I_1 = 2(\kappa\xi_1)^2 T_1 T_2 = 10, 20, 30, 40, 50, 60, 70, 80, 90, 100$. The inversion decay time $T_1 = 10 T_2$.

Figure 6. Peak positions of the in-phase subharmonic probe-field gain. We plot the peak positions of the in-phase subharmonic probe-field gain as a function of Rabi frequency, $\kappa\xi_1$, and modulation frequency, $\delta\omega$. The position of the resonances in modulation frequency varies linearly with the strong-field Rabi frequency. The inversion decay time $T_1 = 10 T_2$.

Figure 7. Peak positions of the in-quadrature subharmonic probe-field gain. We plot the peak positions of the in-quadrature subharmonic probe-field gain as a function of Rabi frequency, $\kappa\xi_1$, and modulation frequency, $\delta\omega$. The position in modulation frequency of the resonances of the in-quadrature subharmonic probe-field gain also vary linearly with strong-field Rabi frequency. The slopes of the lines are equal to the slopes of the lines in Fig. 6. The decay times are the same as in Fig. 6.

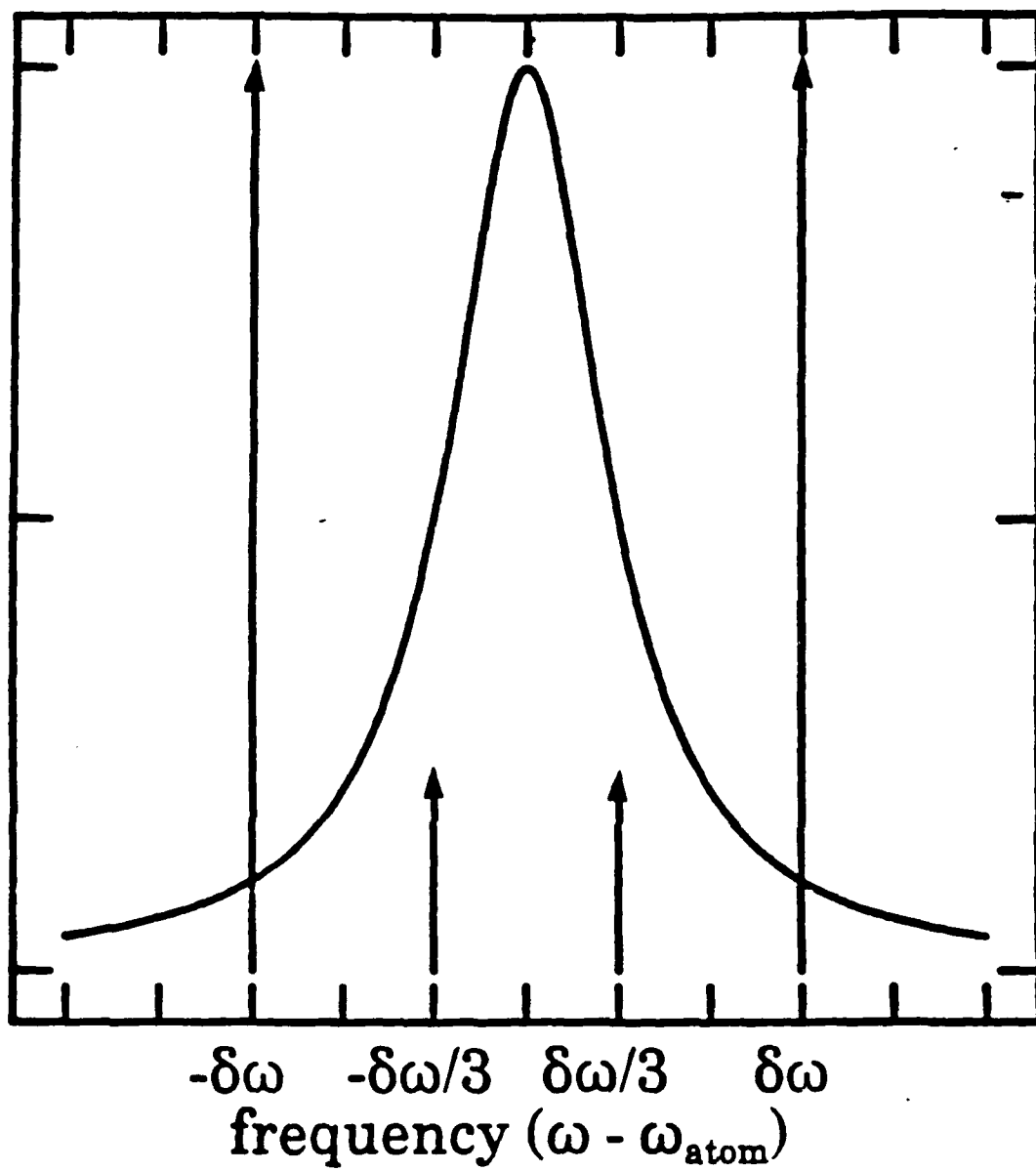
Figure 8. Strong-field gain curve. We plot the strong-field gain as a function of modulation frequency, $\delta\omega$. The maxima occur at the zeroes of the zeroth-order Bessel function, $J_0(2\kappa\xi_1/\delta\omega)$. The Rabi frequency of the strong field is $\kappa\xi_1 = 5/T_2$. The inversion decay time $T_1 = 10 T_2$.

Figure 9. The gain curve of the three pairs of fields. We plot the (a) strong-field gain, (b) in-phase subharmonic probe-field gain and (c) in-quadrature subharmonic probe-field gain as a function of modulation frequency, $\delta\omega$ for the same parameters as Fig. 8. The absolute maxima of the strong-field gain curve exceeds the subharmonic probe field gains. At that modulation frequency the strong-field will be stable to the growth of subharmonic probe fields.

Figure 10. The influence of damping on the in-phase subharmonic probe-field gain.

We plot the in-phase subharmonic probe-field gain as a function of modulation frequency for three different ratios of T_1 to T_2 . The Rabi frequency of the strong field, $\kappa\xi_1 = 3/T_2$. The inversion decay times for the three curves are (a) $T_1 = \frac{1}{2}T_2$, (b) $T_1 = T_2$, and (c) $T_1 = 10T_2$.

Figure 11. The influence of damping on the in-quadrature subharmonic probe-field gain. We plot the in-quadrature subharmonic probe-field gain as a function of modulation frequency for three different ratios of T_1 to T_2 . The Rabi frequency of the strong field, $\kappa\xi_1 = 3/T_2$. The inversion decay times for the three curves are (a) $T_1 = \frac{1}{2}T_2$, (b) $T_1 = T_2$, and (c) $T_1 = 10T_2$.



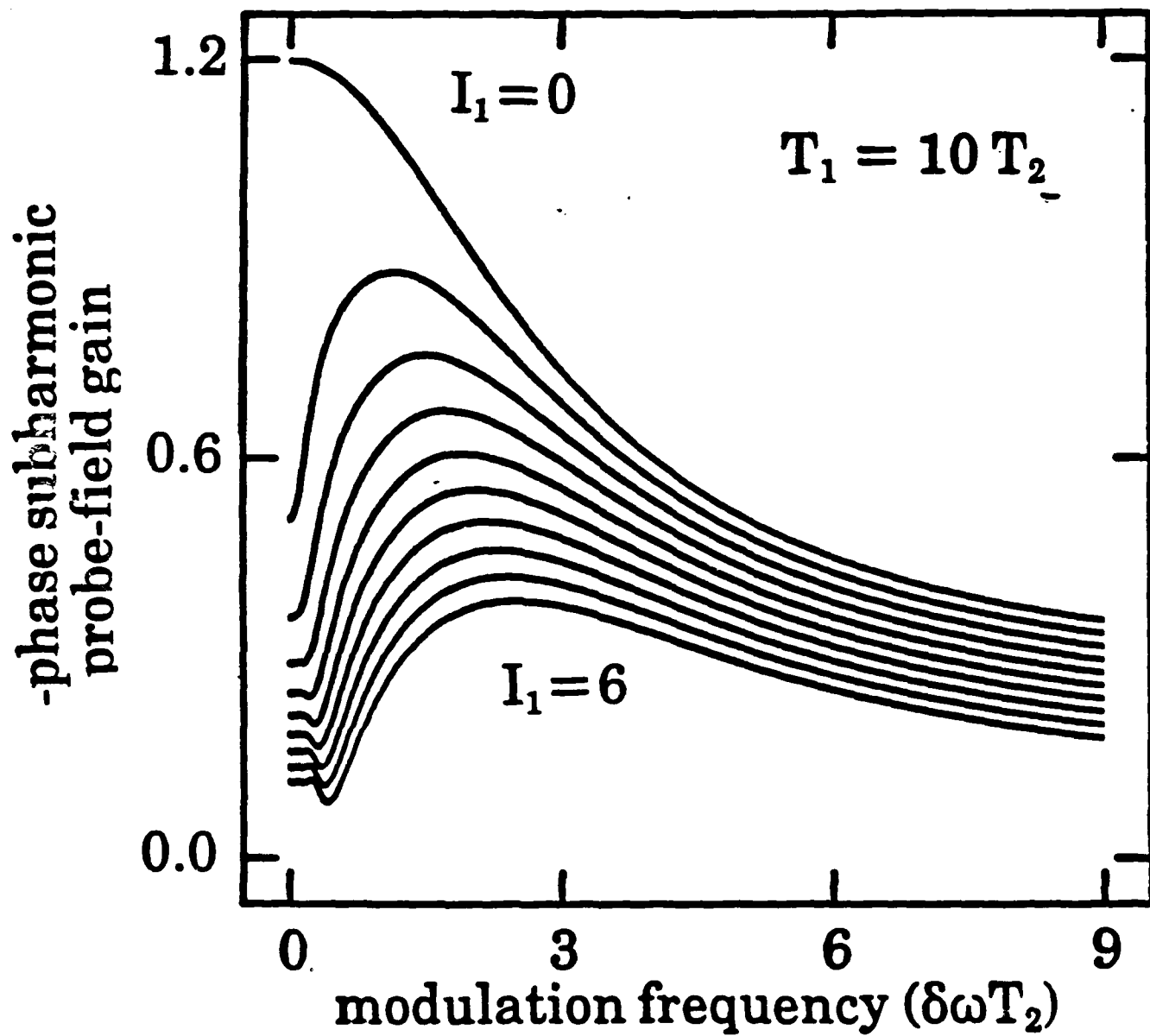


Fig. #2

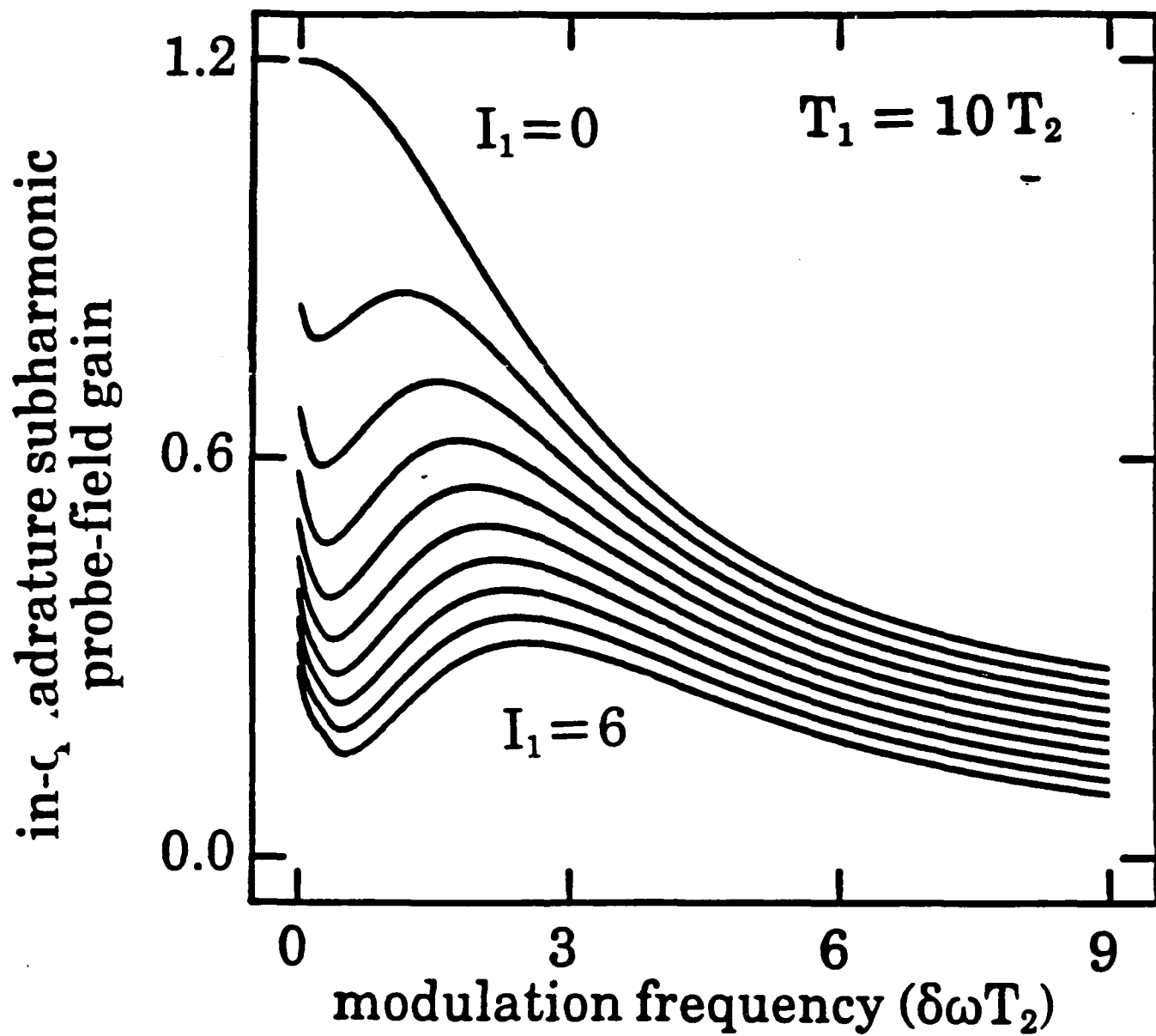


Fig. 3

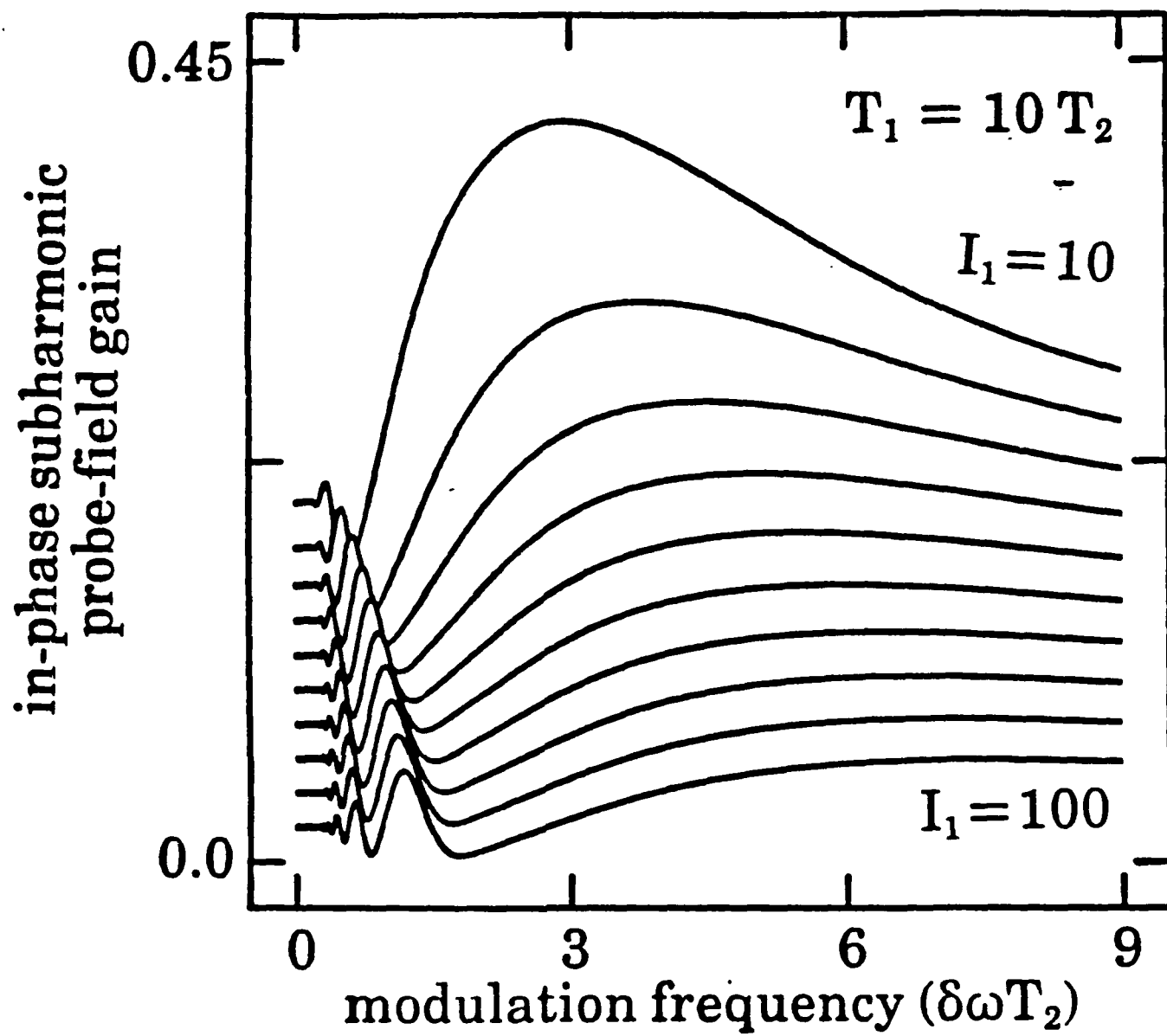


Fig. 4

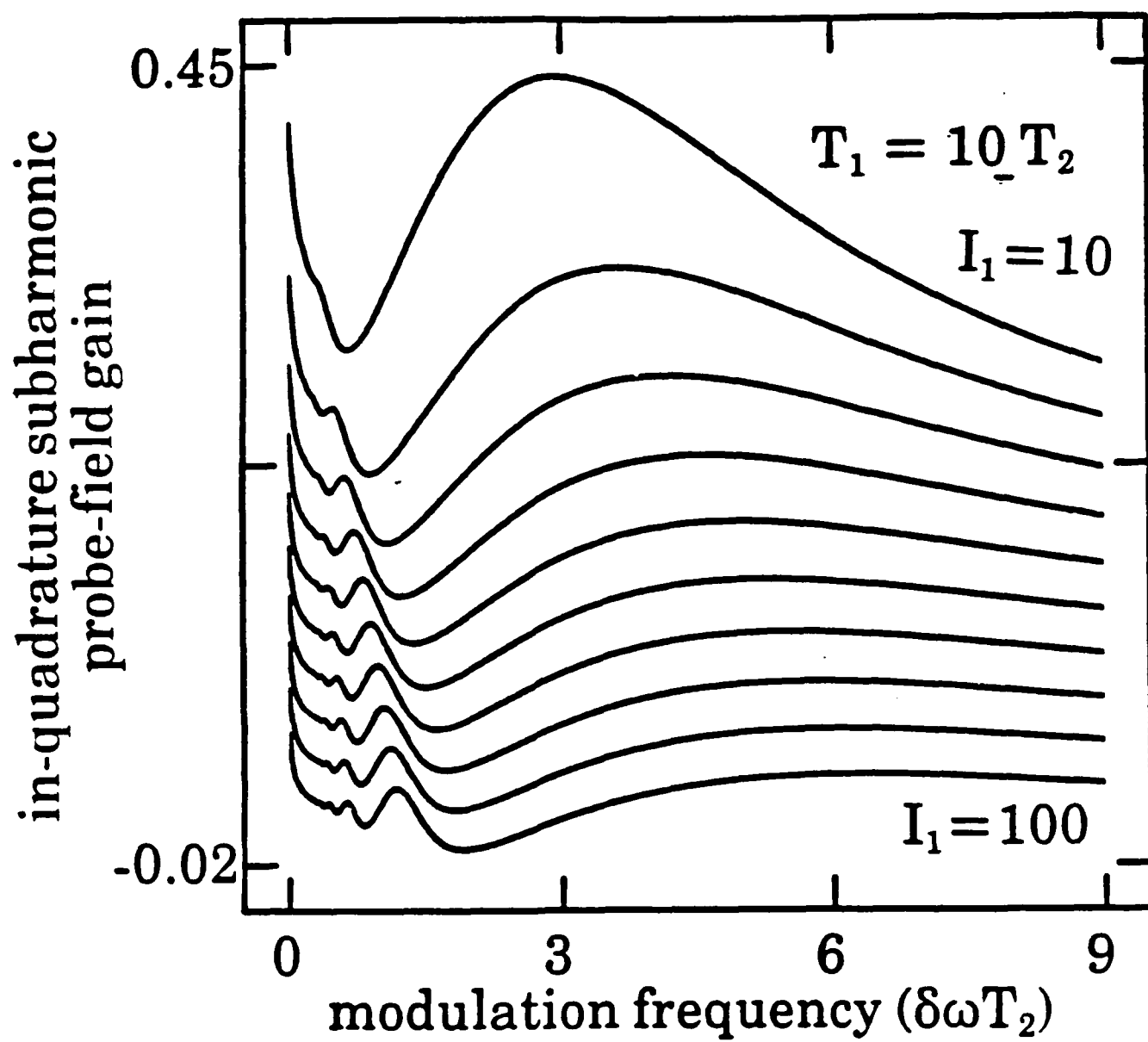


Fig. 5

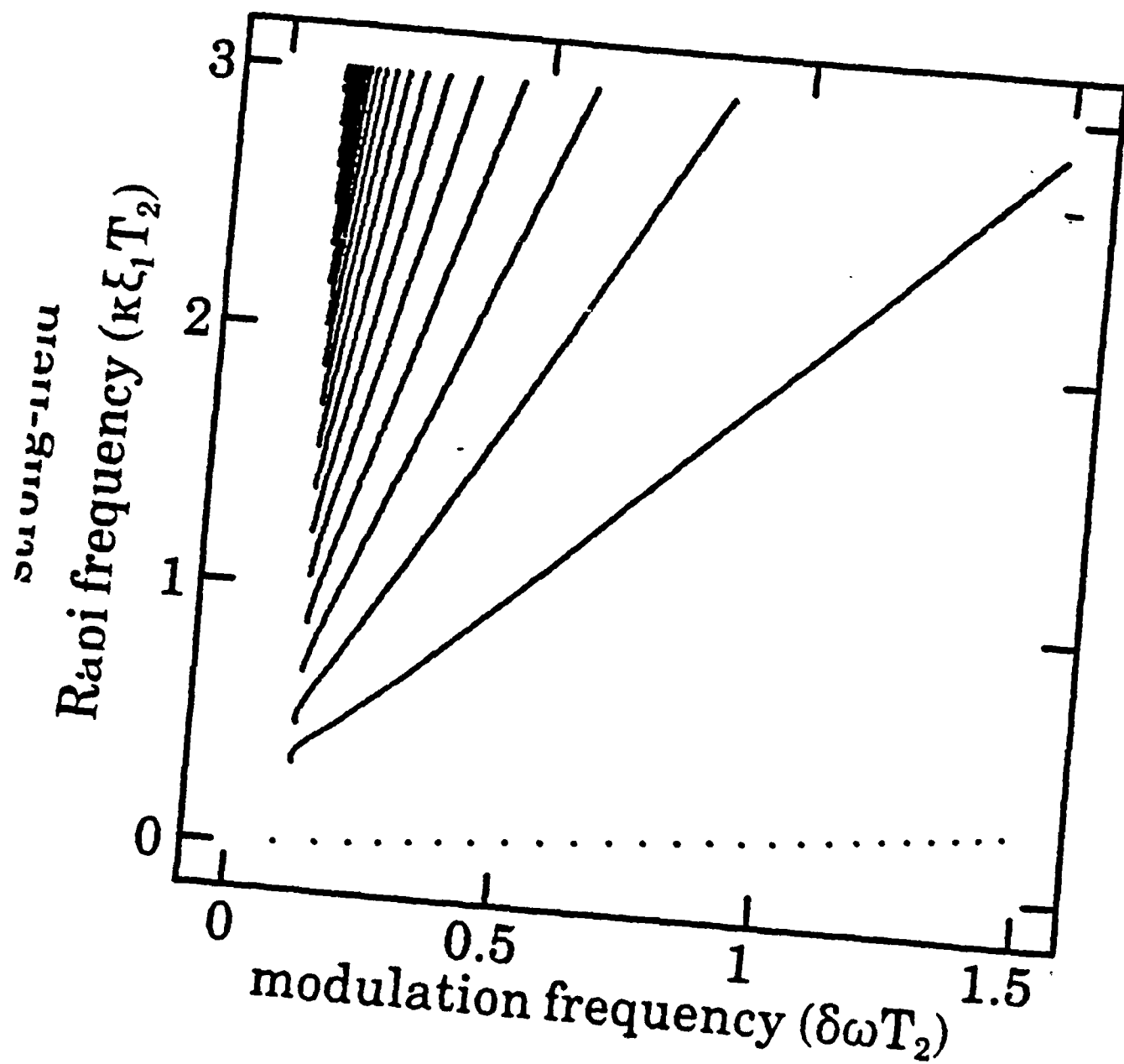


Fig. 6

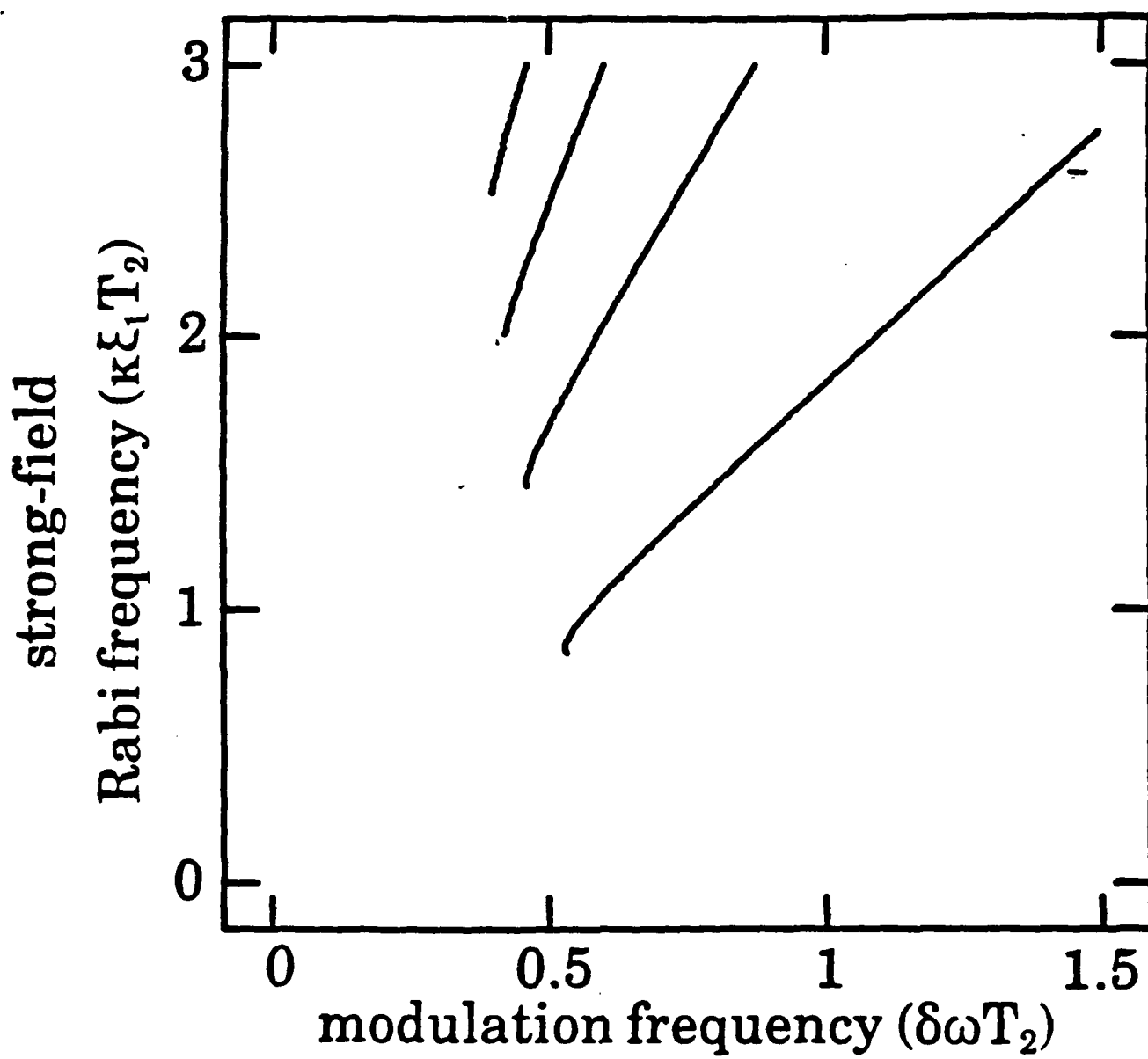


Fig. 7

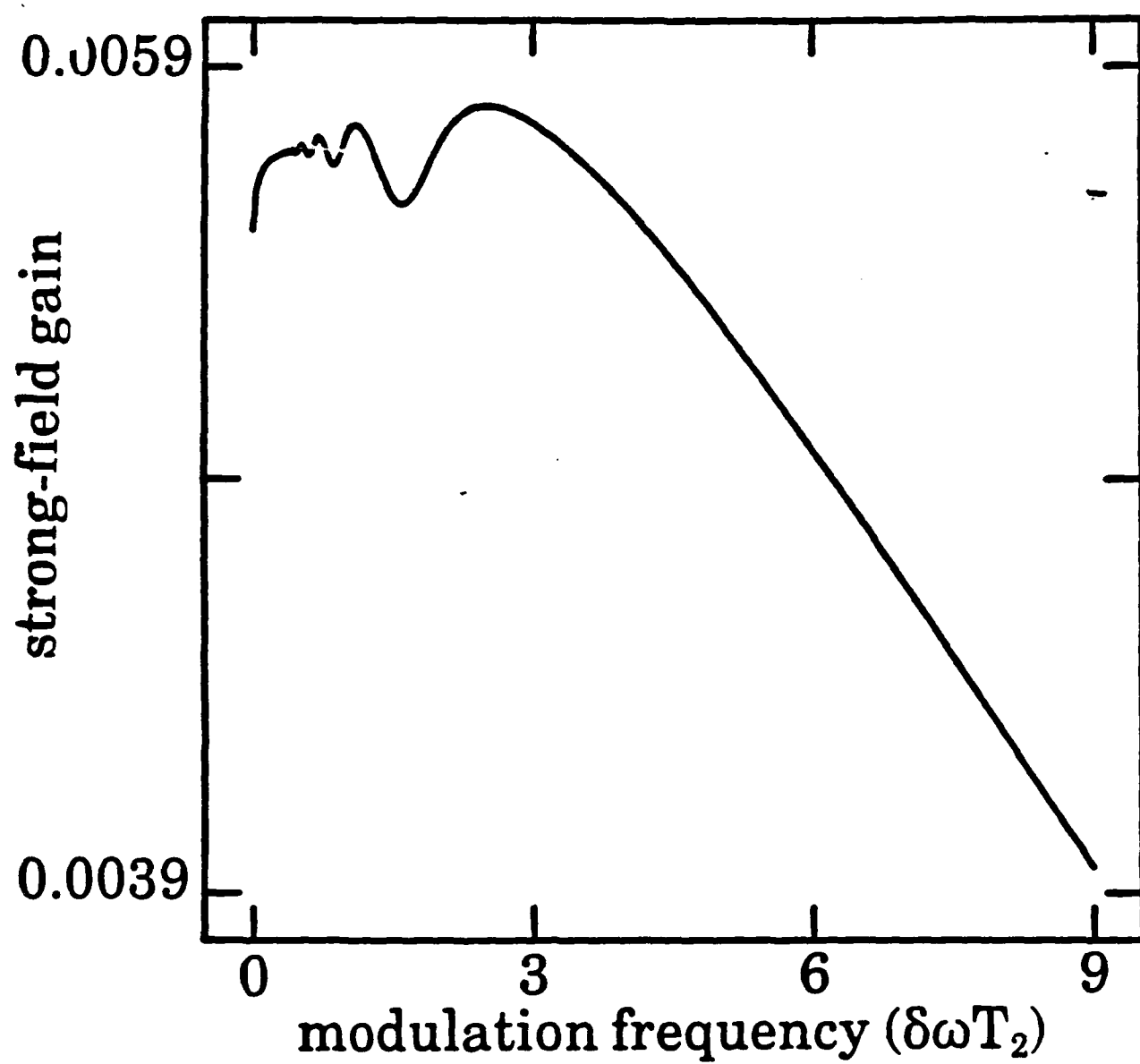


Fig. 8

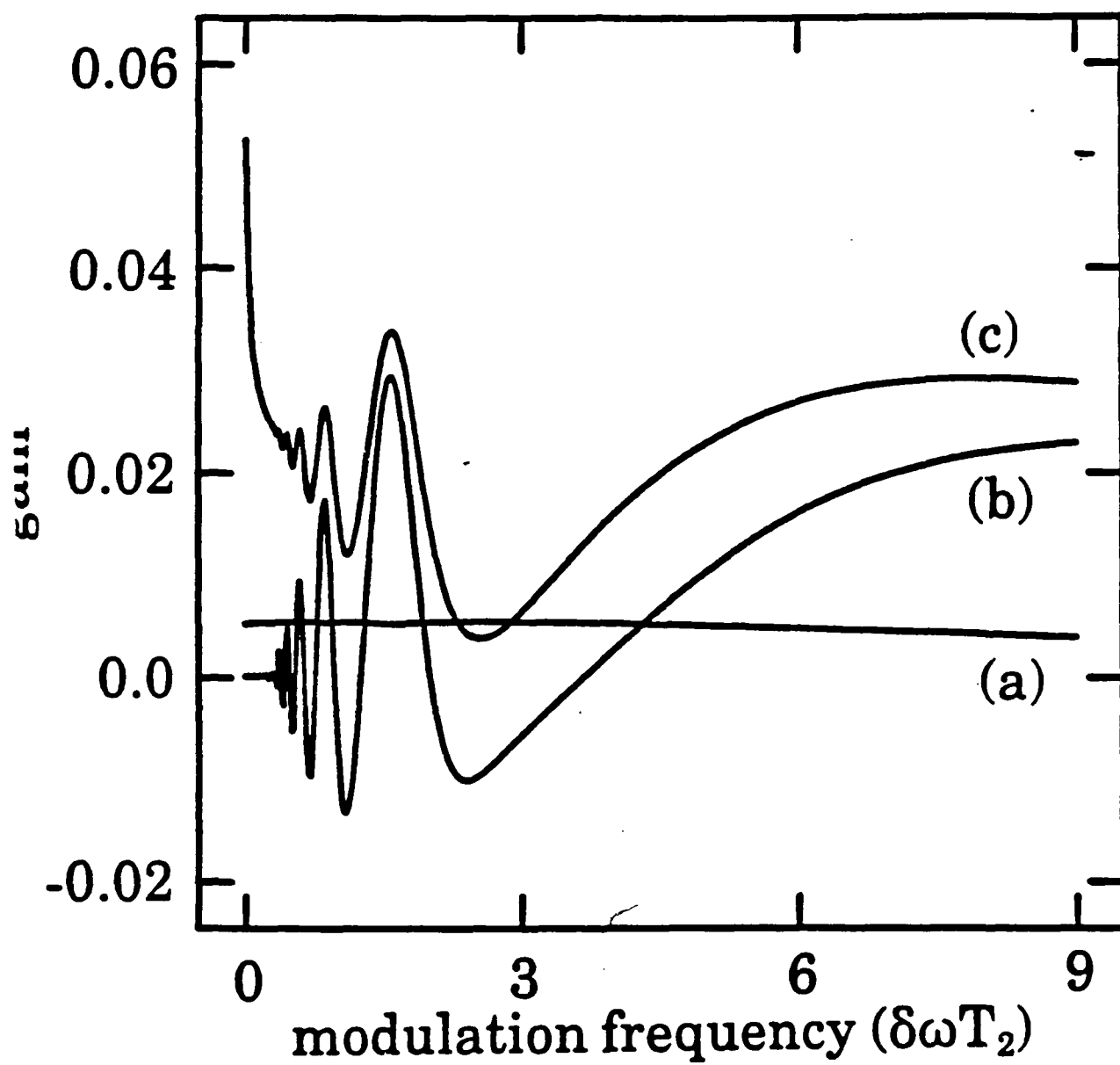


Fig. 9

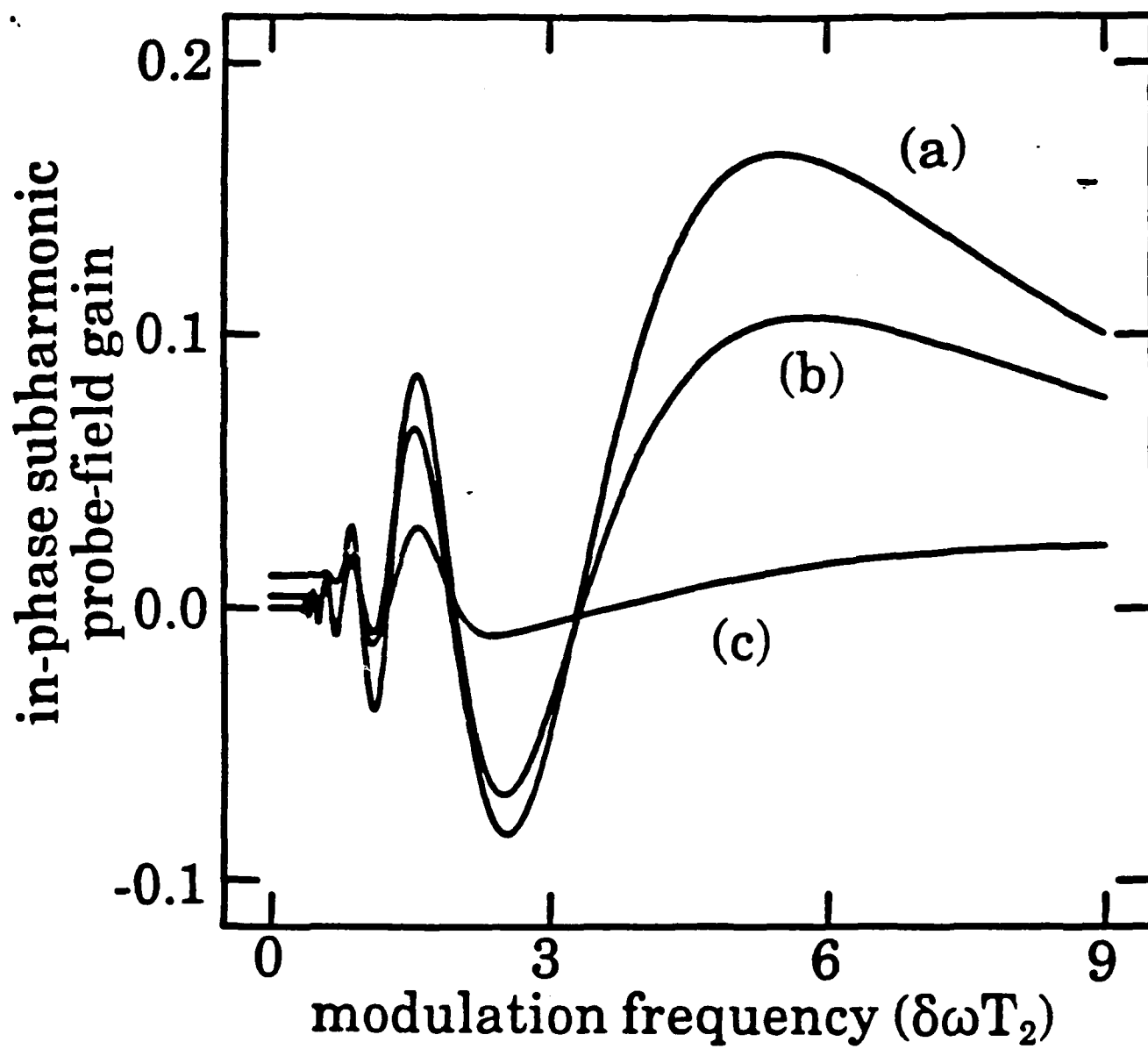


Fig. 10

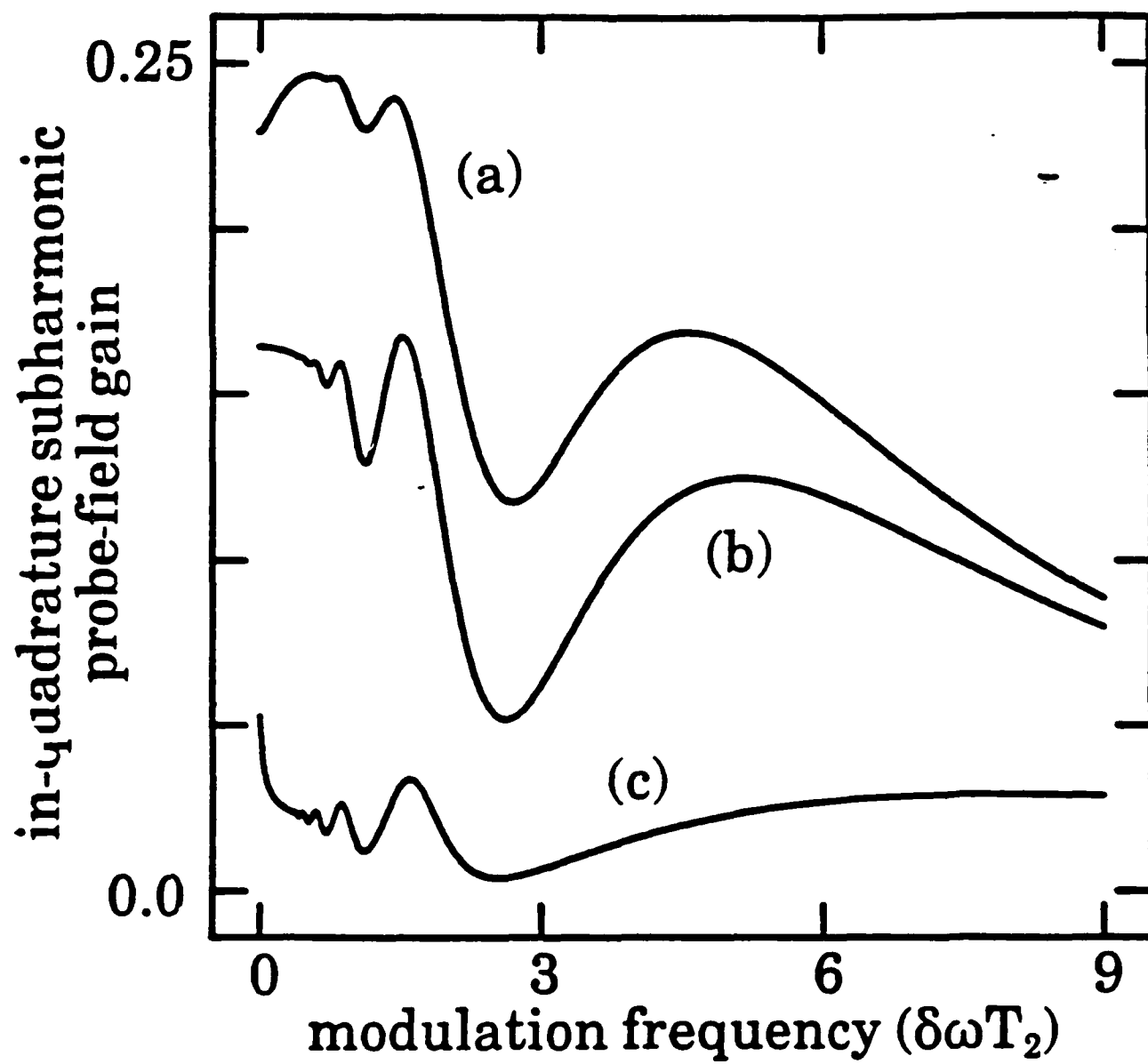


Fig. 11

**CECOM CENTER FOR NIGHT VISION AND ELECTRO-OPTICS
NEEDS FOR BROADBAND MATERIALS AND SYSTEMS**

NEEDS FOR BROADBAND MATERIALS AND SYSTEMS

- Broadband emitters in the 1 micron band for either flashlamp or diode-array pumping.
- Broadband absorber in the 800 nm region to match diode-array emission, with a single or broadband emissions in the 1 micron region.
- Non-linear materials to provide second and third harmonic generators, and OPO materials for the visible, the near IR, the mid IR and the far IR, at room temperature.
- * Broadband emitters (tunable materials) in the one-micron band based upon the Tanabe-Sugano crystal field dependence of the transition metal energy level system.

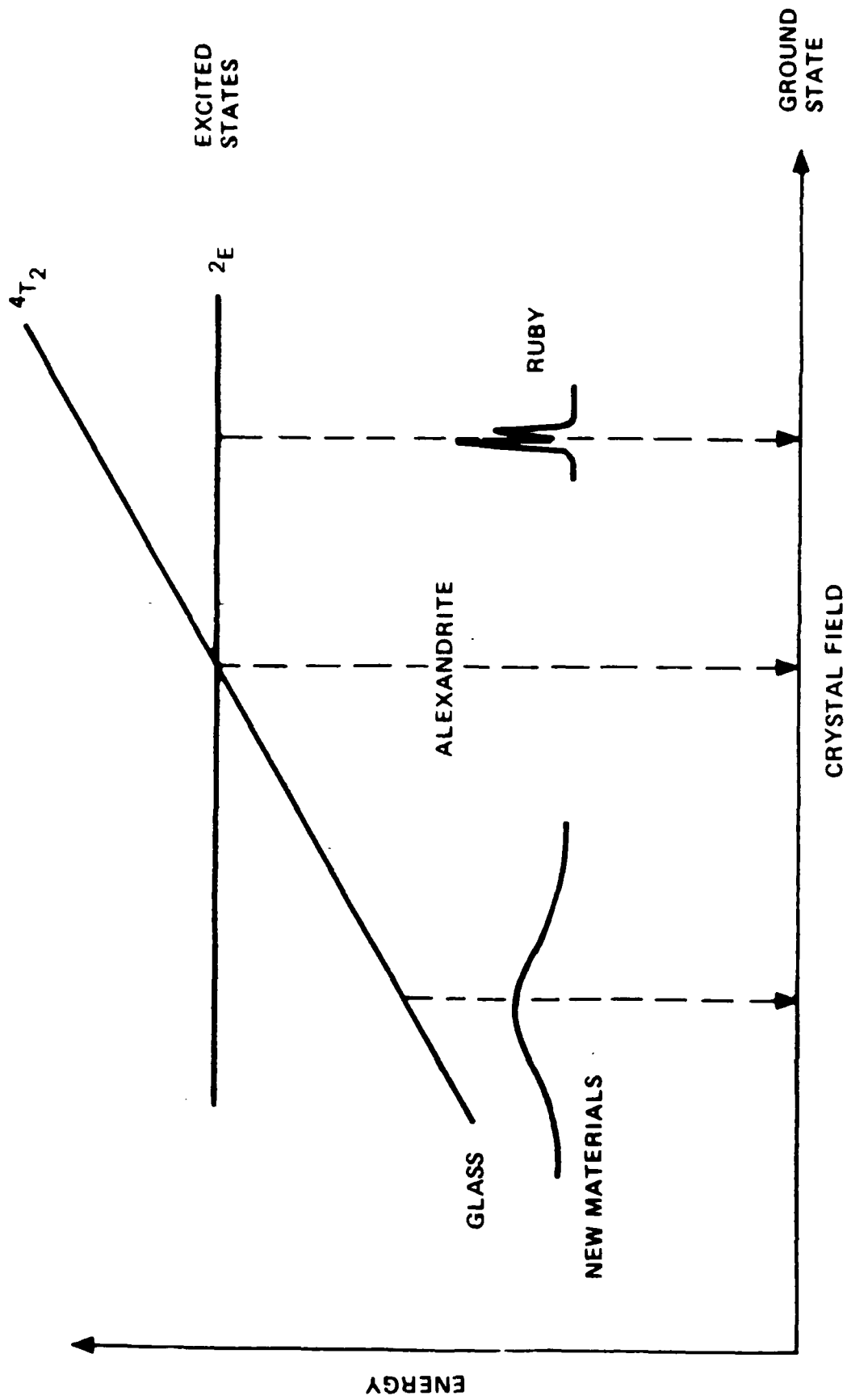
Example of Cr^{3+} (a d³ electron system) in sapphire, alexandrite.

These last two examples are not suitable because they lase in the wrong band, (around 750nm) and their lasing transition lifetimes are too short, (order of 10 microsec or less).

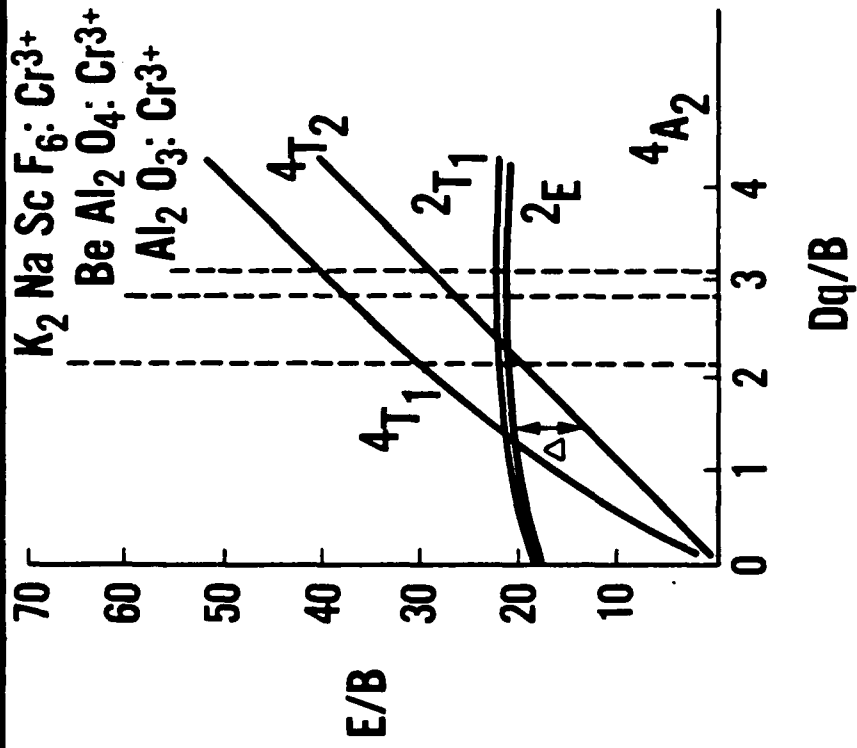
Ti^{3+} offers a possibility, with its d'electronic state, to provide a system with little or no deleterious excited state absorption.

These are phonon terminated laser transition which give rise to the tunability at the desired wavelengths.

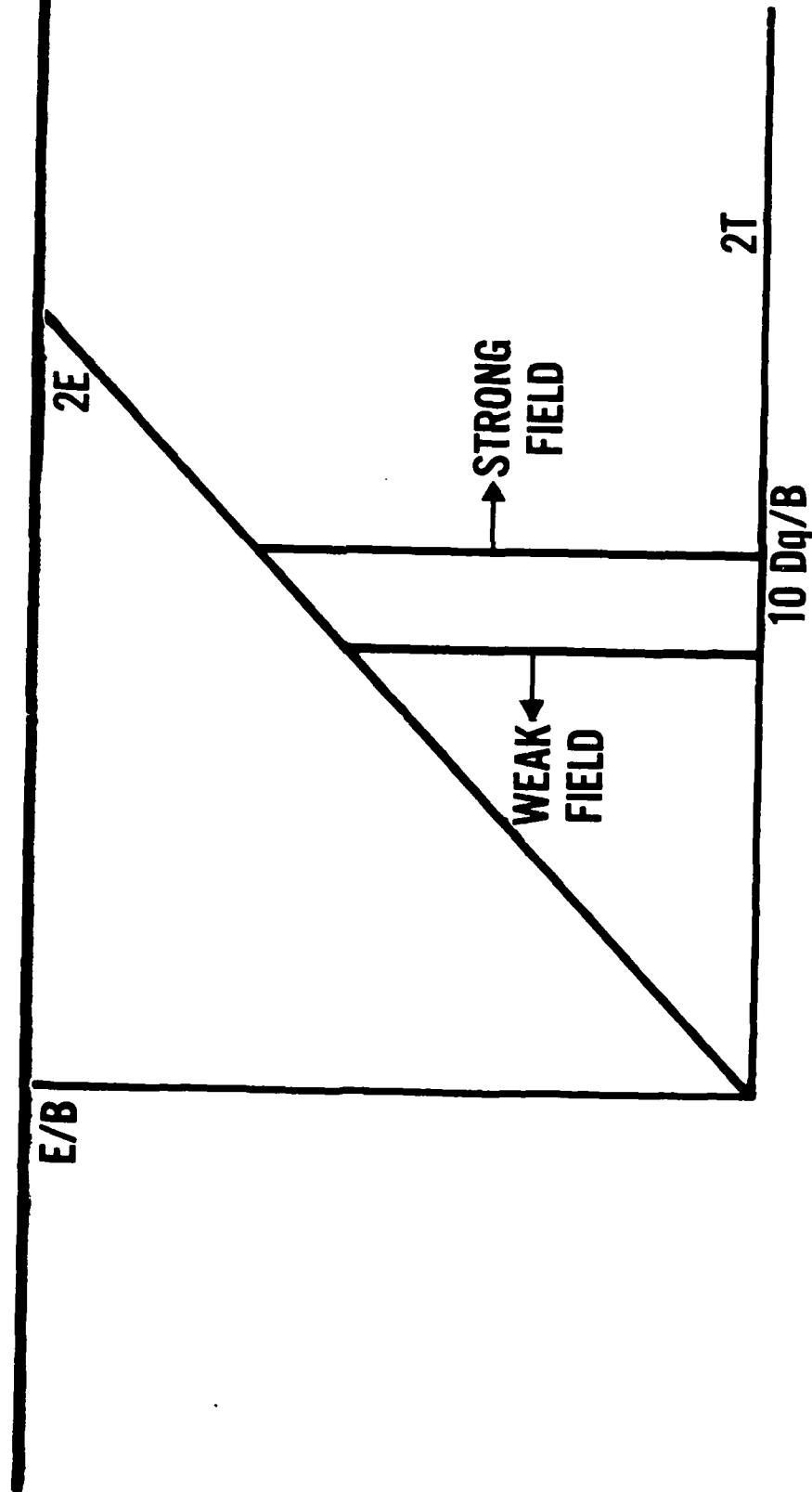
Cr³⁺ ENERGY LEVELS



TANABE-SUGANO ENERGY DIAGRAM



TANABE-SUGANO-TYPE DIAGRAM FOR Ti^{3+}



LIST OF EQUIPMENT AVAILABLE

- CW dye laser system including a 20 W Argon laser and a stabilized ring dye laser (Coherent)
- Various ancillary measuring equipment such as: lock-in amplifiers, box-car integrators, high-speed storage oscilloscope
- Various computers and peripherals
- Optical light chopper
- X-ray fluorescence spectrometer (Kevex)
- X-ray generator (Philips) for diffraction analysis
- Visible and near IR interferometer (Zygo)
- Pulsed double-beam spectrofluorometer (Spex) with detectors both in the visible and near IR
- Streak camera and monochromator (Hamamatsu) with various ancillary components
- Vacuum pumping system (Baltzers)
- Single-crystal x-ray diffractometer (Nicolet)
- Fume hood
- Pulsed Nd dye-laser system: 1 Joule pump, doubles and triples converters
- Various Newport optical tables with pneumatic support
- Various He-Ne lasers
- Various imaging viewers ramping from S1 photocathode to F.R density
- Low-temperature de _____ (down to 100K)

**CECOM CENTER FOR NIGHT VISION AND ELECTRO-OPTICS
V4+ IN CORUNDUM: CRYSTAL GROWTH AND SPECTROSCOPY**

V^{4+} in Corundum: Crystal Growth and Spectroscopy

H. Verdun, U. Brauch, G. de la Fuente,
L. Thomas and E. Behrens
Fibertek, Inc.
510-A Herndon Parkway
Herndon, VA 22070

T. Allik and Susan Stewart
Science Applications International Corporation
1710 Goodridge Drive
McLean, VA 22102

A. Pinto and W. Hovis
U.S. Army Night Vision & Electro-Optics Center
Fort Belvoir, VA 22060

Transition metal ions with the d^1 or d^9 electronic configuration, such as Ti^{3+} , V^{4+} and Cu^{2+} , are of particular interest for tunable solid state lasers. In these ions, the existence of basically only one high-lying excited state determines the absence of internal transitions that could produce excited state absorption. Ti^{3+} in corundum is an example of a successful system. V^{4+} in the same host looks also very promising.¹

In oxide hosts, vanadium can exist in a number of ionic states ranging from V^{2+} to V^{5+} . V^{3+} is by far the most stable ionic state of vanadium and, because of this, it is difficult to obtain significant concentrations of V^{4+} in this host. V^{4+} has been found to be present in small concentrations in corundum crystals grown by the Verneuil method. Annealing under oxygen produces the conversion of some V^{3+} into V^{4+} .² Gamma radiation is also effective for converting V^{3+} into V^{2+} and V^{4+} .³ Codoping with magnesium for charge compensation could have the effect of increasing even further the ratio of V^{4+} to V^{3+} in the as grown crystals.¹

Crystals of vanadium-doped corundum, codoped with magnesium, were grown using the laser-heated pedestal growth (LHPG) method.⁵ A 250 W CO₂ laser allowed us to grow crystals up to 3.5 mm in diameter. The LHPG method is an ideal tool for the study of the effects of growth atmosphere on the ionic valence of polyvalent dopants, such as vanadium, since it is free of the constraints imposed by the crucible material that limits the range of the oxygen fugacity that is tolerable in the growth atmosphere. The atmospheres used ranged from inert (low oxygen fugacity) to strongly oxidizing (about 47% oxygen in argon). An atmosphere with 18% oxygen gave the largest ratio of V⁴⁺ to V³⁺ in our crystals, as judged from the absorption spectrum, when the feed rods were prepared starting with an equimolar amount of magnesium and vanadium. With higher Mg/V ratios, the optimum was found to be at lower oxygen concentrations (at about 8% of oxygen for feed rods prepared with a starting composition containing twice as many moles of magnesium as vanadium). The final composition of the crystals could not be determined accurately with the analytical method available in our laboratory (x-ray fluorescence). The vanadium concentration in the crystals is certainly much lower than the initial concentration in the powder mixture as a significant amount of vanadium was lost during the sintering process used in the preparation of the feed rods. Further losses took place during the growth of the crystals.

The absorption, fluorescence and excitation spectra for sample #50 (size: 1.4 mm x 1.6 mm x 7.6 mm) are shown in Figure 1. These spectra were obtained at room temperature using unpolarized light and unoriented crystals. Their main features coincide with those reported in the literature.¹⁻⁴ The orange emission of V⁴⁺ in corundum extends from 520 nm to 800 nm peaking at about 640 nm. The position of the absorption bands can be inferred from the absorption and excitation spectra. The two humps peaking at 425 nm and 485 nm can be identified

as related to the V^{4+} intrinsic absorption, which corresponds to the ${}^2T_{2g}-{}^2E_g$ transition. The double peak characteristic is due to the dynamic Jahn-Teller effect acting on the 2E_g level (see Ref. 4 and references therein). The features with maxima at 250 nm and 320 nm are possibly due to charge transfer processes. The absorption spectrum of sample #37 (size: 2.0 mm x 2.5 mm x 12.1 mm), which was doped only with vanadium and grown in argon, is shown for comparison. This sample contains mostly V^{3+} which has, in the visible, two strong absorption bands with maxima at 400 nm and 570 nm. From the relative strength of the absorption bands present in sample #50 it can be concluded that most of the vanadium ions in this sample are in the 4+ valence state.

The fluorescence lifetime versus temperature was also measured. The results are shown in Figure 1-d. At room temperature, the fluorescence lifetime is 1.2 μ s. Thermal quenching becomes important above room temperature. From these measurements, and the width and position of the emission spectrum, the resultant value for the stimulated emission cross section is: $\sigma_{se} = 5.2 \cdot 10^{-19} \text{ cm}^2$.

References

1. V.A. Sandulenko and E.A. Sidorova, Opt. Spectrosc. (USSR) 60, 2 (1986).
2. J.Y. Wong, M.J. Berggren and A.L. Schawlow, J. Chem. Phys., 49, 835 (1968).
3. M. Villedieu, N. Devismes and A.M. Goer, J. Phys. Chem. Solids, 38, 1063 (1977).
4. B. Champagnon and E. Duval, J. Phys C: Solid State Phys., 12, L425 (1979).
5. R.S. Feigelson, in Tunable Solid State Lasers, ed P. Hammerling, A.B. Bugdor and A. Pinto (Springer-Verlag, Berlin Heidelberg, 1985), p. 129.

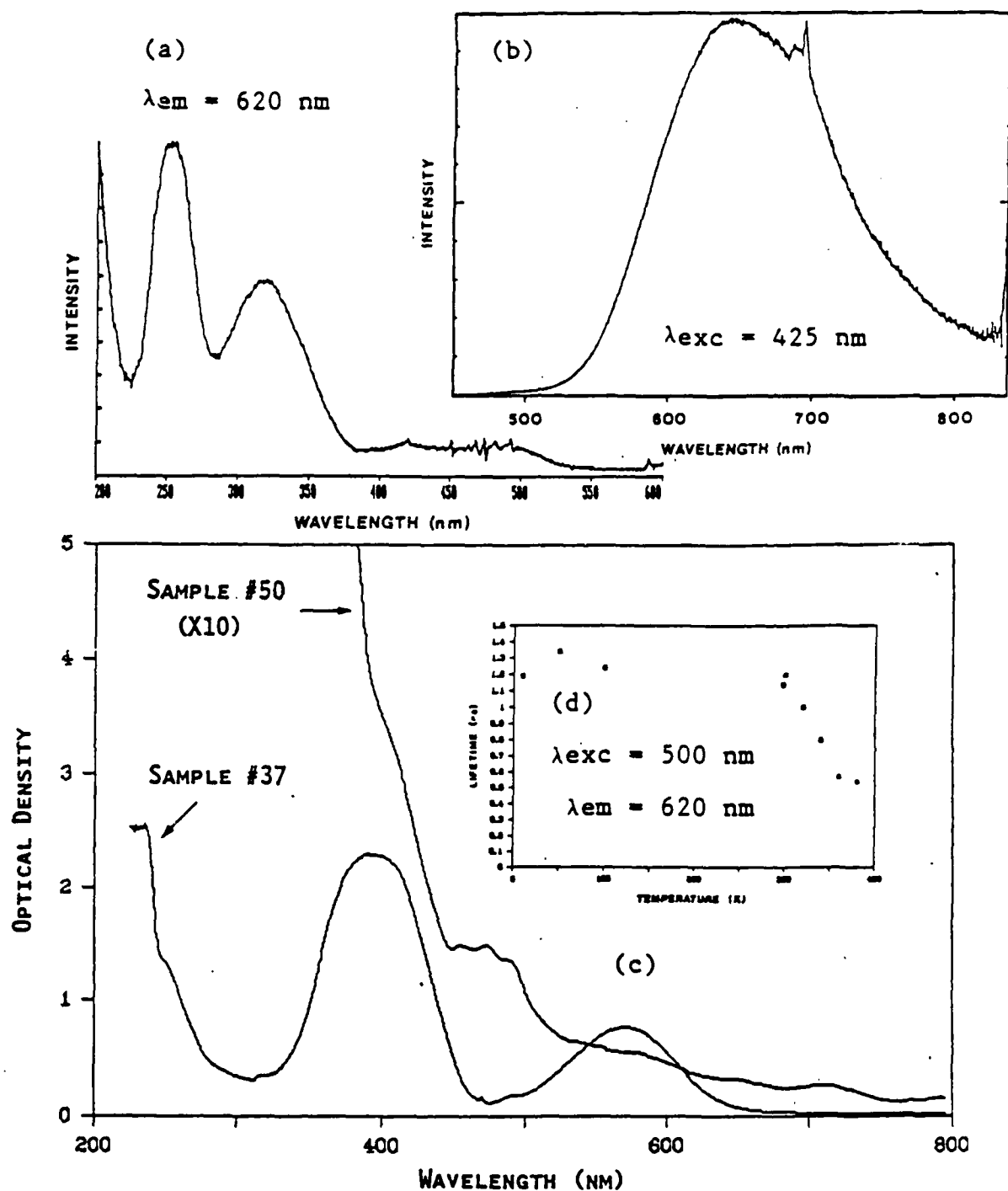


FIG. 1: Excitation (a), fluorescence (b) and absorption (c) spectra and fluorescence lifetime (d) for V,Mg: α Al₂O₃ (sample #50); T=295 K.

CECOM CENTER FOR NIGHT VISION AND ELECTRO-OPTICS
CHARACTERIZATION OF THE OPTICAL SPECTRA OF EuA10₃:Ti AND GdA10₃:Ti

Characterization of the Optical Spectra of $\text{EuAlO}_3\text{:Ti}$ and
 $\text{GdAlO}_3\text{:Ti}$

Larry Merkle^a, Horacio Verdun, Uwe Brauch^b,
German de la Fuente and Edward Behrens^c

Fibertek, Inc.

510-A Herndon Parkway, Herndon, VA 22070

Toomas H. Allik

Science Applications International Corporation

1710 Goodridge Drive, McLean, VA 22102

Albert Pinto and Wayne Hovis

U.S. Army Night Vision and Electro-Optics Center

Fort Belvoir, VA 22060

^aPermanent address: Department of Physics, University of
Arkansas, Fayetteville AR 72701

^bPresent address: DFVLR Institute Fur Technische Physik,
Pfaffenwaldring 38-40, D-7000 Stuttgart 80 Federal Republic
of Germany

^cPresent address: Department of Physics, Oklahoma State
University, Stillwater OK 74078

Abstract

Two oxide perovskites, EuAlO_3 and GdAlO_3 , doped with titanium, have been grown by the laser-heated pedestal growth method. The crystal structure of EuAlO_3 is found to be different than that reported by other workers. The absorption spectra of $\text{EuAlO}_3\text{:Ti}$ and the lack of fluorescence from this material indicate that the titanium enters the lattice as Ti^{4+} . On the other hand, the spectra of $\text{GdAlO}_3\text{:Ti}$ are attributable to Ti^{3+} . The difference between EuAlO_3 and GdAlO_3 can be attributed to the difference in third ionization potentials between europium and gadolinium. The spectra of $\text{GdAlO}_3\text{:Ti}$ indicate that it has potential as a tunable laser material.

I. Introduction

The trivalent titanium ion placed in an octahedral field is very promising for tunable solid state laser applications due to its strong, broad ${}^2e_g-{}^2t_{2g}$ emission band. The fluorescence can lie in the long wavelength visible range or the near infrared, depending on the crystal field. Its $[Ar]3d^1$ configuration permits no intraconfigurational excited state absorption transitions, which is a significant problem in some other solid state systems. ^{1,2} Sapphire doped with Ti^{3+} has proven to be a successful tunable laser material. ^{3,4}

There is significant interest to investigate Ti^{3+} in other hosts, in which laser action may occur in spectral regions other than that of Ti^{3+} in sapphire, and in which crystal growth and mechanical and thermal properties may be optimized for laser applications. The oxide perovskites, with general chemical formula ABO_3 , contain a large A ion occupying a twelvefold coordination site and a smaller B ion in the sixfold (octahedral) site. In these materials, small transition metals tend to enter the B site. ⁵ Perovskites form a promising class of laser hosts since no tetrahedrally coordinated cation sites exist whose lower crystal field could give unwanted absorption at the sixfold coordinated ions' emission wavelength.

The work reported here is part of a systematic study of the properties of Ti^{3+} in perovskite and other hosts grown by the laser-heated pedestal (LHP) growth method.⁶ This method permits the rapid growth of single crystals of a wide range of compounds so that more extensive studies of host dependent optical properties can be undertaken than by Czochralski or Bridgman techniques. In this paper, the optical properties of $EuAlO_3:Ti$ and $GdAlO_3:Ti$ are reported. Section II reviews the pedestal growth technique and the crystal structure of $EuAlO_3$, and Section III presents the optical properties of both materials. Interpretation of the data is discussed in Section IV, with concluding remarks following in Section V.

II. Crystal Growth and Properties

The crystals for this study were grown by the LHP growth method using a 250-watt, CO_2 laser. Sintered ceramic compacts were obtained from starting stoichiometric amounts of Al_2O_3 (99.999%, Cerac), Gd_2O_3 (99.999%, Cerac), Eu_2O_3 (99.995%, Cerac), and Ti_2O_3 (99.8%, Cerac) powders. The starting powdered components were milled in acetone for ca. 30 minutes inside a sintered corundum jar ball mill (Brinkman mixer mill model MM2), and subsequently dried in an oven. The dried powder was then placed into a stainless steel die assembly (28 mm diameter) and a compact was formed

at a force of 14 tons during a period of 30 minutes. The powder compact was then sintered for 12 hours at 1100°C (EuAlO_3) or at 1500°C (GdAlO_3) in air. The hard, sintered compact was cut into rectangular feed rods (of size ca. 2.5 x 2.5 x 26 mm³) and mounted on a graphite holder fitted into the bottom chuck of the LHP growth apparatus. A platinum wire was attached to the top chuck of the apparatus and used as a primer to initiate the nucleation process. The LHP apparatus is comprised of a CW, 250-watt, CO₂ laser adapted to a growth chamber capable of handling oxidizing and reducing environments. A top metal chuck inside the chamber is used for mounting primers or seeds, while a bottom counterpart is used for mounting ceramic feed-rod precursors. The laser beam is focused onto the feedrod, which is rotated in order to evenly distribute the heat generated by the laser throughout the molten zone. The rotating seed or primer is then inserted into the melt and nucleation is allowed to take place. After several minutes, the crystal is pulled from the melt by lifting the upper chuck while feeding at a slower rate with the lower chuck. The resulting polished crystals are typically 1 to 2 mm in diameter and 20 to 50 mm long. This growth process has also been recently described as the laser floating zone melting method,⁷ and has been adapted for the growth of materials with different applications.⁸ The specific growth parameters reported here are summarized in Table I. Because both titanium and europium are heterovalent, the influence

of the growth atmosphere on the valence state must be considered. For this reason, some samples were grown in air, and others in 99.95% pure nitrogen.

Single crystal x-ray diffraction, performed on a Nicolet R3m/ μ diffractometer, was employed to characterize the EuAlO_3 samples. Evaluation of several axial photographs reveal that structure has tetragonal P symmetry, rather than the orthorhombic structure reported by others.⁹ The unit cell parameters of this crystal at room temperature are $a_0 = 0.3736$ nm and $c_0 = 0.7466$ nm. Since the pedestal growth method creates large thermal gradients along the sample, and perovskites have the propensity for structure transformations in narrow temperature ranges,¹⁰ it is possible that the observed structure represents a high temperature phase of EuAlO_3 "frozen in" at room temperature. This structure is a distortion of the cubic perovskite structure with a cubic pseudocell size equal to 0.374 nm.

III. Optical Spectroscopy

Optical spectra were taken using a Spex F222 and Perkin-Elmer Lambda 9 and MPF-66 spectrometers. These instruments permitted the measurement of absorption, fluorescence and excitation spectra. The absorption spectrometer is equipped with a 4X beam condenser (Harrick Scientific Corporation, Ossining, NY). Considerable care

was taken to discriminate against spurious signals such as filter fluorescence. Fluorescence lifetime data were taken using pulsed excitation by the second and third harmonics of a Quantel Q-switched Nd:YAG laser. Detection was by a cooled photomultiplier coupled to a quarter meter monochromator or by a silicon photodiode with color filters. Low temperature experiments were carried out by placing the samples on the cold tip of a CTI Model 21 cryogenic refrigerator.

The absorption spectra of two EuAlO_3 samples grown in air are shown in Figure 1. Absorption in the undoped samples for wavelengths longer than 300 nm is attributable to Eu^{3+} transitions. Fluorescence from undoped samples also exhibits only transitions of this ion. No evidence of Eu^{2+} absorption or emission has been found, unlike the results reported by Jaffe.¹¹ The room temperature fluorescence lifetime of the $\text{Eu}^{3+} {}^5\text{D}_0$ state in the undoped sample grown in air is 2.5 microseconds for 355 nm excitation and 4.5 microseconds for 532 nm excitation. For an undoped sample grown in nitrogen, the corresponding values are 6.5 and 17 microseconds, respectively. In this sample, lifetimes were also measured at low temperature, about 20 K, and were found to be unchanged from the room temperature values. All these lifetimes are far shorter than observed for systems with dilute concentrations of Eu^{3+} , which are about 2 to 3 milliseconds even in glass.¹² This must indicate that in

EuAlO_3 the lifetime is limited by interionic processes such as energy migration to traps. The difference in lifetimes between the two samples suggests that such traps are more common in the sample grown in oxidizing atmosphere.

The Eu^{3+} fluorescence has also been observed in lightly doped $\text{EuAlO}_3\text{:Ti}$ samples. Its lifetime at room temperature under 355 nm excitation is 0.5 microseconds which is much shorter than in the undoped samples. This suggests that energy transfer from the Eu^{3+} is increased in the doped samples.

As Figure 1 shows, the introduction of titanium into EuAlO_3 changes its absorption spectrum dramatically. The strong, very broad absorption band in the visible and near infrared is not consistent with that expected for Ti^{3+} in an octahedral field. In addition, doping introduces a strong ultraviolet band between about 400 nm and the absorption edge of undoped EuAlO_3 . The strengths of both these bands increase in rough proportion to the Ti concentration in the starting materials, as shown in Figure 2. Since the samples used are of different thickness, the absorbance values at 345 nm (indicative of the strength of the ultraviolet band) and at 650 nm (the visible band) are normalized by the absorbance of the Eu^{3+} peak near 466 nm in each sample. Note that two samples were grown with 0.48% (atomic) of Ti in the starting material, and that both absorption bands are

stronger for the sample grown in N_2 than for that grown in air.

No fluorescence has been observed from the doped samples except for weak Eu^{3+} emission in the most lightly doped samples. Taken together with the absorption spectra, it is apparent that little if any of the titanium has remained in the trivalent state in these samples. The visible band does not correspond to intra-ionic transitions in other charge states of Ti, but its strength may be indicative of a charge transfer transition.

Samples of $GdAlO_3:Ti^{3+}$ have also been grown and studied. In these samples the absorption and fluorescence in the visible region is consistent with the presence of Ti^{3+} . The excitation and fluorescence spectra are presented in Figure 3 for a sample grown in nitrogen with 0.48 weight % Ti added to the melt. The pair of absorption peaks at 445 and 490 nm may be attributed to transitions from the $^2t_{2g}$ to the 2e_g state, using the familiar labels which would apply in a truly octahedral environment, with the latter level split by the Jahn-Teller effect as well as by non-octahedral components of the crystal field. Similarly the fluorescence band position and its room temperature lifetime of about 5 microseconds are consistent for a transition from the lower 2e_g state to the $^2t_{2g}$ state. At a temperature of 12 K the fluorescence lifetime was

measured to be 14 microseconds, thus implying a quantum efficiency of 36% at room temperature. The positions of these transitions indicate that the crystal field at the impurity site is approximately 20% stronger in GdAlO_3 than in Al_2O_3 .³ The change expected in the crystal field approximation can be estimated by noting that in Al_2O_3 each Al has three oxygen neighbors at a distance of 0.166 nm and three at 0.197 nm. Whereas in GdAlO_3 , assuming for simplicity the cubic perovskite structure, each Al has six oxygen neighbors at a distance of 0.1855 nm.¹³ The familiar inverse fifth power distance dependence of the crystal field thus predicts a 16% stronger field in GdAlO_3 than in Al_2O_3 , in reasonable agreement with experiment. The excitation peak at 355 nm does not correspond to any transition within the $3d^1$ configuration of Ti^{3+} . It may be due to absorption by another impurity which then transfers its energy to Ti, or in view of the discussion of section IV, perhaps to charge transfer from Ti^{3+} to Gd^{3+} . In any case, it is clear that the titanium dopant enters the GdAlO_3 lattice in the trivalent state, in contrast to the situation for EuAlO_3 .

IV. Discussion

The striking difference between the behavior of titanium in EuAlO_3 and GdAlO_3 is probably not attributable to crystal field effects, as the ionic radii of Eu^{3+} and Gd^{3+} are quite similar, 0.102 - 0.106 nm and 0.100 - 0.104

nm respectively.¹⁴ Rather, it is of interest to note that the third ionization potentials of these two rare earths are quite different, 24.92 eV for europium and 20.63 eV for gadolinium.¹⁵ In addition, for the crystal EuTiO_3 , the europium ions have been found to be divalent and the titanium ions tetravalent.^{16,17} This suggests that in $\text{EuAlO}_3\text{:Ti}$, the dopant ions become tetravalent, each making a nearby europium divalent to conserve charge. The ability of Ti to remain trivalent in GdAlO_3 would presumably be due to the smaller third ionization potential of Gd, inhibiting it from accepting an electron from Ti.

A simple calculation based on a lattice of point ions may be undertaken to test the suggestion that Ti in EuAlO_3 is tetravalent and a nearby Eu divalent. Following the work of Pedrini et al.¹⁸, the energy difference between such a state and a situation in which both ions are trivalent may be evaluated in terms of the ionization potentials, Madelung energies, and crystal field energies of the two ions given in Eq. 1..

$$E(\text{Eu}^{2+}\text{+Ti}^{4+}) - E(\text{Eu}^{3+}\text{+Ti}^{3+}) = I_4(\text{Ti}) - I_3(\text{Eu}) - E_M(\text{Ti site}) \\ + E_M(\text{Eu site}) - E_C(\text{Ti-Eu}) - E_{\text{Cf}}(\text{Ti}) \quad (1)$$

Here $I_4(\text{Ti})$ is the fourth ionization potential of titanium, 43.24 eV.¹⁹ $I_3(\text{Eu})$ is the third ionization potential of europium, E_M is the magnitude of the Madelung energy at the

indicated site, $E_C(\text{Ti-Eu})$ is the magnitude of the Coulomb energy of attraction between the extra positive charge on Ti^{4+} and the extra electron on Eu^{2+} , and $E_{\text{Cf}}(\text{Ti})$ is the crystal field contribution to the energy of the ground state of Ti^{3+} . The ground state of Ti^{4+} is nondegenerate and each valence state of Eu exhibits only a small crystal field splitting, so that the crystal field contributions for these ions are neglected. The Madelung energy was calculated by standard methods.²⁰ To simplify the calculation of the E_M and E_C terms, the lattice has been approximated by that of a cubic perovskite with lattice constant 0.374 nm. It is assumed that the Eu which accepts an electron from the Ti is one of the nearest-neighbor Eu ions. With these assumptions, $E_M(\text{Ti site})$ is 45.95 eV, $E_M(\text{Eu site})$ is 22.57 eV and $E_C(\text{Ti-Eu})$ is 4.46 eV. The crystal field contribution to the Ti^{3+} ground state energy is estimated by assuming an octahedral environment, so that $E_{\text{Cf}} = -4Dq$, and was determined from the Ti^{3+} spectra in GdAlO_3 to be 1.07 eV. In this way it is estimated that a $\text{Ti}^{4+}\text{-Eu}^{2+}$ pair in $\text{EuAlO}_3\text{:Ti}$ is lower in energy than a $\text{Ti}^{3+}\text{-Eu}^{3+}$ pair by 8.4 eV. Despite the crudeness of the calculation, this result strongly supports the attribution of the lack of Ti^{3+} in $\text{EuAlO}_3\text{:Ti}$ to instability of the trivalent ion.

Comparison of the spectra of Ti in the two hosts suggests that the above calculation has overestimated the energy difference between the two charge states. Since the

major change in the above calculation upon switching to the GdAlO_3 host is the 4.29 eV difference in I_3 of the rare earth, this calculation predicts that Ti^{3+} would also be unstable in this host. Thus, the presence of Ti^{3+} in GdAlO_3 may suggest that the energy difference between the two charge states has been overestimated, and that the $\text{Eu}^{3+}\text{-Ti}^{3+}$ state in $\text{EuAlO}_3\text{:Ti}$ is higher in energy than the $\text{Eu}^{2+}\text{-Ti}^{4+}$ state by no more than about 4 eV.

This overestimation is surprising since a similar approach to the calculation of photoionization energies of divalent rare earth dopants has generally been accurate to within an electron volt.²¹ The larger error in the present case makes the attribution of the optical properties of $\text{EuAlO}_3\text{:Ti}$ to Ti^{4+} less certain. However, the error may plausibly be attributed to the crudeness of the calculations. Not only has an idealized (cubic) version of the crystal structure been used to calculate the Madelung energies, but, more importantly, no attempt has been made to correct these energies for the local distortion of the lattice around the impurity site. Although no data are available to determine this distortion, it can make a sizable contribution to the Madelung energies.

The above discussion suggests plausible interpretations for the strong visible and near infrared absorption band and for the absorption edge near 400 nm in EuAlO_3 . The visible-

infrared band may be attributed to a charge transfer transition in which an electron is moved from a Eu^{2+} ion to the nearby Ti^{4+} . If so, the energy of $\text{Eu}^{2+}\text{-Ti}^{4+}$ pair must be lower than that of a $\text{Eu}^{3+}\text{-Ti}^{3+}$ pair by no more than about one eV. The 400 nm absorption edge lies near the onset of the lower absorption band of Eu^{2+} in EuAlO_3 reported by Jaffe¹¹ and is also near the absorption edge of TiO_2 , in which each titanium ion is coordinated by six oxygens much as in these perovskites. Thus, the ultraviolet absorption may be due to Eu^{2+} , Ti^{4+} , or both. It should be noted that no evidence of Eu^{2+} fluorescence has been observed upon ultraviolet excitation of $\text{EuAlO}_3\text{:Ti}$. However, the strong visible absorption band overlaps the wavelength range in which Eu^{2+} emission is expected, so that efficient energy transfer, either radiative or nonradiative, may explain this lack of fluorescence.

The excitation and fluorescence spectra of $\text{GdAlO}_3\text{:Ti}$ permit a preliminary consideration of its potential as a laser material. The five microsecond lifetime, 9×10^{13} Hz fluorescence bandwidth and 36% quantum efficiency imply a peak stimulated emission cross section of $4 \times 10^{-20} \text{ cm}^2$. This is smaller than the peak cross section in $\text{Al}_2\text{O}_3\text{:Ti}$ and comparable to that of typical Cr^{3+} -based laser materials. It will be important to determine the nature of the observed ultraviolet excitation band. If it is due to Ti^{3+} itself rather than to some inadvertant impurity, it may give rise

to excited state absorption. The wavelength limit of the present experiments leaves open the question of whether such excited state absorption would interfere with laser emission.

V. Conclusions

A number of properties are important in determining a material's potential as a solid state laser. In addition to optical properties such as absorption, excited state absorption and stimulated emission cross sections, factors affecting growth such as size and charge matching must also be considered. The investigation of $\text{EuAlO}_3\text{:Ti}$ presented here demonstrates the influence which the host can have on yet another factor, the dopant's valence state. It is anticipated that similar difficulties would arise for Ti doping of hosts containing Yb^{3+} , as it also has a large third ionization potential. Among the rare earths, only gadolinium, and perhaps cerium and terbium, has a sufficiently small third ionization potential and wide enough absorption-free regions in the visible range to be of interest for titanium-doped laser materials. As noted in the previous section, $\text{GdAlO}_3\text{:Ti}$ does indeed appear to be an interesting system for further study.

The point-ion based calculation of the energy difference between the two possible charge states of the

dopant and a nearest neighbor rare earth was only partially successful, having predicted that Ti^{4+} would be more stable than Ti^{3+} in $GdAlO_3$ as well as in $EuAlO_3$. Without direct data on the positions of the ions neighboring the impurity site, it is difficult to know whether this difficulty is fully attributed to the crudeness of the ionization calculations. Based on the known charge states of the Ti and Eu ions in $EuTiO_3$, however, the interpretation of the spectra given in Section IV remains the most plausible.

Acknowledgments: Both the Fibertek and SAIC work was sponsored by the Center for Night Vision and Electro-Optics.

References

1. P. F. Moulton, *Laser Focus* 19(5), 83 (1983).
2. M. L. Shand and H. P. Jenssen, *IEEE J. Quantum Electron.* QE-19(3), 480 (1983).
3. G. F. Albrecht, J. M. Eggleston, and J. J. Ewing, *Opt. Commun.* 52(6), 401 (1985).
4. Several papers on this system are found in Tunable Solid-State Lasers II, ed. A. B. Budgor, L. Esterowitz, and L. G. DeShazer, (Springer-Verlag, Berlin Heidelberg, 1986).
5. J. P. van der Ziel and L. G. Van Uitert, *Phys. Rev. B* 8(5), 1889 (1973).
6. R. S. Feigelson, in Tunable Solid State Lasers, ed. P. Hammerling, A. B. Budgor, and A. Pinto (Springer-Verlag, Berlin Heidelberg, 1985), p. 129.
7. K. Dembinski, J. M. Bassat, J. P. Coutures and P. Odier, *J. Mater. Science Lett.* 6, 1365 (1987).
8. X. P. Jiang, G. W. Quao, J. G. Huang, Y. Yu, M. Jiang, Y. L. Ge, Z. Q. Hu, C. X. Shi, Y. H. Zheo, Y. J. Wang, G. Z.

Su and Y. E. Zhuo, Extended Abstracts, High-Temperature Superconductors II, MRS Spring Meeting Symposium, Reno, NV. 1988, D. W. Capone II, W. H. Butler, B. Batlogg and C. W. Chu, EDS. Materials Research Society, Pittsburgh, PA, 1988.

9. S. Geller and V. B. Bala, Acta Cryst. 2, 1019 (1956).
10. O. Muller and R. Roy, The Major Ternary Structural Families, (Springer-Verlag, New York, 1974) pp.175-229.
11. P. M. Jaffe, J. Electrochem. Soc. 117(7), 918 (1970).
12. X. Gang and R. C. Powell, J. Appl. Phys. 57(4), 1299 (1985).
13. R. Wyckoff, Crystal Structures, (Wiley Interscience, New York, 1964) vol. 2, pp.7,392.
14. S. K. Dickinson, Air Force Cambridge Research Laboratories Physical Sciences Research Paper 439 (1970).
15. W. Martin, L. Hagan, J. Reader and J. Sugar, J. Phys. Chem. Phys. Ref. Data 3(3), 771 (1974).
16. J. Brous, I. FanKuchen, and E. Banks, Acta Cryst. 6, 67 (1953).

17. T. R. McGuire, M. W. Shafer, R. J. Joenk, H. A. Alperin, and S. J. Pickart, J. Appl. Phys. 37(3), 981 (1966).
18. C. Pedrini, D. S. McClure, and C. H. Anderson, J. Chem. Phys. 70(11), 4959 (1979).
19. Handbook of Physics and Chemistry, 52nd ed., ed. Robert Weast, (Chemical Rubber, Cleveland, 1971).
20. M. P. Tosi, Solid State Physics, vol.16, editors F. Seitz and D. Turnbull (Academic Press, New York, 1964) p. 13.
21. C. Pedrini, F. Rogemund, and D. S. McClure, J. Appl. Phys. 59(4), 1196 (1986).

Figure Captions

1. Room temperature optical absorption of two EuAlO_3 samples grown in air. Lower trace: Undoped, sample length is 1.14 mm. Upper dashed trace: Doped sample with 0.47% (atomic) Ti. Sample length is 0.71 mm. (The concentration refers to that in the starting material.)

2. Relative absorbance at 345 nm and at 650 nm versus x in $\text{EuAl}_{1-x}\text{O}_3:\text{Ti}_x$. Each value is a ratio of the absorbance at the stated wavelength to the absorbance of the Eu^{3+} line at 466 nm.

Squares: Absorbance at 650 nm for samples grown in air.

Asterisk: Absorbance at 650 nm for sample grown in N_2 .

Diamonds: Absorbance at 345 nm minus that at 440 nm, samples grown in air.

Circle: Absorbance at 345 nm minus that at 440 nm, sample grown in N_2 .

3. Room temperature fluorescence and excitation spectra of $\text{GdAlO}_3:\text{Ti}$. The fluorescence spectrum is corrected for instrument response.

Table I
LHP Crystal Growth Parameters

Stoichiometric Formula	x	Atmosphere	Laser Power (W)	Rotation (rpm)		Translation (cm/h)		Size (mm ³)	Color
				Feed	Primer	Feed	Crystal	Dia x Length	
EuAl _{1-x} Ti _x O ₃	0	Air	110	370	-600	0.35	0.70	1.7 x 18.3	Pink-Orange
EuAl _{1-x} Ti _x O ₃	0	99.995% N ₂	115	370	-600	0.35	0.70	1.5 x 19.7	Colorless
EuAl _{1-x} Ti _x O ₃	0.00063	Air	85	370	-400	0.35	0.70	1.4 x 19.0	Light Violet
EuAl _{1-x} Ti _x O ₃	0.0022	Air	83	370	-400	0.35	0.70	1.3 x 32.4	Violet
EuAl _{1-x} Ti _x O ₃	0.0047	Air	134	370	-400	0.87	1.41	1.0 x 34.0	Strong Violet
EuAl _{1-x} Ti _x O ₃	0.00063	99.995% N ₂	98	370	-540	0.42	0.70	1.2 x 26.0	Violet
EuAl _{1-x} Ti _x O ₃	0.0024	99.995% N ₂	64	370	-400	0.87	1.41	1.4 x 28.6	Dark Violet
GdAl _{1-x} Ti _x O ₃	0.0048	99.995% N ₂	118	370	-370	0.42	1.40	1.3 x 42.0	Light Yellow
GdAl _{1-x} Ti _x O ₃	0.0048	Air	100	370	-370	0.35	0.70	1.7 x 38.0	Colorless
GdAl _{1-x} Ti _x O ₃	0.0048	Ar + 0.75% H ₂	110	360	-360	0.35	0.70	1.5 x 43.0	Pale brown-yellow
GdAl _{1-x} Ti _x O ₃	0	O ₂	65	360	-360	0.70	1.05	1.3 x 50.0	Light brown

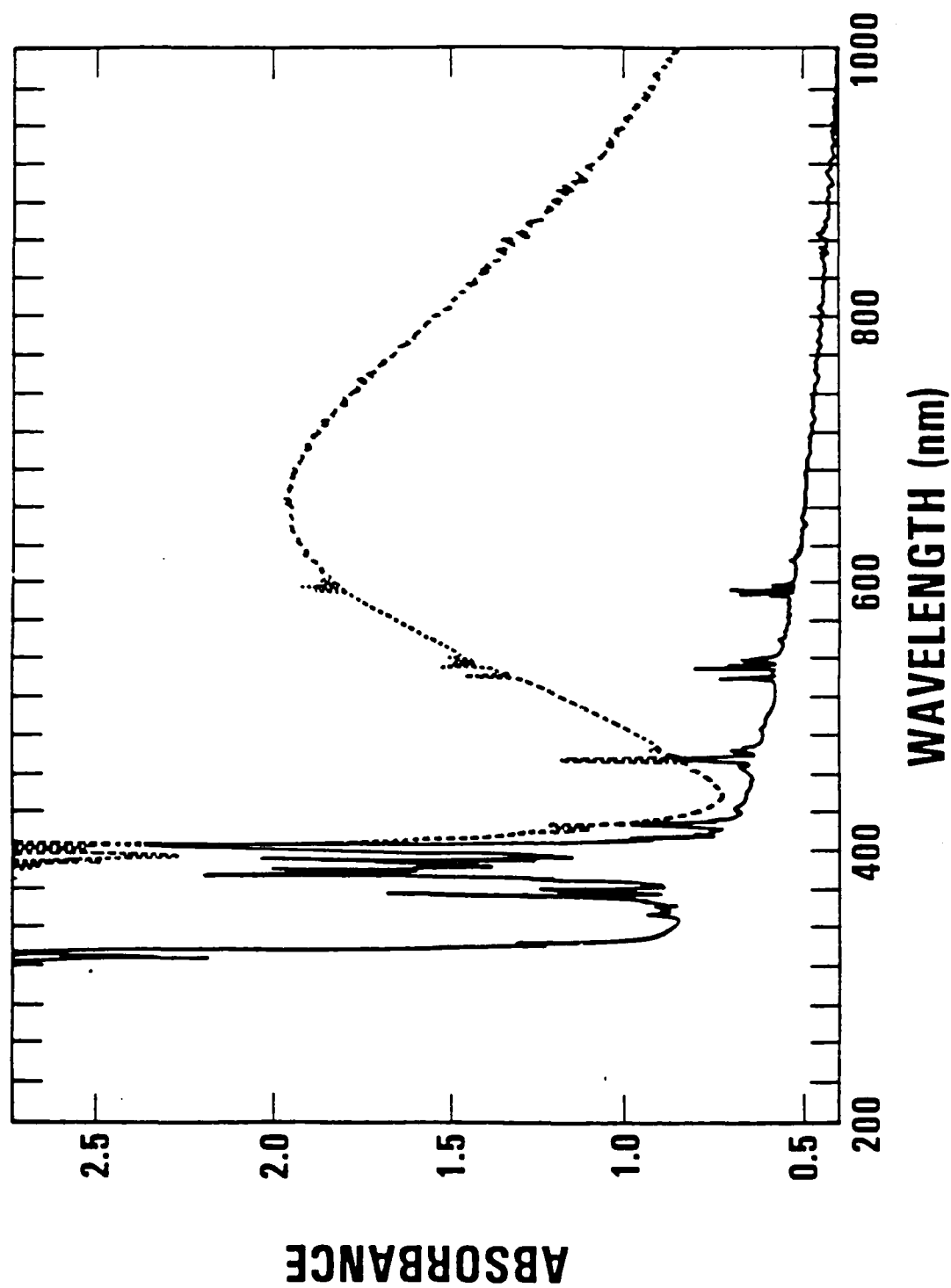


FIGURE 1

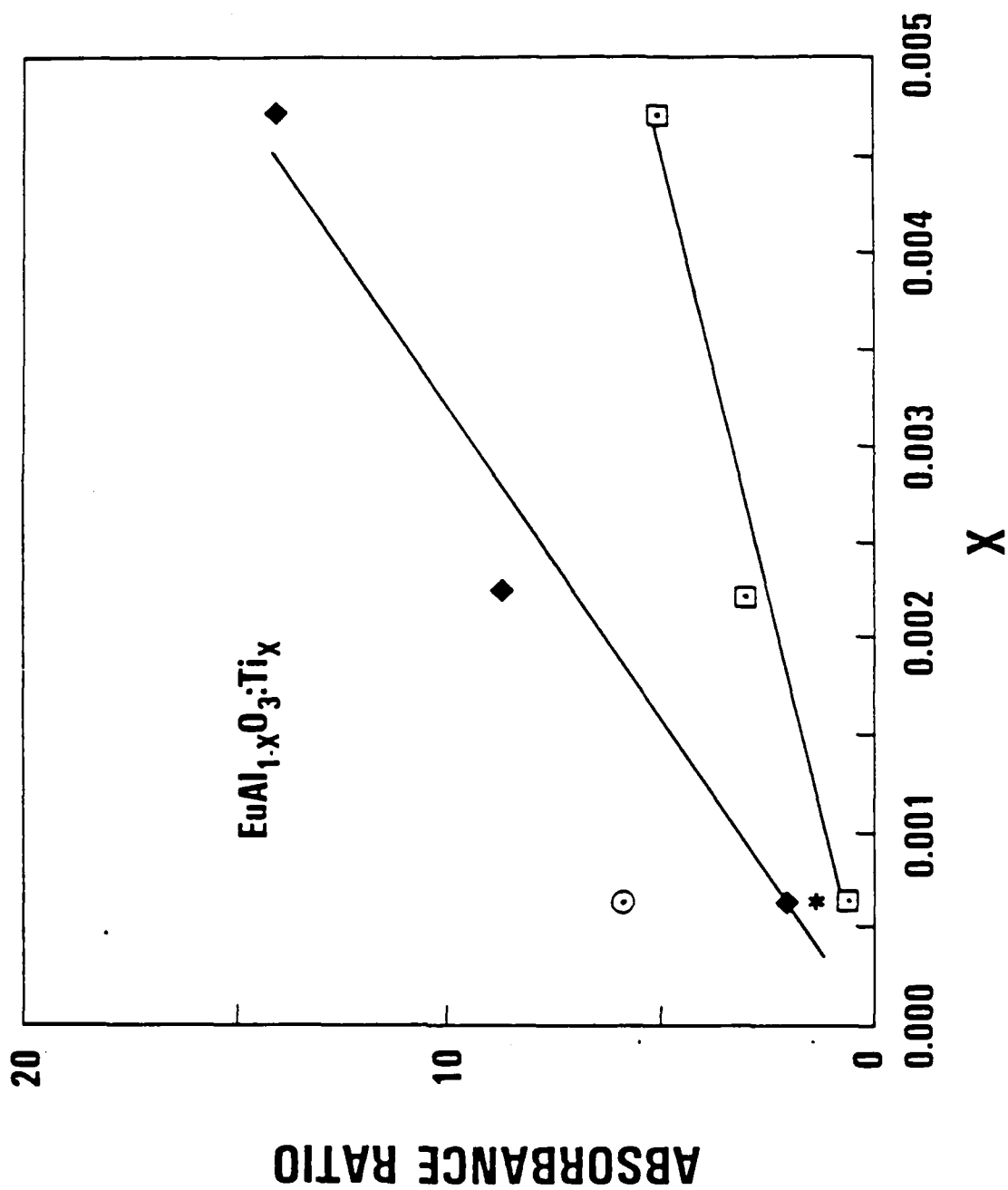


FIGURE 2

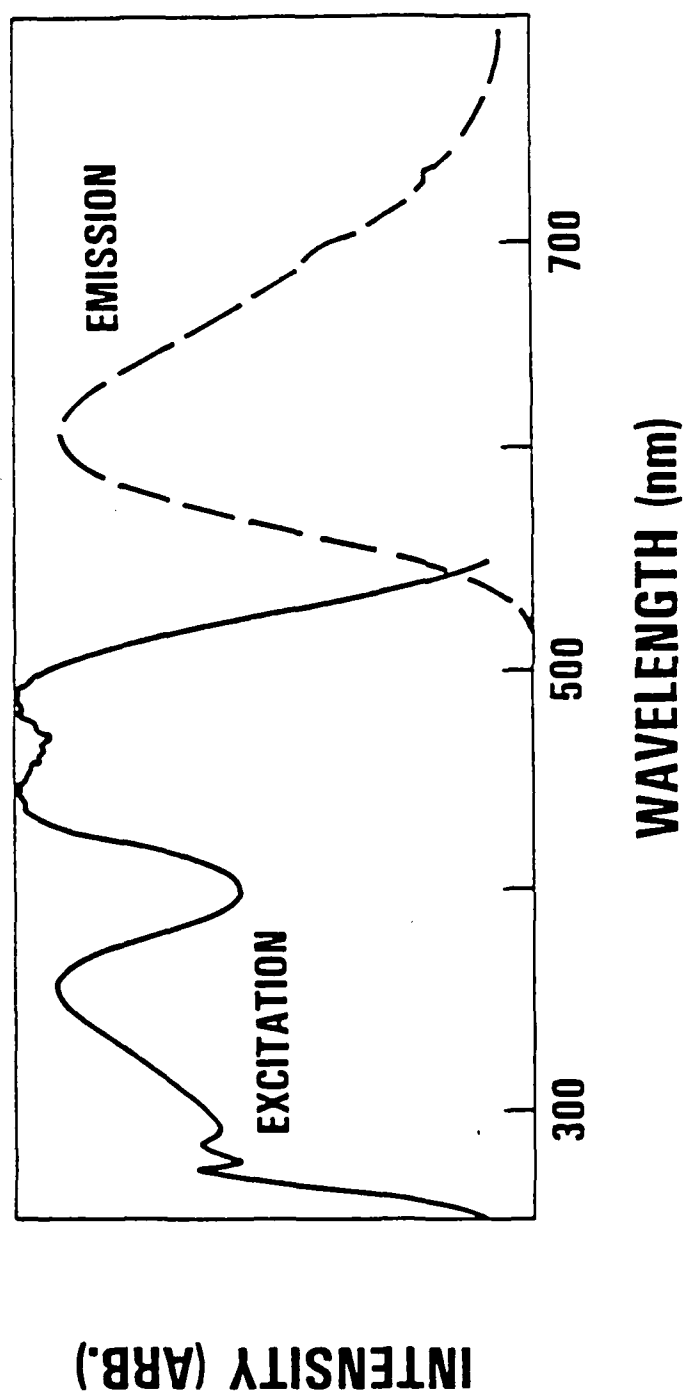


FIGURE 3

ATTENDANCE

LIST OF ATTENDEES

OPTOELECTRONIC WORKSHOP

DYNAMICAL INSTABILITIES IN HOMOGENEOUSLY BROADENED LASERS

August 23, 1988

NAME	ORGANIZATION	PHONE
Tom Allilc	NVEOC, SAIC	703-664-4766
David Caffey	NVEOC, Laser Div.	703-664-1431
Tom Colandene	NVEOC, Laser Div.	703-664-5310
Vernon King	NVEOC, Laser Div.	703-664-1431
Andy Mott	NVEOC, Laser Div.	703-664-1432
Al Pinto	NVEOC, Laser Div.	703-664-5310
Jay Sonstroem	NVEOC, Laser Div.	703-664-5310
Ward Trussell	NVEOC, Laser Div.	703-664-5310
Richard Utano	NVEOC, Laser Div.	703-664-4766
Ronald Antos	UR, Optics	716-275-4179
Stephen Chakmakjian	UR, Optics	716-275-8006
Karl Koch	UR, Optics	716-275-8006
Carlos Stroud	UR, Optics	716-275-2598